Title

Intrinsic plasma flows in straight magnetic fields: generation, frictionless saturation, and interaction

Author

Li, Jiacong

Publication Date

2018

UNIVERSITY OF CALIFORNIA SAN DIEGO

Intrinsic plasma flows in straight magnetic fields: generation, frictionless saturation, and interaction

A dissertation submitted in partial satisfaction of the
requirements for the degree
Doctor of Philosophy

in

Physics

by

Jiacong Li

Committee in charge:

Patrick H. Diamond, Chair
Farhat N. Beg
George R. Tynan
David R. Tytler
Congjun Wu
Xueqiao Xu

2018

The dissertation of Jiacong Li is approved, and it is acceptable in quality and form for publication on microfilm and electronically:

Chair

University of California San Diego

2018

DEDICATION

To my grandfather

TABLE OF CONTENTS

LIST OF FIGURES

LIST OF TABLES

ACKNOWLEDGEMENTS

This thesis could not have been completed without the help of many individuals to whom I owe much thanks. First, my sincere gratitude goes to my advisor Prof. Patrick H. Diamond for his continuous support of my PhD study. Pat spent tremendous time in discussing my results, polishing manuscripts, and helping me practice presentations. His clear and deep understanding of the relevant topics guided me through a successful PhD study. I owe my thanks to Pat for his guidance and help with my research.

I would like to thank Prof. George R. Tynan for his constructive opinions on aspects of my research related to experiments. I thank Dr. Xueqiao Xu for his guidance and support in computer simulation using BOUT++. I would also like to thank other members in my dissertation committee: Prof. Farhat N. Beg, Prof. David R. Tytler, and Prof. Congjun Wu. I thank you all for your valuable comments and suggestions on my thesis research.

My special thanks go to Dr. Rongjie Hong and Prof. Zhibin Guo. I owe my thanks to Rongjie for educating me about plasma diagnostics and experiments relevant to my thesis research. Zhibin has raised many critical questions to my results, the solutions of which have largely improved the quality of my works.

My sincere thanks also go to Dr. Min Xu, Dr. Lei Zhao, Dr. Pei-Chun Hsu, Chris Lee, Xiang Fan, Dr. Rima Hajjar, Dr. Saikat Chakraborty Thakur, Dr. Tengfei Tang, Dr. Chenhao Ma, and Dr. Tianyang Xia. I thank you all for supporting my research.

Finally, I must thank my parents and my wife for their constant love, support and encouragement. I could never ask for a better family. I owe all my success to you.

Chapter 2 is a reprint of the material as it appears in J. C. Li, P. H. Diamond, X. Q. Xu, and G. R. Tynan, “Dynamics of intrinsic axial flows in unsheared, uniform magnetic fields”, *Physics of Plasmas* **23**, 052311 (2016), American Institute of Physics. The dissertation author was the primary investigator and author of this article.

Chapter 3 is a reprint of the material as it appears in J. C. Li and P. H. Diamond, “Negative

viscosity from negative compressibility and axial flow shear stiffness in a straight magnetic field", *Physics of Plasmas* **24**, 032117 (2017), American Institute of Physics. The dissertation author was the primary investigator and author of this article.

Chapter 4 is a reprint of the material as it appears in J. C. Li and P. H. Diamond, "Interaction of Turbulence-Generated Azimuthal and Axial Flows in CSDX", which is being prepared for publication. The dissertation author was the primary investigator and author of this article.

Chapter 5 has been submitted for publication of the material as it may appear in R. Hong, J. C. Li, R. Hajjar, S. Chakraborty Thakur, P. H. Diamond, and G. R. Tynan, "Generation of Parasitic Axial Flow by Drift Wave Turbulence with Broken Symmetry: Theory and Experiment", *Physics of Plasmas* (2018), American Institute of Physics. The dissertation author was the primary investigator and author of this article.

Chapter 6 has been submitted for publication of the material as it may appear in J. C. Li and P. H. Diamond, "Another look at zonal flow physics: resonance, shear flows and frictionless saturation", *Physics of Plasmas* (2018), American Institute of Physics. The dissertation author was the primary investigator and author of this article.

The research presented in this dissertation was supported by the U.S. Department of Energy, Office of Science, Office of Fusion Energy Sciences, under Award Nos. DE-FG02-04ER54738 and DE-AC52-07NA27344, and CMTFO Award No. DE-SC0008378.

VITA

2012	B. E. in Engineering Physics, Tsinghua University, Beijing, China
2012-2014	Graduate Teaching Assistant, University of California San Diego
2018	Ph. D. in Physics, University of California San Diego

PUBLICATIONS

J. C. Li, P. H. Diamond, X. Q. Xu, and G. R. Tynan, “Dynamics of intrinsic axial flows in unsheared, uniform magnetic fields”, *Physics of Plasmas*, 23, 052311, 2016.

J. C. Li and P. H. Diamond, “Negative viscosity from negative compressibility and axial flow shear stiffness in a straight magnetic field”, *Physics of Plasmas*, 24, 032117, 2017.

J. C. Li and P. H. Diamond, “Frictionless Zonal Flow Saturation by Vorticity Mixing”, *Physical Review Letters* (Submitted for publication).

J. C. Li and P. H. Diamond, “Another Look at Zonal Flow Physics: Resonance, Shear Flows and Frictionless Saturation”, *Physics of Plasmas* (Submitted for publication).

J. C. Li and P. H. Diamond, “Interaction of Turbulence-Generated Azimuthal and Axial Flows in CSDX”, manuscript in preparation.

R. Hong, J. C. Li, R. J. Hajjar, S. Chakraborty Thakur, P. H. Diamond, G. R. Tynan, “Generation of Parasitic Axial Flow by Drift Wave Turbulence with Broken Symmetry: Theory and Experiment”, *Physics of Plasmas* (Submitted for publication).

R. Hong, J. C. Li, S. Chakraborty Thakur, R. J. Hajjar, P. H. Diamond, G. R. Tynan, “Tracing the Pathway from Drift-Wave Turbulence with Broken Symmetry to the Production of Sheared Axial Mean Flow”, *Physical Review Letters* (Submitted for publication).

ABSTRACT OF THE DISSERTATION

Intrinsic plasma flows in straight magnetic fields: generation, frictionless saturation, and interaction

by

Jiacong Li

Doctor of Philosophy in Physics

University of California San Diego, 2018

Professor Patrick H. Diamond, Chair

We develop a simple model for the generation and amplification of intrinsic axial flow in a linear device, Controlled Shear Decorrelation Experiment (CSDX). This model develops a novel dynamical symmetry breaking mechanism in drift wave turbulence, which does not require complex magnetic field structure, such as shear. Thus, the model is applicable to both tokamaks and linear devices. This mechanism is, essentially, a form of negative viscosity phenomenon.

Negative compressibility ITG turbulence can also induce a negative viscosity increment. However, we show that no intrinsic axial flow can be generated by pure ITG turbulence in a straight magnetic field. When the flow gradient is steepened by any drive mechanism, the flow

profile saturates at a level close to the value above which parallel shear flow instability (PSFI) becomes dominant over the ITG instability. This saturated flow gradient exceeds the PSFI linear threshold, and grows with ∇T_{i0} as $|\nabla V_{\|}|/|k_{\|} c_s| \sim |\nabla T_{i0}|^{2/3}/(k_{\|} T_{i0})^{2/3}$.

The coupling of azimuthal and axial flows in CSDX–in absence of magnetic shear–is investigated. In particular, we focus on the apportionment of turbulence energy between azimuthal and axial flows, and how the azimuthal flow shear affects axial flow generation and saturation by drift wave turbulence.

Detailed measurements of intrinsic axial flow parallel to the magnetic field are performed on CSDX, with no axial momentum input. The results present a direct demonstration that the broken spectral symmetry of drift wave turbulence causes the development of axial mean flows in cylindrical magnetized plasmas. Measurements suggest the axial flow is parasitic to the drift wave–zonal flow system.

Besides, we show that consideration of wave–flow resonance resolves the long-standing problem of how zonal flows (ZFs) saturate in the limit of weak or zero frictional drag and also determines the ZF scale directly from analysis. We show that resonant vorticity mixing, which conserves potential enstrophy, enables ZF saturation in the absence of drag, and so is effective at regulating the Dimits up-shift regime. Vorticity mixing is incorporated as a nonlinear, self-regulation effect in an extended 0D predator–prey model of drift–ZF turbulence.

Chapter 1

General Introduction

This dissertation studies intrinsic flows in fusion plasmas with a particular focus on the generation of intrinsic parallel flows in the absence of magnetic shear. We also investigate how the parallel and perpendicular flows interact absent magnetic shear. In addition, the saturation of zonal flows, absent frictional drag, is studied with special focus on the wave–flow resonance effect. In Section 1.1, we introduce nuclear fusion and some challenges of magnetic confinement. Next, we introduce intrinsic parallel and perpendicular (zonal) flows in magnetic confinement devices (Section 1.2) and in a linear device (Section 1.3) with straight magnetic fields, i.e., zero magnetic shear. We conclude this chapter by describing the questions we address in this thesis and the organization of the rest chapters (Section 1.4).

1.1 Nuclear fusion and magnetic confinement

Nuclear fusion results from the process of combining two or more atomic nuclei to form new atomic nuclei, along with subatomic particles (e.g., neutrons or protons). In the cosmos, fusion is the primary heat source of most stars, e.g., the Sun. In the laboratory, fusion research uses the deuterium–tritium (D–T) reaction, because it has the largest cross-section compared to other viable reaction types. Nevertheless, the D–T reaction still requires extremely high tem-

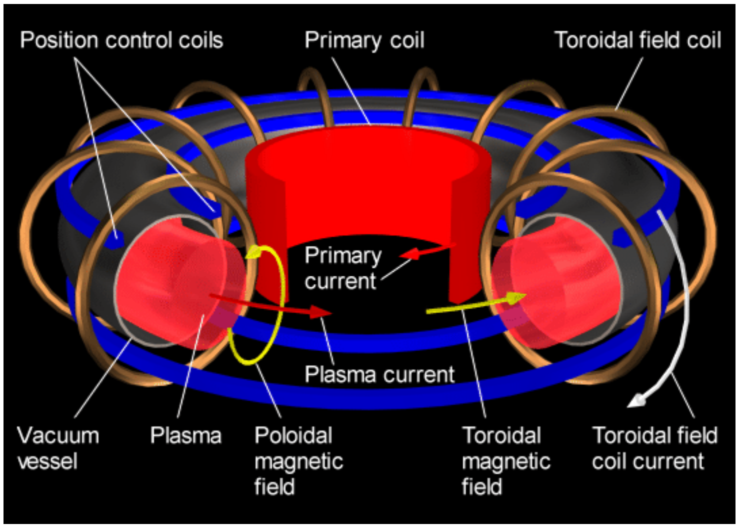

Figure 1.1: Schematic of a plasma in tokamak.

perature and high density of the fuel gas to ensure a sufficiently high reaction rate. Under such conditions, the fuel gas is ionized and thus becomes a plasma.

Confinement time and energy content are the two key factors that determine whether a fusion reactor can sustain itself. A fusion reactor needs to meet Lawson criterion [Law57] to reach ignition. Lawson criterion requires that the heating by fusion reactions needs to be sufficient to maintain plasma temperature without external power input. For the D–T reaction, ignition requires the triple product of density, temperature, and confinement time to be $nT\tau_E \geq 3 \times 10^{21}$ keV s/m^3.

One way to confine the laboratory fusion plasma is to use magnetic fields, such that the hot plasmas do not touch the reactor walls. Of various device designs, tokamaks have achieved the best performance, especially in terms of operation duration [WLG$^+$]. For tokamaks, confinement time is defined as the ratio of energy content (W) and energy loss rate (P_L), i.e., $\tau_E = W/P_L$. In steady state, the energy loss rate is balanced by the heating power P_H. Therefore, confinement time in tokamaks is calculated using $\tau_E = W/P_H$. Fig. 1.1 shows a sketch of the plasma geometry in a tokamak. It can be viewed as a torus with magnetic fields in both the toroidal direction and the poloidal direction.

Both the energy content and confinement time are reduced by the transport of particles, momentum, and thermal energy of plasmas. Turbulence leads to stronger transport than collisions, and thus is the major candidate for redistribution and loss of energy. Turbulence in tokamaks can be driven by profile gradients (e.g., ∇n and ∇T). For example, electron drift wave turbulence is a common type of turbulence in plasmas [HW83]. It is driven by ∇n and requires non-adiabatic electrons.

1.2 Intrinsic plasma flows

Turbulence-driven flows are ubiquitous in natural and laboratory plasmas. In magnetic confinement devices, shear flows generated by turbulence are effective in stabilizing the microturbulence and MHD (magnetohydrodynamics) instabilities, and thus are favorable to both microstability and macrostability [MAC^{+}11a, RHS^{+}06, DLCT94], in that intrinsic flows occur both parallel and perpendicular to the magnetic field [RHD^{+}11b, HLH^{+}18, XTD^{+}11a]. The generation of such flows is analogous to the heat engine paradigm [KDG10a]. Initially driven by profile gradients (such as ∇T and/or ∇n), the turbulence energy is coupled to both parallel and perpendicular flows.

1.2.1 Intrinsic parallel flow

Toroidal rotation of plasma is beneficial to both macrostability (e.g., the mitigation or stabilization of resistive wall modes [RHS^{+}06]) and microstability by suppressing turbulence via toroidal shear flows that contribute to $E \times B$ shear flows. Plasma rotation and the underlying toroidal angular momentum transport were intensively first studied because neutral beam injection (NBI) was the heating method of choice for tokamaks. Given that unbalanced NBI drives toroidal rotation and the experimental observation that the ion momentum and thermal diffusivities were comparable ($\chi_\phi \sim \chi_i$) [SDF^{+}90], toroidal momentum transport was thought to be diffusive and comparable to the ion heat transport. However, the discovery of the non-diffusive character of toroidal momentum transport in the JFT-2M tokamak [IMM$^+$95] disrupted that simplistic understanding of the toroidal rotation. The paradigm shift was triggered by the observation of intrinsic core rotation in the Alcator C-Mod tokamak, for both ohmically heated and ion cyclotron resonance frequency-driven plasma discharges [RLM$^+$04, LRH$^+$05]. Here, intrinsic rotation means plasma rotation without NBI drives or external wave momentum torque, i.e., self-accelerated rotation. Given the benefits of plasma rotations, the intrinsic rotation is particularly favorable for the International Thermonuclear Experimental Reactor (ITER) where NBI driven rotation is not feasible.

The discovery of intrinsic rotation has elicited interest in the non-diffusive flux (pinch and residual stress) of toroidal momentum, which can accelerate the central plasma rotation [DKG$^+$13a]. The momentum pinch, which redistributes the toroidal momentum, contributes little to rotation generation [PAB$^+$11, ACC$^+$12]. Hence, the Reynolds stress has the generic form

$$\langle \tilde{v}_r \tilde{v}_\phi \rangle \cong -\chi_\phi \frac{\partial \langle v_\phi \rangle}{\partial r} + \Pi_{r\phi}^{\mathrm{Res}}. \tag{1.1}$$

The residual stress is driven by the background turbulence, i.e., $\Pi_{r\phi}^{\mathrm{Res}} = \Pi_{r\phi}^{\mathrm{Res}}(\nabla n_0, \nabla T_{i,e})$, and can accelerate the plasma from rest via the intrinsic torque $\tau = -\partial_r \Pi_{r\phi}^{\mathrm{Res}}$. The process that the profile gradients drive intrinsic rotations via the residual stress is analogous to a car engine that converts heat flux into the motion of wheels [KDG10a]. $\Pi_{r\phi}^{\mathrm{Res}}$ is also a counterpart of the poloidal residual stress that accelerates poloidal flow [YXD$^+$10a]. The turbulent diffusion of toroidal momentum is also driven by the ambient background turbulence, i.e. $\chi_\phi = \chi_\phi(\nabla n_0, \nabla T_{i,e})$. Thus, as a result of the balance between $\Pi_{r\phi}^{\mathrm{Res}}$ and χ_ϕ, the rotation profile steepens as a secondary effect of the free energy sources (∇n_0, $\nabla T_{i,e}$).

Usually, toroidal rotation is driven by the parallel residual stress $\Pi_{r\|}^{\mathrm{Res}}$ that emerges from $\langle \tilde{v}_r \tilde{v}_\| \rangle$. $\Pi_{r\|}^{\mathrm{Res}}$ is determined by the spectral correlator $\langle k_\theta k_\| \rangle \equiv \sum_k k_\theta k_\| |\phi_k|^2$, which requires symmetry breaking, i.e. spectral imbalance in **k** space [GDHS07a, GDH$^+$10a, MDGH09]. Conventional mechanisms for symmetry breaking are summarized in [DKG$^+$13a]. Most of them are tied to correlating $k_{\|}$ and k_θ via magnetic shear, i.e. $k_{\|} = k_\theta x/L_s$ where $L_s \equiv \hat{s}/Rq$ is the magnetic shear length and x is the distance between the mode center and the rational surface. Ultimately, the correlator is determined by the spatial distribution of the intensity, i.e. $\langle k_\theta k_{\|}\rangle = k_\theta^2 \langle x \rangle / L_s$.

Conventional symmetry breaking mechanisms, and thus models of intrinsic rotation, require finite magnetic shear. However, weak or reversed magnetic shear has long been known to enhance microstability and confinement. Studies on enhanced reversed shear [SBB$^+$97], negative central shear [RTB$^+$96], weakly negative shear [YHN$^+$15], etc. reveal this trend. For example, de-stiffened states, with enhanced confinement, were observed in the weak shear regime in JET [MAC$^+$11a]. In addition, residual stress reversal is observed in computer simulations at weak magnetic shear [LWD$^+$15]. Therefore, intrinsic rotation at weak magnetic shear is of special interest. In particular, there is an open question of what breaks the spectral symmetry absent magnetic shear.

Intrinsic rotation is generated by turbulence. Thus, in tokamaks, intrinsic rotation usually tracks the driving gradient of turbulence [RHD$^+$11a]. This also raises the question of how the flow gradient (∇V_ϕ) interacts with and scales with the driving gradient of turbulence (e.g., edge ion temperature gradient (ITG), in the case of Ref. [RHD$^+$11a]).

1.2.2 Zonal flow

Intrinsic perpendicular flows are often referred to as zonal flows [DIIH05b, GD15, AD16], because they are analogous to zonal flows driven by quasi-geostrophic turbulence [Cha48]. Zonal flows (ZFs) are very effective at regulating drift wave (DW) turbulence, as they are the secondary modes of minimal inertia, transport, and damping [DIIH05b, GD15]. Such a mechanism can be thought of as an element in a 'predator–prey' type ecology [DLCT94, KGD15], in which the secondary 'predator' feeds of (i.e., extracts energy from) the primary 'prey'. In such a system, the damping of the predator (here, the ZF) ultimately regulates the full system.

Frictional drag, due to collisions, is usually invoked to damp ZF. However, this picture is unsatisfactory for present day and future regimes of low collisionality. Thus, an understanding of frictionless ZF saturation and its implications for drift wave turbulence is essential. Of course, ZF saturation significantly impacts transport and turbulence scalings. Note that understanding scalings in the frictionless regime is critical for developing reduced models. As zonal flow shear reduces the turbulent mixing scale, the saturated zonal flow is coupled to the scaling of turbulent diffusivity with $\rho_* \equiv \rho_s/L_n$. This is related to the degree of gyro-Bohm breaking [MPW+01], i.e. the exponent α in $D \sim D_B \rho_*^\alpha$, where $D_B \equiv k_B T/16eB$ is Bohm diffusivity and $\alpha < 1$ indicates gyro-Bohm breaking.

Zonal flow generation has been well-studied [DIIH05b, GD15, GHD15, GD16], but the question of how zonal flows saturate, absent frictional drag, remains open. Though sometimes mentioned in this context, tertiary instability is not effective for most cases of ZF saturation, as it is strongly suppressed by magnetic shear. In simulation studies, the onset of tertiary instability requires an artificial increase in the ZF shearing rate [RDK00] in order to overcome the stabilizing effects of magnetic shear. ITGs can provide an extra source of free energy to drive the tertiary mode, in addition to flow shear. However, such a contribution to the growth rate of the tertiary mode is of order $O(k^2\rho_i^2)$, and thus does not qualitatively alter tertiary stability [KD02]. Tertiary instability of ZF may occur in flat-q regimes [MAC+11a] with zero magnetic shear. Even in this case, the key question of how much turbulent mixing and flow damping result remains to be addressed.

1.3 Turbulence-driven flows in a linear device

Linear devices with zero magnetic shear are testbeds to study the physics of intrinsic flows. It has long been known that the combination of weak magnetic shear and intrinsic toroidal rotation in tokamaks are required for the formation of enhanced confinement states [MAC+11a,

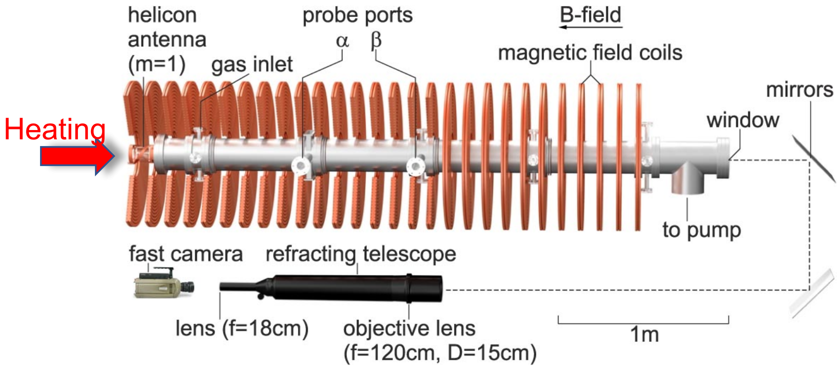

Figure 1.2: Schematic of CSDX.

Table 1.1: Correspondence between CSDX and tokamaks.

Tokamaks	CSDX
Most have sheared magnetic field	Uniform axial magnetic field (shear-free)
Zonal flow in poloidal direction	Zonal flow in azimuthal direction
Intrinsic toroidal rotation	Intrinsic axial flow
Rotation boundary condition set by SOL (scrap-off layer)	Axial flow boundary condition set by boundary neutral layer

RTB$^+$96]. The Controlled Shear Decorrelation Experiment (CSDX) is a cylindrical linear device at University of California San Diego (UCSD) (Fig. 1.2). CSDX has straight magnetic fields, and thus is an important limiting case for understanding turbulence-driven flows at zero shear. Intrinsic axial flows are observed and measured in CSDX [HLH$^+$18]. In addition, CSDX has a long record of zonal flow studies [XTD$^+$11a, YXD$^+$10a]. Therefore, CSDX is an ideal venue to study the generation, saturation, and interaction of intrinsic parallel and perpendicular (zonal) flows at zero magnetic shear. Table 2.1 compares the characteristics of CSDX and tokamak devices.

The axial flow in CSDX is intrinsic. Because neutral gas, as the fuel, is injected radially from the side wall, there is no external source of axial momentum, and so the observed axial flow is intrinsic. In addition, the mean axial flow profile steepens during a global transition triggered for a critical axial magnetic field [CAT$^+$16]. Meanwhile, the steepening of $\nabla\langle v_z\rangle$ tracks that

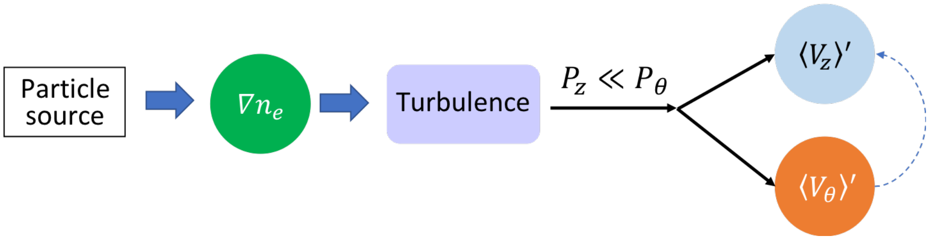

Figure 1.3: Paradigm of the heat engine analogy for the generation of axial and azimuthal flows in CSDX. $P_z \equiv -\langle \tilde{v}_r \tilde{v}_z \rangle' \langle V_z \rangle$ and $P_\theta \equiv -\langle \tilde{v}_r \tilde{v}_\theta \rangle' \langle V_\theta \rangle$ are the axial and azimuthal Reynolds powers.

of ∇n_0 [HLT+16]. This is consistent with the intrinsic axial momentum transport being driven by electron drift wave turbulence. Taken together, this raises the question of what generates the intrinsic axial flow absent magnetic shear. Intrinsic toroidal flows are driven by the residual axial stress Π_{rz}^{Res}, which requires spectral symmetry breaking. However, conventional symmetry breaking mechanisms don't apply to CSDX due to the uniform magnetic field there, i.e. zero magnetic shear.

While the turbulence in CSDX is usually a population of electron drift waves, fluctuations propagating in the ion drift direction are observed [CAT+16]. Such ion features appear in the central region of the cylindrical plasma, where the density profile is flat. ITG turbulence controls momentum transport in tokamaks operated in enhanced confinement states, e.g. states with an internal transport barrier (ITB). Therefore, we are interested in the generation and saturation of intrinsic parallel flows in negative compressibility turbulence (e.g., ITG turbulence) absent magnetic shear. It has long been known that a finite parallel flow shear $\nabla V_\parallel$ can enhance ITG turbulence in sheared magnetic fields [MD88]. However, the detailed question of how the mean flow gradient, $\nabla V_\parallel$, and its perturbation, $\delta V_\parallel'$, affect flow generation and saturation in ITG turbulence in a straight field remains unanswered.

The generation of intrinsic flows is analogous to a heat engine (Fig. 1.3). Initially driven by the free energy source (e.g., ∇n for drift wave turbulence), the turbulence energy is coupled to both azimuthal (zonal) flow and axial flow. Due to its turbulence-driven origin, the axial flow must necessarily be coupled to the azimuthal mean flow. A theoretical framework [HDT] has been proposed to account for the interaction between these two secondary shear flows. However, how to precisely predict what the branching ratio between axial and azimuthal flows remains unknown. Therefore, further studies on how energy is apportioned among the turbulence, azimuthal and axial mean flows are of interest. The dominant branch will have a larger turbulent drive and set the turbulence level through a predator–prey type interaction with turbulent intensity field.

Besides the branching ratio question, the axial and azimuthal flows can interact with each other directly. For a coupled drift–ion acoustic wave system, a zonal flow can arise from the parallel flow compression due to the effects of acoustic coupling [WDH12a]. Especially, when the parallel flow shear is strong enough to trigger parallel shear flow instability (PSFI), the enhanced fluctuating parallel flow compression can act as a source for zonal flow. This mechanism of zonal flow generation differs from conventional models (which depend on the potential vorticity (PV) flux) and has not been tested experimentally. The axial flow shear may also be affected directly by its azimuthal counterpart. In the presence of a finite magnetic shear, the $E_r \times B$ flow shear breaks parallel symmetry and generates a parallel residual stress Π_{rz}^{Res}, which accelerates the axial flow V_z. The effects of azimuthal flows on axial flow generation at zero magnetic shear also remain unclear.

1.4 Organization of chapters

In this thesis, we focus on the mechanism that breaks the spectral symmetry and generates intrinsic axial flows in CSDX. We propose a novel symmetry breaking mechanism to generate intrinsic parallel flows in drift wave turbulence without requiring magnetic shears. This new theoretical finding motivates detailed measurements of symmetry breaking in the microscopic turbulence and how the spectral asymmetry drives macroscopic axial flows in CSDX.

These measurements confirm the new theory of intrinsic axial flow generation. In addition, we study the interaction of intrinsic axial and azimuthal flows in CSDX. We also investigate the saturation of zonal flows in absence of frictional drags.

In Chapter 2, we study the generation of intrinsic axial flows in drift wave turbulence. The observed intrinsic axial flows in CSDX raises the question of what generates the intrinsic axial flow. We seek to understand what breaks the $k_{\|} \to -k_{\|}$ symmetry absent magnetic shear.

In Chapter 3, we study the generation and saturation of intrinsic parallel flows without magnetic shear in the context of ITG turbulence. In particular, we focus on how negative compressibility turbulence, e.g. ITG turbulence, affects momentum transport at zero magnetic shear. The question of how axial flow shear saturates in ITG turbulence is addressed. We also discuss the stiffness of $\nabla V_{\|}$ profile when plotted vs. ∇T_{i0}.

In Chapter 4, we investigate the interaction of intrinsic azimuthal and axial flows in CSDX. We compute the production branching ratio, i.e., the fraction of axial Reynolds power relative to azimuthal Reynolds power. We also show the effects of azimuthal flow shear on the generation and saturation of intrinsic axial flows.

In Chapter 5, we study the phenomenology of intrinsic axial flow and its interaction with azimuthal flows in CSDX. Since the azimuthal (zonal) flow and intrinsic axial flow compete for turbulence energy, the focus is on the interaction of axial and azimuthal flows. Relevant theory and reduced models are also discussed.

The question of what saturates zonal flows absent frictional drag is discussed in Chapter 6. Special focus is on how wave–flow resonance regulates the zonal flow saturation in the frictionless regime and in near-marginal turbulence.

We conclude this thesis by summarizing the results and discussing future direction in Chapter 7.

Chapter 2

Dynamics of Intrinsic Axial Flows in Unsheared, Uniform Magnetic Fields

2.1 Introduction

Toroidal rotation of plasma is beneficial to both macrostability, e.g. the mitigation or stabilization of resistive wall modes [RHS$^+$06], and microstability, by suppressing turbulence via toroidal shear flows that contribute to $E \times B$ shear flows. Plasma rotation and the underlying toroidal angular momentum transport were intensively first studied because neutral beam injection (NBI) was the heating method of choice for tokamaks. Given the fact that unbalanced NBI naturally drives toroidal rotation, and along with the experimental observation that the ion momentum and thermal diffusivities were comparable ($\chi_\phi \sim \chi_i$) [SDF$^+$90], toroidal momentum transport was thought to be diffusive and comparable to the ion heat transport. However, the discovery of the non-diffusive character of toroidal momentum transport in the JFT-2M tokamak [IMM$^+$95] disrupted that overly simple understanding of the toroidal rotation. The paradigm shift was finally triggered by the observation of intrinsic core rotation in the Alcator-C-Mod tokamak, for both Ohmically heated and ion cyclotron resonance frequency driven plasma discharges [RLM$^+$04, LRH$^+$05]. Here, intrinsic rotation means plasma rotation without NBI drives or external wave momentum torque, i.e. self-accelerated rotation. Given the benefits of plasma rotations, the intrinsic rotation is particularly favorable for the International Thermonuclear Experimental Reactor (ITER) where NBI driven rotation is not feasible.

The discovery of intrinsic rotation has elicited interest in the nondiffusive flux (pinch and residual stress) of toroidal momentum which can accelerate the central plasma rotation [DKG$^+$13a]. The momentum pinch, which redistributes the toroidal momentum, contributes little to rotation generation [PAB$^+$11, ACC$^+$12]. Hence, the Reynolds stress has the generic form

$$\langle \tilde{v}_r \tilde{v}_\phi \rangle \cong -\chi_\phi \frac{\partial \langle v_\phi \rangle}{\partial r} + \Pi^{\text{Res}}_{r\phi}. \tag{2.1}$$

The residual stress is driven by the background turbulence, i.e. $\Pi^{\text{Res}}_{r\phi} = \Pi^{\text{Res}}_{r\phi}(\nabla n_0, \nabla T_{i,e})$, and can accelerate the plasma from rest via the intrinsic torque $\tau = -\partial_r \Pi^{\text{Res}}_{r\phi}$. The process that the profile gradients drive intrinsic rotations via the residual stress is analogous to a car engine which converts heat flux into the motion of wheels [KDG10a]. $\Pi^{\text{Res}}_{r\phi}$ is also a counterpart of the poloidal residual stress that accelerates poloidal flow [YXD$^+$10a]. The turbulent diffusion of toroidal momentum is also driven by the ambient background turbulence, i.e. $\chi_\phi = \chi_\phi(\nabla n_0, \nabla T_{i,e})$. Thus, as a result of the balance between $\Pi^{\text{Res}}_{r\phi}$ and χ_ϕ, the rotation profile steepens as a secondary effect of the free energy sources (∇n_0, $\nabla T_{i,e}$). If the rotation profile steepens enough to drive a tertiary instability, i.e. parallel shear flow instability (PSFI) [MD88, RSK04], then $\nabla \langle v_\parallel \rangle$ will act as an additional drive for the turbulent viscosity, i.e. $\chi_\phi = \chi_{\phi,1}(\nabla n_0, \nabla T_{i,e}) + \chi^{\text{PSFI}}_\phi(\nabla \langle v_\parallel \rangle)$. As a consequence, the intrinsic rotation profile is relaxed by the additional viscosity driven by $\nabla \langle v_\parallel \rangle$ because $\langle v_\phi \rangle' \sim \Pi^{\text{Res}}_{r\phi}/(\chi_{\phi,1} + \chi^{\text{PSFI}}_\phi)$. This is somewhat analogous to the zonal flow saturation by tertiary instability (Fig.2.1) [DIIH05b].

Usually, the toroidal rotation is driven by the parallel residual stress $\Pi^{\text{Res}}_{r\parallel}$ that emerges from $\langle \tilde{v}_r \tilde{v}_\parallel \rangle$. $\Pi^{\text{Res}}_{r\parallel}$ is determined by the spectral correlator $\langle k_\theta k_\parallel \rangle \equiv \sum_k k_\theta k_\parallel |\phi_k|^2$ which requires symmetry breaking, i.e. spectral imbalance in **k** space [GDHS07a, GDH$^+$10a, MDGH09]. Con-

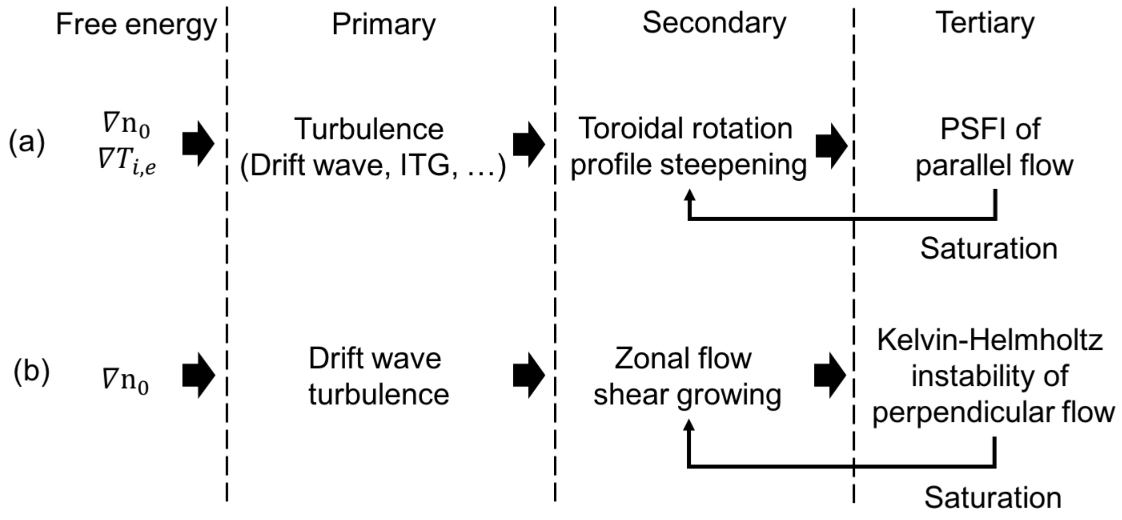

Figure 2.1: Primary, secondary, and tertiary effects of free energy sources on (a) intrinsic rotation and (b) zonal flow.

ventional mechanisms for symmetry breaking are summarized in [DKG$^+$13a]. Most of them are tied to correlating $k_\parallel$ and k_θ via magnetic shear, i.e. $k_\parallel = k_\theta x/L_s$ where $L_s \equiv \hat{s}/Rq$ is the magnetic shear length and x is the distance between the mode center and the rational surface. Ultimately, the correlator is determined by the spatial distribution of the intensity, i.e. $\langle k_\theta k_\parallel \rangle = k_\theta^2 \langle x \rangle / L_s$.

Conventional symmetry breaking mechanisms, and thus models of intrinsic rotation, require finite magnetic shear. However, residual stress reversal is observed in computer simulations at weak magnetic shear [LWD$^+$15]. Moreover, experimental results suggest that a control knob for intrinsic rotation is the magnitude of safety factor q_0 rather than the magnetic shear [RPR$^+$13]. Recently, intrinsic parallel flows were observed in a linear device with uniform magnetic field (zero magnetic shear), the Controlled Shear Decorrelation Experiment (CSDX) (Fig.2.2) [TBC$^+$14b]. Some of the correspondence between CSDX and tokamaks is summarized in Table 2.1, more of which can be found in [CAT$^+$16]. Because neutral gas, as the fuel, is injected radially from the side wall, there is no external source of axial momentum, and so the observed axial flow is intrinsic. In addition, mean axial flow profile steepens during a global transition triggered for a critical axial magnetic field [CAT$^+$16]. Meanwhile, the steepening of

Table 2.1: Correspondence between the linear device, CSDX and tokamaks.

Tokamaks	CSDX
Most have sheared magnetic field	Uniform axial magnetic field (shear-free)
Intrinsic toroidal rotation	Intrinsic axial flow
Rotation boundary condition set by SOL	Axial flow boundary condition set by boundary neutral layer

$\nabla\langle v_z\rangle$ tracks that of ∇n_0 [HLT$^+$16]. This is consistent with that the intrinsic axial momentum transport is driven by electron drift wave turbulence.

The observed intrinsic axial flows in CSDX raises two questions: 1) what generates the intrinsic axial flow; 2) what determines the mean axial flow profile? Intrinsic toroidal flows are driven by the residual axial stress Π_{rz}^{Res}, which requires spectral symmetry breaking. However, conventional symmetry breaking mechanisms don't apply to CSDX due to the uniform magnetic field there, i.e. zero magnetic shear. Motivated by these observations, in this paper, we propose a new dynamical symmetry breaking mechanism which doesn't require a specific magnetic field structure. In this model, we consider a drift wave system with weakly nonadiabatic electrons ($\tilde{n}_e/n_0 = (1-i\delta)\widetilde{\phi}$ with $0<\delta\ll 1$) in presence of finite axial flow shear. By dynamical symmetry breaking, we mean that a small but finite perturbation to the mean axial flow profile can break the symmetry and the resulting turbulence spectral imbalance sets a finite residual stress. The residual stress driven intrinsic flow then adds to the initial flow profile perturbation. Therefore, the flow profile perturbation is self-amplified via a closed feedback loop, as in a modulational instability. The residual stress gives rise to a momentum flux with a negative diffusivity, $\Pi_{rz}^{\text{Res}} \sim |\chi_\phi^{\text{Res}}|\langle v_z\rangle'$, inducing a negative increment ($-|\chi_\phi^{\text{Res}}|$) to the ambient turbulent viscosity (χ_ϕ). Hence, the dynamical symmetry breaking is essentially a negative viscosity phenomenon. The growth of axial flow shear by the dynamical symmetry breaking is analogous to the modulational growth of zonal flow shear [DIIH05b].

The mean axial flow can be driven by an axial ion pressure drop and is enhanced by

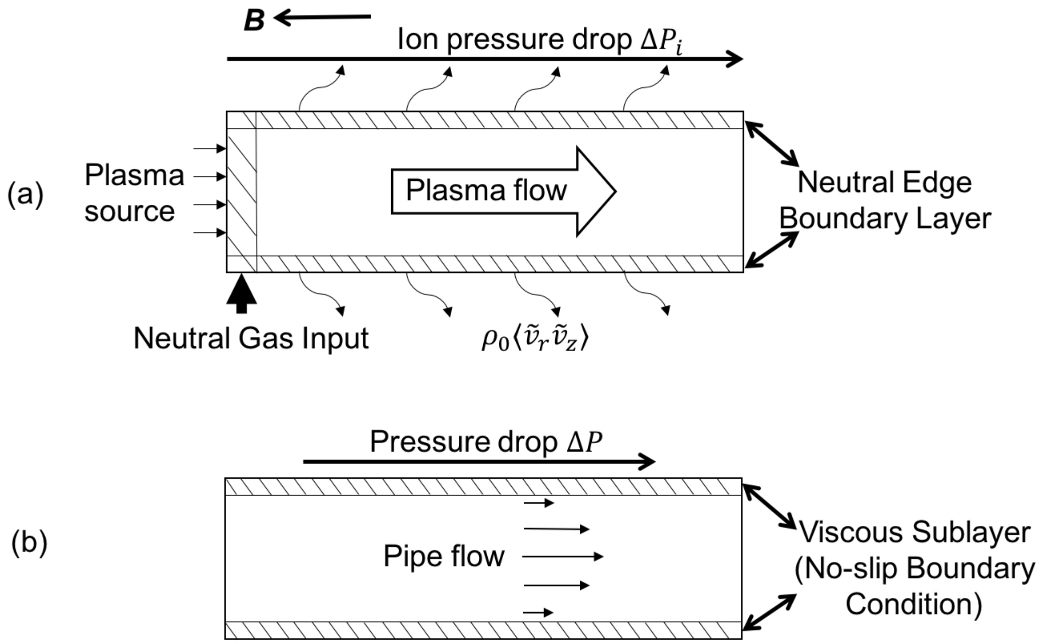

Figure 2.2: (a) Sketch of axial plasma flow in CSDX in analogy to (b) turbulent pipe flow.

the negative viscosity. As shown in Fig.2.2, the helicon source on the left end of the cylinder makes the nearby plasma hotter than the plasma near the endplate, thus giving rise to an axial ion pressure drop, $\Delta P_i = P_i|_{\text{Source}} - P_i|_{\text{Endplate}}$. Hence, in analogy to the turbulent hydrodynamic pipe flows, the axial plasma flow in a linear device is driven by ΔP_i and dissipated by the total viscosity, consisting of both the ambient turbulent viscosity and the negative viscosity increment induced by the residual stress, i.e. $\langle v_z\rangle' \sim \Delta P_i/(\chi_\phi - |\chi_\phi^{\text{Res}}|)$. Therefore, with external excitation (e.g. ΔP_i), a total negative viscosity is *not* needed to generate axial flows, and $\langle v_z\rangle'$ is enhanced by $-|\chi_\phi^{\text{Res}}|$. In addition, boundary conditions must be considered to determine the mean flow profile [AGG+13]. In CSDX, the boundary layer is dominated by neutral flows (Fig.2.2). The outer region of the cylindrical plasma is only partially ionized, and the neutral momentum is coupled to the plasma momentum via the ionization and recombination processes within the boundary layer. Thus, the neutral dynamics in the boundary layer plays a role in the boundary conditions for the plasma flow in the center.

Driven by electron drift wave turbulence with no requirement for magnetic field ge-

Table 2.2: Compare and contrast the dynamical symmetry breaking with conventional symmetry breaking mechanisms.

	Standard Symmetry Breaking	Dynamical Symmetry Breaking
Free energy	$\nabla T_i, \nabla n_0, \ldots$	∇n_0
Symmetry breaker	$E_r', I(x)', \ldots$ All tied to magnetic field configuration	Test axial flow shear, $\delta\langle v_z\rangle'$; No requirement for shear of $\boldsymbol{B}$ structure.
Effect on flow	Intrinsic torque, $-\partial_r \Pi_{r\parallel}^{Res}$	Negative viscosity, $-\lvert\chi^{Res}\rvert$ driven by ∇n_0
Flow profile	$\langle v_\parallel\rangle' = \dfrac{\Pi_{r\parallel}^{Res}}{\chi_\phi}$	$\langle v_z\rangle' = \dfrac{\text{Flow drive (e.g. } \Pi_{rz}^{Res}, \Delta P_i)}{\chi_\phi(\nabla N_0, \nabla\langle v_z\rangle) - \lvert\chi_\phi^{Res}\rvert}$
Feedback loop	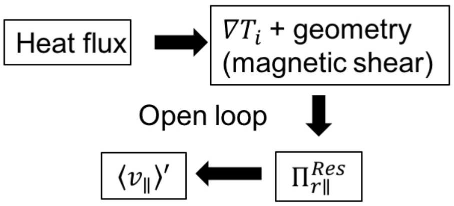	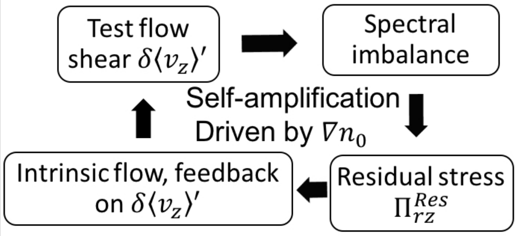

ometry, the dynamical symmetry breaking is applicable to intrinsic rotation in flat q regions [MAC$^+$11a, dVRG$^+$06] where conventional models fail, as well as to intrinsic rotation in plasmas where the electron channel (and thus CTEM) is dominant. Also, a total negative viscosity, as well as the underlying modulational growth of test flow shear, is not needed to generate intrinsic rotation at normal magnetic shears, because the residual stress determined by conventional symmetry breaking mechanisms can accelerate the plasma. Therefore, the profile gradient of intrinsic toroidal rotation is *enhanced* by the negative viscosity induced by the dynamical symmetry breaking, i.e. $\langle v_\parallel\rangle' \sim \Pi_{r\parallel}^{\text{Res}}/(\chi_\phi - |\chi_\phi^{\text{Res}}|)$.

To summarize, the new dynamical symmetry breaking mechanism discussed here is outside the domain of conventional models of residual stress. The contrast and comparison are summarized in Table 2.2. The dynamical symmetry breaking is different in two ways: (1) Intrinsic flow is generated by the self-amplification of a test or seed flow shear. This process is driven fundamentally by ∇n_0, i.e. as in a modulational instability of drift waves, similar to the modulational growth of zonal flow shear. (2) Instead of an intrinsic torque that accelerates the flow, the dynamical symmetry breaking mechanism yields a residual stress which induces a negative increment to the ambient turbulent viscosity that enhances the mean flow profile gradient.

The rest of this paper is organized as follows: Sec.5.2 introduces the derivation of the drift wave system coupled to axial flow fluctuations in the weakly nonadiabatic limit; Sec.2.3 discusses the dynamical symmetry breaking mechanism; Sec.2.4 elaborates the negative viscosity induced by the residual stress; the total axial flow structure is calculated and discussed in Sec.2.5; Sec.2.6 gives the implications for tokamaks of dynamical symmetry breaking; Sec.6.4 summarizes and discusses the results.

2.2 Physics Model

We consider a system consisting of electron density, electron axial momentum, charge balance, and plasma axial flow in cylindrical geometry where magnetic field is uniform in the axial direction:

$$\frac{\mathrm{D}\tilde{n}_e}{\mathrm{D}t} + \mathbf{v}_E \cdot \nabla n_0 + n_0 \frac{\partial \tilde{v}_e}{\partial z} = 0, \tag{2.2}$$

$$m_e n_0 \frac{\mathrm{D}}{\mathrm{D}t} \tilde{v}_e = e n_0 \frac{\partial \tilde{\phi}}{\partial z} - \frac{\partial \tilde{p}_e}{\partial z} - \nu_{\mathrm{ei}} m_e n_0 \tilde{v}_e, \tag{2.3}$$

$$\nabla_\perp \cdot \mathbf{j}_\perp = -\frac{\partial j_z}{\partial z}, \tag{2.4}$$

$$\frac{\mathrm{D}}{\mathrm{D}t} \tilde{v}_z + \mathbf{v}_E \cdot \nabla \langle v_z \rangle = -\frac{\partial \tilde{p}_e}{\partial z}. \tag{2.5}$$

Here, $\mathrm{D}/\mathrm{D}t \equiv \partial_t + \mathbf{v}_E \cdot \nabla$ is the convective time derivative and $\mathbf{v}_E = \hat{z} \times \nabla \tilde{\phi}$ is the $E \times B$ drift velocity. In the following analysis, it is convenient to normalize the quantities as follows: $\tilde{n} \equiv \tilde{n}_e / n_0$, $\tilde{\phi} \equiv e\tilde{\phi}/T_e$, length $\equiv$ length$/\rho_s$, $t \equiv t/\omega_{ci}$, $\tilde{v}_z \equiv \tilde{v}_z / c_s$, where $c_s \equiv \sqrt{T_e/m_i}$ is the ion acoustic speed, $\omega_{ci} \equiv eB/m_i$ is the ion cyclotron frequency, and $\rho_s \equiv c_s/\omega_{ci}$. The perpendicular current is set by the polarization current $\mathbf{j}_\perp = -n_0 \frac{D}{Dt} \nabla_\perp \tilde{\phi}$, while the axial current is $j_z = n_0(\tilde{v}_z -$

$\tilde{v}_e)$. Thus, the electron flow is cancelled by subtracting Eq.(2.4) from Eq.(6.1)

$$\frac{\mathrm{D}}{\mathrm{D}t}\left(\tilde{n}-\nabla_\perp^2\tilde{\phi}\right)+\frac{1}{L_n}\frac{1}{r}\frac{\partial\tilde{\phi}}{\partial\theta}+\frac{\partial\tilde{v}_z}{\partial z}=0, \tag{2.6}$$

where $L_n \equiv -(d\ln n_0/dr)^{-1}$ is the density profile gradient length. Ion pressure fluctuation is neglected in the flow equation, since $\tilde{p}_i \ll \tilde{p}_e$. In the presence of a finite mean axial flow shear $\langle v_z\rangle'$, the axial flow momentum equation becomes

$$\frac{\mathrm{D}}{\mathrm{D}t}\tilde{v}_z-\langle v_z\rangle'\frac{1}{r}\frac{\partial\tilde{\phi}}{\partial\theta}=-\frac{\partial\tilde{n}}{\partial z}, \tag{2.7}$$

where the thermal fluctuations of electrons are ignored, such that $\tilde{p}_e = T_e\tilde{n}$. To close the system, the electron density fluctuation needs to be evaluated. The electron response is nearly adiabatic, i.e. $\tilde{n}=(1-i\delta)\tilde{\phi}$ with $\delta \ll 1$, given by Eq.(6.1)(2.3). The electron axial momentum is damped by electron-ion collisions. With the electrons in the thermal equilibrium state $\nu_{\mathrm{ei}} \gg \omega$, the inertia term in Eq.(2.3) can be neglected. As a consequence, the electron current is driven by the nonadiabatic electrons

$$\tilde{v}_e=-\frac{v_{\mathrm{The}}^2}{\nu_{\mathrm{ei}}}\frac{\partial}{\partial z}\left(\tilde{n}-\tilde{\phi}\right). \tag{2.8}$$

In the weakly nonadiabatic limit, $1 < k_z^2 v_{\mathrm{The}}^2/(\nu_{\mathrm{ei}}\omega_k) < \infty$. Plugging the electron current into the electron density equation, the nonadiabatic electron response is then given by

$$\delta \cong \frac{\nu_{\mathrm{ei}}(\omega_* - \omega_k)}{k_z^2 v_{\mathrm{The}}^2}, \tag{2.9}$$

where $\omega_* \equiv k_\theta\rho_{\mathrm{s}}c_{\mathrm{s}}/L_n$ is the electron drift frequency. In the weakly nonadiabatic limit, $0 < \delta \ll 1$. For adiabatic electrons, $k_z^2 v_{\mathrm{The}}^2/(\nu_{\mathrm{ei}}\omega_k) \to \infty$, then $\delta \to 0$ and $\tilde{n} \to \tilde{\phi}$. Finally, we arrive at the drift wave system with weakly nonadiabatic electrons coupled to the axial flow fluctuations

$$\frac{\mathrm{D}}{\mathrm{D}t}(1-i\delta-\nabla_\perp^2)\tilde{\phi}+\frac{1}{L_n}\frac{1}{r}\frac{\partial\tilde{\phi}}{\partial\theta}+\frac{\partial\tilde{v}_z}{\partial z}=0, \tag{2.10}$$

$$\frac{\mathrm{D}}{\mathrm{D}t}\tilde{v}_z - \langle v_z \rangle' \frac{1}{r}\frac{\partial\tilde{\phi}}{\partial\theta} = -(1-i\delta)\frac{\partial\tilde{\phi}}{\partial z}, \tag{2.11}$$

with δ given by Eq.(2.9). This system gives two instabilities: electron drift wave instability and parallel shear flow instability (PSFI). The electron drift wave is unstable in the presence of nonadiabatic electrons and is driven by ∇n_0. Next, we'll briefly discuss the PSFI in the presence of nearly adiabatic electrons.

PSFI is driven by $\nabla\langle v_z \rangle$ and is essentially a negative compressibility phenomenon. The dispersion relation for the coupled system Eq.(6.2)(2.11) is

$$1 + k_\perp^2\rho_\mathrm{s}^2 - i\delta - \frac{\omega_*}{\omega} + \frac{k_\theta k_z \rho_\mathrm{s} c_\mathrm{s} \langle v_z \rangle'}{\omega^2} - (1-i\delta)\frac{k_z^2 c_\mathrm{s}^2}{\omega^2} = 0, \tag{2.12}$$

where $0 < \delta \ll 1$ in the weakly nonadiabatic limit. As a quadratic equation of ω, Eq.(4.10) gives unstable solution when the mean flow shear $\langle v_z \rangle'$ exceeds a critical value

$$\langle v_z \rangle'_\mathrm{crit} = \frac{1}{k_\theta k_z \rho_\mathrm{s} c_\mathrm{s}}\left[\frac{\omega_*^2(1+k_\perp^2\rho_\mathrm{s}^2)}{4[(1+k_\perp^2\rho_\mathrm{s}^2)^2+\delta^2]} + k_z^2 c_\mathrm{s}^2\right], \tag{2.13}$$

such that the discriminant is negative. If the drift wave branch is neglected, the dispersion relation Eq.(4.10) supports a modified ion acoustic wave

$$\omega^2 \sim \gamma^\mathrm{eff} k_z^2 c_\mathrm{s}^2 \tag{2.14}$$

with the effective compressibility of the axial flow as:

$$\gamma^\mathrm{eff} = \frac{1}{1+k_\perp^2\rho_\mathrm{s}^2}\left(1 - \frac{k_\theta \langle v_z \rangle'}{k_z \omega_\mathrm{ci}}\right). \tag{2.15}$$

When the axial flow shear is large enough such that the compressibility becomes negative, the modified ion acoustic wave is driven unstable. Therefore, the PSFI is driven by negative compressibility.

With the coupled drift wave system in the weakly nonadiabatic limit, next, we'll show how this system breaks the spectral symmetry of the drift wave turbulence.

2.3 Dynamical Symmetry Breaking

Consider the axial flows in a linear cylindrical plasma. The dynamics of the mean axial flow is governed by

$$\frac{\partial\langle v_z\rangle}{\partial t}+\frac{\partial\langle\tilde{v}_r\tilde{v}_z\rangle}{\partial r}=-\frac{1}{\rho_0}\frac{\partial P_i}{\partial z}-\nu_{ni}(\langle v_z\rangle-\langle v_{z,n}\rangle). \tag{2.16}$$

The mean ion pressure drops in the axial direction due to the axially inhomogeneous ion temperature (Fig.2.2) and thus can drive a mean flow $\langle v_z\rangle$, even though its fluctuation was neglected in the fluctuation equation of axial flow. While ΔP_i drives the axial flow in the center region, the boundary layer is controlled by the collisional coupling between plasma flows ($\langle v_z\rangle$) and neutral flows ($\langle v_{z,n}\rangle$). The generic form of the Reynolds stress is given by

$$\langle\tilde{v}_r\tilde{v}_z\rangle=-\chi_\phi\frac{\partial\langle v_z\rangle}{\partial r}+\Pi_{rz}^{\mathrm{Res}}. \tag{2.17}$$

The momentum pinch is ignored because (1) there is no toroidal effect in the linear device, where the magnetic fields lines are straight and uniform, and (2) the pinch effect is responsible for redistribution of the axial momentum but not for generation.

To calculate the Reynolds stress $\langle\tilde{v}_r\tilde{v}_z\rangle$, linearize Eq.(2.11) to get the linear response for the axial velocity fluctuation $\tilde{v}_z$, and $\tilde{v}_r$ is the fluctuation of the radial $E\times B$ velocity. The quasilinear Reynolds stress is then determined by the cross phase between $\tilde{v}_r$ and $\tilde{v}_z$,

$$\langle\tilde{v}_r\tilde{v}_z\rangle=-\sum_k\frac{|\gamma_k|}{\omega_k^2}k_\theta^2\rho_s^2|\phi_k|^2\langle v_z\rangle'+\sum_k\left(\frac{|\gamma_k|}{\omega_k^2}+\frac{\delta}{\omega_k}\right)k_\theta k_z\rho_s c_s|\phi_k|^2, \tag{2.18}$$

where γ_k and ω_k arise from the drift wave system. The residual stress (the second term in Eq.(2.18)) is determined by the correlator, i.e. $\Pi_{rz}^{\mathrm{Res}} \sim \langle k_\theta k_z \rangle \equiv \sum_k k_\theta k_z |\phi_k|^2$ which requires spectral imbalance, due to correlated $\tilde{v}_r$ and $\tilde{v}_z$ flucturations.

The coupled system described by Eq.(6.2)-(2.11) is controlled by drift wave modes when $\langle v_z \rangle'$ is below the PSFI threshold. This drift wave dominated system is unstable due to nonadiabatic electrons (which set the cross phase between electron density perturbation and electrostatic potential perturbation). Specifically, the linear growth rate is set by the weakly nonadiabatic electron density perturbation as

$$\gamma_k \cong \omega_* \delta / (1 + k_\perp^2 \rho_s^2)^2, \tag{2.19}$$

given by the dispersion relation Eq.(4.10) with the ion-acoustic branch neglected. With δ given by Eq.(2.9), the linear growth rate of the collisional drift wave is then set by the frequency shift from the electron drift frequency

$$\gamma_k \cong \frac{\nu_{\mathrm{ei}}}{k_z^2 v_{\mathrm{The}}^2} \frac{\omega_* (\omega_* - \omega_k)}{(1 + k_\perp^2 \rho_s^2)^2}. \tag{2.20}$$

The frequency of the system is controlled by the electron drift frequency with a shift set by the mean axial flow shear

$$\omega_k \cong \frac{\omega_*}{1 + k_\perp^2 \rho_s^2} - \frac{k_\theta k_z \rho_s c_s \langle v_z \rangle'}{\omega_*}. \tag{2.21}$$

Consequently, the full expression for the growth rate is

$$\gamma_k \cong \frac{\nu_{\mathrm{ei}}}{k_z^2 v_{\mathrm{The}}^2} \frac{\omega_*^2}{(1 + k_\perp^2 \rho_s^2)^2} \left(\frac{k_\perp^2 \rho_s^2}{1 + k_\perp^2 \rho_s^2} + \frac{k_\theta k_z \rho_s c_s \langle v_z \rangle'}{\omega_*^2} \right). \tag{2.22}$$

With ∇n_0 as the free energy source, a finite mean axial flow shear can break the symmetry of the background drift wave turbulence. For a flat mean axial flow profile, i.e. $\langle v_z \rangle' = 0$, the growth rate given by Eq.(5.12) is symmetric for $k_z \to -k_z$. The resulting turbulence spectrum is

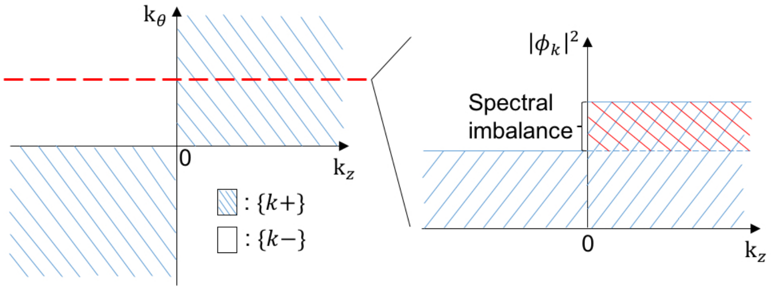

Figure 2.3: Spectral imbalance in $k_\theta k_z$ space.

consequently expected to be symmetric in $\mathbf{k}$ space, giving $\Pi_{rz}^{\text{Res}} \sim \langle k_\theta k_z \rangle = 0$. The momentum diffusion is also zero for the flat mean flow profile. Therefore, the mean axial flow profile is stationary and stays flat. However, a small but finite perturbation to the mean flow profile, e.g. $\delta \langle v_z \rangle' > 0$, breaks the symmetry of the background turbulence. With larger linear growth rates, modes with $k_\theta k_z > 0$, whose frequencies shift further away from ω_*, grow faster than the other modes. The drift wave turbulence intensity is then unbalanced in $k_\theta k_z$ space (Fig.2.3). Hence, k_θ and k_z are correlated by the spectral imbalance, and so form a finite residual stress, since $\Pi_{rz}^{\text{Res}} \sim \langle k_\theta k_z \rangle > 0$. This residual stress amplifies the initial test flow shear, closing the feedback loop for the self-amplification of test flow shear (Table 2.2).

Given the drift wave instability in the background and the spectral imbalance resulting from the symmetry breaking, the Reynolds stress can be calculated. The first term in the Reynolds stress Eq.(2.18) is a diffusive axial momentum flux, with the turbulent viscosity

$$\chi_\phi \cong \sum_k \frac{\nu_{\text{ei}}}{k_z^2 v_{\text{The}}^2} \frac{k_\perp^2 \rho_s^2}{1 + k_\perp^2 \rho_s^2} k_\theta^2 \rho_s^2 |\phi_k|^2. \tag{2.23}$$

This turbulent viscosity is driven by the ambient background turbulence. So for the drift wave turbulence dominated case, χ_ϕ is driven primarily by ∇n_0. Additionally, as will be discussed later, the PSFI will enter when $\langle v_z \rangle' > \langle v_z \rangle'_{\text{crit}}$. Then, the turbulent viscosity is driven by both density gradient and the mean flow gradient, i.e. $\chi_\phi = \chi_\phi^{\text{DW}} (\nabla n_0) + \chi_\phi^{\text{PSFI}} (\nabla \langle v_z \rangle) \Theta(\langle v_z \rangle' - \langle v_z \rangle'_{\text{crit}})$, where $\Theta(x)$ is a Heaviside step function, acting as a switch for the onset of PSFI driven turbulence.

The off-diagonal flux in Eq.(2.18) is the residual stress

$$\Pi_{rz}^{\mathrm{Res}} \cong \sum_k \frac{\nu_{\mathrm{ei}}}{k_z^2 v_{\mathrm{The}}^2}(2+k_\perp^2\rho_\mathrm{s}^2)\left[\underbrace{\frac{k_\perp^2\rho_\mathrm{s}^2}{1+k_\perp^2\rho_\mathrm{s}^2}}_{①}+\underbrace{\frac{k_\theta k_z \rho_\mathrm{s} c_\mathrm{s}\langle v_z\rangle'}{\omega_*^2}}_{②}\right] k_\theta k_z \rho_\mathrm{s} c_\mathrm{s} |\phi_k|^2. \qquad (2.24)$$

Π_{rz}^{Res} is dominated by term ① when $\langle v_z\rangle'$ is below the PSFI threshold. Hence, in the presence of a finite test axial flow shear, the spectral imbalance in Fig.2.3 gives rise to the residual stress

$$\Pi_{rz}^{\mathrm{Res}} = \mathrm{sgn}(\delta\langle v_z\rangle') \sum_{\{k+\}} \frac{\nu_{\mathrm{ei}}}{k_z^2 v_{\mathrm{The}}^2}(2+k_\perp^2\rho_\mathrm{s}^2)\frac{k_\perp^2\rho_\mathrm{s}^2}{1+k_\perp^2\rho_\mathrm{s}^2}|k_\theta k_z|\rho_\mathrm{s} c_\mathrm{s} \Delta I_k(\delta\langle v_z\rangle'), \qquad (2.25)$$

where $\Delta I_k(\delta\langle v_z\rangle') = |\phi_k|^2|_{\{k+\}} - |\phi_k|^2|_{\{k-\}}$ accounts for the spectral imbalance. On account of the symmetry breaking term in the growth rate Eq.(5.12), the residual stress has the same sign as $\delta\langle v_z\rangle'$. Moreover, Π_{rz}^{Res} depends explicitly on the mean axial flow shear via term ② in Eq.(4.18) as well as via the spectral imbalance. Term ② $\sim \sum_k k_\theta^2/\omega_*^2|\phi_k|^2\delta\langle v_z\rangle' = L_n^2\sum_k |\phi_k|^2\delta\langle v_z\rangle'$ doesn't require symmetry breaking and enters in the form of a negative diffusion. *Therefore, a negative viscosity increment is induced by the residual stress.*

It should be noted that the dependence of residual stress upon $\delta\langle v_z\rangle'$ cannot be absorbed by the diffusive component of the Reynolds stress for 3 reasons: (1) the magnitude of residual stress is dominated by term ① of Eq.(4.18) which is independent of $\delta\langle v_z\rangle'$; (2) the spectral imbalance is induced via both linear growth and nonlinear saturation of modes, so $\Delta I_k(\delta\langle v_z\rangle')$ and thus Π_{rz}^{Res} are essentially nonlinear in $\delta\langle v_z\rangle'$; (3) even the term linear in $\delta\langle v_z\rangle'$ results in a negative diffusive flux rather than a positive, downgradient diffusion. The induced negative viscosity can give rise to the modulational growth of the test flow shear, as will be shown in the next section.

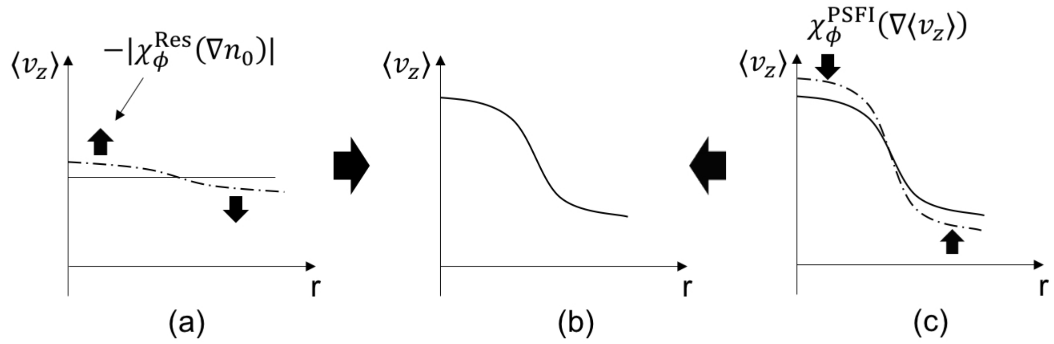

Figure 2.4: Modulational growth of the test flow shear. (a) Perturbation to the axial flow profile is self-amplified by the modulational instability driven by residual stress induced negative viscosity $-|\chi_\phi^{\mathrm{Res}}(\nabla n_0)|$. (b) The test flow shear is amplified into a macroscopic profile. (c) When the axial flow shear hits the PSFI threshold, the additional $\chi_\phi^{\mathrm{PSFI}}(\nabla \langle v_z \rangle)$ relaxes the flow profile, keeping $\langle v_z \rangle'$ at or below $\langle v_z \rangle'_{\mathrm{crit}}$.

2.4 Negative Viscosity

The dynamical symmetry breaking mechanism is essentially the self-amplification of test flow shear, driven by drift wave turbulence, which is similar to the modulational growth of zonal flow shear. In this section, the growth and saturation of the test flow shear are considered. The modulational growth of the test flow shear is illustrated by the cartoon in Fig.2.4. The dynamics of the test flow shear is a diffusion process with the turbulent viscosity as the effective diffusivity. We will show that the residual stress induces a negative increment to the ambient turbulent viscosity. Thus, the total viscosity is $\chi_\phi^{\mathrm{tot}} = \chi_\phi - |\chi_\phi^{\mathrm{Res}}|$. When $|\chi_\phi^{\mathrm{Res}}|$ is strong enough such that the total viscosity becomes negative, the test flow shear will grow until the flow shear hits the PSFI threshold given by Eq.(4.13). Then, the additional turbulent viscosity induced by PSFI turbulence makes the total viscosity positive and stops the growth of the test flow shear. $\langle v_z \rangle'_{\mathrm{crit}}$ thus sets an effective upper limit for the profile gradient of axial flow.

The dynamics of the test flow shear can be derived from Eq.(2.16)

$$\frac{\partial \delta \langle v_z \rangle'}{\partial t} + \frac{\partial^2}{\partial r^2}\left(-\chi_\phi \delta \langle v_z \rangle' + \delta \Pi_{rz}^{\mathrm{Res}}\right) = 0. \tag{2.26}$$

Without the perturbed residual stress, the dynamics of the test flow shear is a diffusion process with the flow shear flux $\Gamma_{\delta\langle v_z\rangle'} = -\chi_\phi \partial_r \delta\langle v_z\rangle'$. Next, we'll show that the residual stress due to the perturbed axial flow shear induces a momentum flux with a negative diffusivity. The test flow shear flux is then modified by the negative increment of momentum diffusivity.

To do this, we begin by calculating the perturbed residual stress. Given by Eq.(2.18), the residual stress explicitly depends on the flow shear through the growth rate and the frequency. Moreover, the turbulence intensity depends on the flow shear because of the spectral imbalance induced by $\langle v_z\rangle'$. Therefore, it is convenient to write the turbulence intensity in terms of the wave action density, which is, by definition, $N_k \equiv \varepsilon_k/\omega_k$. Here, the wave energy of the electron drift wave is $\varepsilon_k = \frac{1}{2}(1+k_\perp^2\rho_s^2)^2|\phi_k|^2$ [WDH12b]. Consequently, the perturbed residual stress due to the test flow shear can be written as $\delta\Pi_{rz}^{\mathrm{Res}} = \delta\Pi_{rz}^{\mathrm{Res}}\left(\delta\gamma_k, \delta\omega_k, \delta N_k\right)$. The perturbed growth rate and perturbed frequency are calculated directly from Eq.(2.21)-(5.12), while the perturbed wave action density due to the axial flow profile perturbation is calculated as follows.

The wave action density $N_k \equiv \varepsilon_k/\omega_k$ is essentially the population of waves with wave number $\mathbf{k}$. Its dynamics is governed by the wave kinetic equation

$$\frac{\partial N_k}{\partial t} + v_{gr}\frac{\partial N_k}{\partial r} - \frac{\partial}{\partial r}\left(\omega_k + \mathbf{k}\cdot\mathbf{V}\right)\frac{\partial N_k}{\partial k_r} = \gamma_k N_k - \Delta\omega_k \frac{N_k^2}{N_0}. \tag{2.27}$$

We separate the perturbation, due to test flow shear, from the slowly varying mean wave action density, i.e. $N_k = \delta N_k + \langle N_k\rangle$. The linearized equation for δN_k is then

$$\frac{\partial \delta N_k}{\partial t} + \delta v_{gr}\frac{\partial\langle N_k\rangle}{\partial r} - \frac{\partial}{\partial r}\delta\left(\omega_k + \mathbf{k}\cdot\mathbf{V}\right)\frac{\partial\langle N_k\rangle}{\partial k_r} = \gamma_k\delta N_k + \delta\gamma_k\langle N_k\rangle - 2\Delta\omega_k\delta N_k. \tag{2.28}$$

The convection by the wave packet motion vanishes because

$$\frac{\delta v_{gr}}{\delta\langle v_z\rangle'} = \frac{\delta(\partial\omega_k/\partial k_r)}{\delta\langle v_z\rangle'} = 0,$$

where only the linear frequency shift is considered. Ignoring the zonal flow effects, since there is no coupling between k_θ and k_z by geometry, the refraction term becomes

$$\frac{\partial}{\partial r}\delta\left(\omega_k+\mathbf{k}\cdot\mathbf{V}\right)\frac{\partial N_k}{\partial k_r}=\left(\frac{\partial\delta\omega_k}{\partial r}+k_z\delta\langle v_z\rangle'\right)\frac{\partial\langle N_k\rangle}{\partial k_r}. \tag{2.29}$$

The shearing of the frequency perturbation is calculated from Eq.(2.21)

$$\frac{\partial\delta\omega_k}{\partial r}=k_z\delta\langle v_z\rangle'\left(\frac{L_n^2}{n_0}\frac{\partial^2 n_0}{\partial r^2}-1\right). \tag{2.30}$$

Thus, the perturbation to the refraction term is driven by the density profile curvature

$$\delta\left\{\frac{\partial}{\partial r}\left(\omega_k+\mathbf{k}\cdot\mathbf{V}\right)\frac{\partial N_k}{\partial k_r}\right\}=k_z\delta\langle v_z\rangle'\frac{L_n^2}{n_0}\frac{\partial^2 n_0}{\partial r^2}\frac{\partial\langle N_k\rangle}{\partial k_r}. \tag{2.31}$$

Here, we consider the drift wave turbulence with finite ∇n_0, so the effect of $\partial n_0/\partial r$ is dominant over that of $\partial^2 n_0/\partial r^2$, and thus the above curvature driven term (Eq.2.31) can be neglected. Therefore, δN_k is driven by the linear growth and nonlinear self-interaction of drift waves

$$\frac{\partial\delta N_k}{\partial t}=\gamma_k\delta N_k+\delta\gamma_k\langle N_k\rangle-2\Delta\omega_k\delta N_k. \tag{2.32}$$

The steady state perturbation is then given by

$$\delta N_k=\frac{\delta\gamma_k}{2\Delta\omega_k-\gamma_k}\langle N_k\rangle, \tag{2.33}$$

where the decorrelation rate $\Delta\omega_k\cong\gamma_k$ is determined by the steady state equilibrium, $\langle N_k\rangle$. Finally, with the perturbed growth rate calculated from Eq.(5.12), the perturbed wave action density due to the test flow shear is

$$\delta N_k=\frac{1+k_\perp^2\rho_s^2}{k_\perp^2\rho_s^2}\frac{k_\theta k_z\rho_s c_s\delta\langle v_z\rangle'}{\omega_*^2}\langle N_k\rangle. \tag{2.34}$$

Thus, the perturbed residual stress due to the test flow shear takes the form of a negative diffusive flux of axial momentum

$$\delta\Pi_{rz}^{\mathrm{Res}} \equiv -\chi_{\phi}^{\mathrm{Res}}\delta\langle v_z\rangle', \tag{2.35}$$

with the negative viscosity

$$\chi_{\phi}^{\mathrm{Res}} = -\frac{\nu_{\mathrm{ei}}L_n^2}{v_{\mathrm{The}}^2}\sum_k(1+k_{\perp}^2\rho_{\mathrm{s}}^2)(4+k_{\perp}^2\rho_{\mathrm{s}}^2)|\phi_k|^2 \tag{2.36}$$

related to Π_{rz}^{Res} by dynamical symmetry breaking. Therefore, the test flow shear dynamics is a diffusion process

$$\frac{\partial\delta\langle v_z\rangle'}{\partial t} - \frac{\partial^2}{\partial r^2}\chi_{\phi}^{\mathrm{tot}}\delta\langle v_z\rangle' = 0, \tag{2.37}$$

where the total viscosity

$$\chi_{\phi}^{\mathrm{tot}} = \chi_{\phi} - |\chi_{\phi}^{\mathrm{Res}}| \tag{2.38}$$

consists of both the ambient turbulent viscosity and the negative viscosity induced by the residual stress. Thus, an axial flow shear modulation is either damped or growing without oscillation, with growth rate given by

$$\gamma_q = -q_r^2\chi_{\phi}^{\mathrm{tot}} \tag{2.39}$$

where q_r is the radial wave number of the modulation. When the negative viscosity is large enough that the total viscosity becomes negative, the axial flow shear modulation is unstable, which means a small perturbation to the mean flow profile can be amplified. This is analogous to the modulational growth of zonal flow shears [DIIH05b].

However, the test flow shear cannot grow forever. The mean axial flow profile gradient is limited by the PSFI threshold Eq.(4.13). When the flow shear hits $\langle v_z\rangle'_{\mathrm{crit}}$, an additional turbulent viscosity $\chi_{\phi}^{\mathrm{PSFI}}$ driven by $\nabla\langle v_z\rangle$ is induced. Moreover, being nonlinear in the flow shear, $\chi_{\phi}^{\mathrm{PSFI}}$ is large enough to make the total viscosity positive, since

$$\chi_\phi^{\mathrm{tot}} = \chi_\phi^{\mathrm{DW}} + \chi_\phi^{\mathrm{PSFI}} \Theta\left(\langle v_z\rangle' - \langle v_z\rangle'_{\mathrm{crit}}\right) - |\chi_\phi^{\mathrm{Res}}|, \tag{2.40}$$

so that the modulational growth of the test flow shear stops. In this way, the PSFI threshold given by Eq.(4.13) sets an upper limit for the mean flow shear driven by the modulational growth, and the total viscosity is kept positive.

To summarize, a test, or seed, sheared axial flow is amplified by the negative viscosity induced by the residual stress. In particular, when the induced negative viscosity is larger than the ambient turbulent viscosity such that the total viscosity becomes negative, the test shear is then amplified to form a macroscopic profile by the modulational instability. The axial flow profile gradient is limited by the PSFI threshold. Also, the total viscosity stays positive due to the PSFI induced turbulent viscosity. Moreover, the total viscosity given by Eq.(2.40) is driven by both ∇n_0 (which drives χ_ϕ^{DW} and $-|\chi_\phi^{\mathrm{Res}}|$) and $\nabla\langle v_z\rangle$ (which drives $\chi_\phi^{\mathrm{PSFI}}$ when PSFI switches on). This makes χ_ϕ^{tot} different from familiar eddy viscosities. In particular, χ_ϕ^{tot} can give rise to the self-amplification of a test flow shear and also limit this modulational growth.

2.5 Mean Flow Structure

The turbulent plasma flow in a cylindrical chamber is similar to a turbulent pipe flow (Fig.2.2), with a point-by-point comparison listed on Table 2.3. The turbulent hydrodynamic pipe flow is driven by axial pressure drop due to pumping power, and dissipated by the turbulent viscosity driven by the background hydrodynamic turbulence. By balancing the local momentum input (ΔP) and momentum diffusion ($\langle \tilde{v}_r \tilde{v}_z\rangle \sim -\nu_T \langle v_z\rangle'$), the flow gradient is obtained as $\langle v_z\rangle' \sim -\Delta P/\nu_T$. The flow vanishes at the boundary due to the frictional force by the wall, which sets the boundary condition as no-slip. In a linear plasma device like CSDX, axial plasma flow can always be driven by the axial pressure drop ΔP_i. Therefore, the axial flow does not need

Table 2.3: Comparison and contrast between hydrodynamic pipe flow and plasma flow in a cylinder.

	Pipe flow	Plasma flow
Drive	Pressure drop ΔP	Ion pressure drop ΔP_i
Boundary condition	No slip wall	Set by neutral flows within boundary layer, located near the wall
Viscosity	ν_T	$\chi_\phi^{\mathrm{DW}}(\nabla n_0) + \chi_\phi^{\mathrm{PSFI}}(\nabla\langle v_z\rangle)\Theta(\langle v_z\rangle' - \langle v_z\rangle'_{\mathrm{crit}}) - \lvert\chi_\phi^{\mathrm{Res}}(\nabla n_0)\rvert$

a negative viscosity for generation. However, by the dynamical symmetry breaking, the axial flow gradient can be enhanced by the negative viscosity increment induced by the residual stress. Hence, an intrinsic axial flow is generated, enhancing the axial flow driven by ΔP_i. Also, for plasma flow, the total viscosity depends on both ∇n_0 and $\nabla\langle v_z\rangle$.

The boundary condition of the plasma flow is controlled by the neutral layer at the edge where the gas is partially ionized, which thus heavily involves the neutral flow dynamics. Meanwhile, the neutral momentum is coupled to the plasma momentum through ionization and recombination processes, so the boundary condition for the plasma flow is ultimately set by the neutral flows in the boundary layer. In this section, boundary conditions and their effects on the flow profile are discussed.

The axial flow profile is given by the ion momentum balance for the turbulent plasma axial flow, as shown in Fig.2.2. The ion pressure drop in the axial direction due to heating at the source end is balanced by the momentum out flux through the side wall, as determined by the Reynolds stress

$$\pi R^2 \Delta P_{\mathrm{i}} = \rho_0 \langle \tilde{v}_z \tilde{v}_r \rangle 2\pi R L.$$

Here, R and L are the radius and the length of the cylindrical plasma tube, respectively, and ρ_0 is the mean plasma density. The Reynolds stress consists of both the diffusive axial momentum flux driven by the ambient turbulent viscosity and the residual component that induces a negative viscosity increment by the dynamical symmetry breaking

$$\langle \tilde{v}_z \tilde{v}_r \rangle \cong -\left[\chi_\phi^{\mathrm{DW}} + \chi_\phi^{\mathrm{PSFI}} \Theta(\langle v_z \rangle' - \langle v_z \rangle'_{\mathrm{crit}}) - |\chi_\phi^{\mathrm{Res}}| \right] \langle v_z \rangle'.$$

As a consequence, the mean axial flow profile is

$$\langle v_z \rangle' \cong -\frac{R\Delta P_{\mathrm{i}}}{2\rho_0 L \left[\chi_\phi^{\mathrm{DW}} + \chi_\phi^{\mathrm{PSFI}} \Theta(\langle v_z \rangle' - \langle v_z \rangle'_{\mathrm{crit}}) - |\chi_\phi^{\mathrm{Res}}| \right]}. \tag{2.41}$$

The total viscosity that balances the pressure drop sets an upper limit for the flow shear through its dependence upon the mean flow profile, via the PSFI effect. When the axial flow profile steepens such that the axial flow shear exceeds $\langle v_z \rangle'_{\mathrm{crit}}$ (given by Eq.4.13) and the PSFI switches on, the resulting turbulent viscosity $\chi_\phi^{\mathrm{PSFI}}$ adds to the existing viscosity as a positive increment. The enhanced dissipation level then relaxes the flow profile, so that the mean axial flow profile gradient stays *below or at* the PSFI threshold.

Boundary conditions are important to determine the axial flow profile. By integrating Eq.(2.16), the net axial flow evolution is

$$\frac{\partial}{\partial t} \int_0^R dr \langle v_z \rangle = \int_0^R dr \frac{\Delta P_i}{\rho_0 L} - \langle \tilde{v}_r \tilde{v}_z \rangle \bigg|_R . \tag{2.42}$$

The momentum flux at the center $r = 0$ is neglected because both components of the Reynolds stress are driven by the profile gradients, which vanish at the center. Momentum transfer between ions and neutrals cancels and makes no contribution to the net flow. Eq.(2.42) shows the radial flux of axial momentum at the boundary is a sink of the net axial flow, and the axial pressure drop in the center region is a source. If there is no momentum source/sink, the flow profile should be reversed because the net momentum is conserved (Fig.2.5). However, it is not clear if flow reversal occurs in CSDX [TBC$^+$14b], and the net axial flow is always positive [CAT$^+$16]. This is due to the small momentum flux (because of the no-slip wall condition) at the boundary and

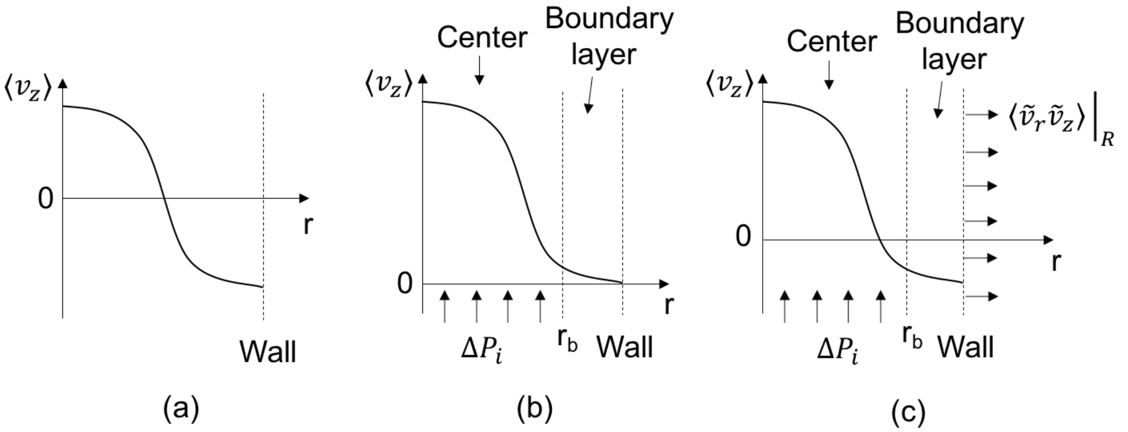

Figure 2.5: Mean flow profile for different boundary conditions. (a) No external source/sink. (b) No slip at wall, i.e. momentum flux is zero at the boundary; axial flow is driven by ion pressure drop in the axial direction. (c) With some momentum flux at the wall while axial ion pressure drop dominated, flow profile is reversed with positive net flow.

the existence of axial ion pressure drop. Axial flow is small at the boundary due to the frictional force by the wall, so $\tilde{v}_z\big|_R \cong 0$ and thus $\langle \tilde{v}_r \tilde{v}_z \rangle\big|_R \cong 0$. As a consequence, ΔP_i driven axial flow in the central region (outer region is dominated by neutral flows) raises the net flow magnitude. To calculate the axial flow profile, integrate Eq.(2.41) to get

$$\langle v_z(r) \rangle = \langle v_z(R) \rangle + \int_r^R dr \frac{R \Delta P_i}{2 \rho_0 L \chi_\phi^{\mathrm{tot}}}. \tag{2.43}$$

The plasma momentum is coupled to the neutral momentum within the boundary layer. There is no momentum loss during ionization and recombination processes, since the plasma source mostly heats electrons. Therefore, within the boundary layer near the wall ($r_b < r < R$),

$$\langle v_z \rangle \cong \langle v_{n,z} \rangle. \tag{2.44}$$

For the neutral flows within the boundary layer, the outer boundary is set by the frictional wall condition, as in a no-slip boundary condition. Assuming the width of the boundary layer is small compare to L_n, the plasma flow is approximately no-slip at the boundary, i.e.

$$\langle v_z(R)\rangle \cong 0. \tag{2.45}$$

With the no-slip boundary condition, the axial flow profile is

$$\langle v_z(r)\rangle = \int_r^R dr \frac{R\Delta P_i}{2\rho_0 L \chi_\phi^{\mathrm{tot}}}, \tag{2.46}$$

which gives rise to a positive net flow driven by the ion pressure drop in axial direction. However, if the boundary condition is not strictly no-slip–i.e. with positive momentum out-flux at the boundary (e.g. momentum loss due to ion-neutral coupling within the boundary layer)–then the flow profile can reverse near the wall region. Therefore, to obtain a physical boundary condition for the plasma flow, the details of the coupled ion and neutral dynamics need to be considered within the boundary layer. This is left to future work.

2.6 Implication for Tokamaks

The dynamical symmetry breaking mechanism does not require a particular magnetic field structure, so it may help understand intrinsic rotations with flat q profile or weak magnetic shear. Recent computational studies discover an intrinsic torque reversal at weak magnetic shear [LWD$^+$15]. Moreover, experimental results suggest that the control knob for intrinsic rotation is the magnitude of q_0, rather than magnetic shear [RPR$^+$13]. Both of them can be addressed using the dynamical symmetry breaking scheme which is independent from magnetic shear.

We propose a synergy of the conventional residual stress (linked to magnetic shear) and the residual stress induced negative viscosity by dynamical symmetry breaking. For tokamaks with normal magnetic shears, the total viscosity doesn't need to become negative to generate intrinsic flow, because the intrinsic rotation can be generated by residual stress determined by conventional models. However, the flow dissipation consists of both the ambient turbulent viscosity and the negative viscosity induced by the dynamical symmetry breaking. Then, the mean rotation profile is given by

$$\frac{d\langle v_{\parallel}\rangle}{dr} = \frac{\Pi_{r\parallel}^{\mathrm{Res}}}{\chi_{\phi}^{\mathrm{Turb}} - |\chi_{\phi}^{\mathrm{Res}}|}. \tag{2.47}$$

Thus, the negative viscosity increment enhances the rotation profile independent of the magnetic field structure. Also, the rotation profile gradient is limited by the PSFI threshold. When $\langle v_{\parallel}\rangle'$ hits the PSFI threshold, the additional turbulent viscosity driven by PSFI can raise the total viscosity and thus relaxes the rotation profile, since

$$\frac{d\langle v_{\parallel}\rangle}{dr} = \frac{\Pi_{r\parallel}^{\mathrm{Res}}}{\chi_{\phi}^{\mathrm{Turb}} + \chi_{\phi}^{\mathrm{PSFI}}\Theta(\langle v_{\parallel}\rangle' - \langle v_{\parallel}\rangle'_{\mathrm{PSFI}}) - |\chi_{\phi}^{\mathrm{Res}}|}. \tag{2.48}$$

As a result, the rotation profile gradient can be expected to stay at or below the PSFI threshold. Therefore, the dynamical symmetry breaking mechanism is applicable to the intrinsic rotation at weak magnetic shear. In addition, as the dynamical symmetry breaking uses a simple model of electron drift wave turbulence, this mechanism can be used to understand the intrinsic rotation in burning plasmas where the turbulence is the CTEM turbulence [GBH$^+$01, GSG$^+$02], and to address the effect of ECRH on toroidal rotation[SKK$^+$13, MAD$^+$11].

2.7 Conclusion and Discussion

In this paper, we propose a new dynamical symmetry breaking mechanism for the generation of intrinsic axial flows in linear devices with uniform magnetic field. Specifically, in a simple drift wave system in the presence of finite axial flow shears, a test, or seed, flow shear can be self-amplifying. The linear growth rate of the drift wave instability is set by the frequency shift from the electron drift frequency. A test axial flow shear breaks the symmetry by shifting the frequencies of some classes of modes further away from ω_* than others. As a consequence, the unbalanced turbulence spectrum couples k_θ and k_z, giving rise to a finite residual stress $\Pi_{rz}^{\mathrm{Res}} \sim \langle k_\theta k_z \rangle$. This residual stress amplifies the initial test flow shear by inducing a negative increment to the ambient turbulent viscosity. Thus, this mechanism is essentially one of negative viscosity. When the negative viscosity induced by residual stress is large enough such that the total viscosity becomes negative, the flow shear modulation is unstable and is amplified by modulational instability. When the axial flow shear exceeds $\langle v_z \rangle'_{\mathrm{crit}}$ and triggers PSFI, the additional turbulent viscosity by PSFI nonlinearly saturates the $\langle v_z \rangle'$ growth. The flow profile will then be relaxed by $\chi_\phi^{\mathrm{PSFI}}$. Hence, the axial flow shear will stay at or below $\langle v_z \rangle'_{\mathrm{crit}}$. Also, the total viscosity given by this model is driven by not only ∇n_0 but also $\nabla \langle v_z \rangle$ due to the PSFI contribution, distinguishing from the standard models of eddy viscosity.

The growth of the test flow shear is analogous to the modulational growth of zonal flow shear. Additionally, the nonlinear saturation by PSFI–a tertiary instability–is similar to the zonal flow saturation by tertiary instability. However, despite these similarities, parallel flow cannot trivially couple to zonal flow via geometry in the linear device, due to the absence of magnetic shear. The simple coupled drift wave system studied here can convert parallel compression $\nabla_\parallel \tilde{v}_\parallel$ into zonal flow [WDH12b], indicating coupling between parallel flow and zonal flow by drift wave turbulence. Thus, zonal flow may play a role in the intrinsic axial flow and the intrinsic toroidal rotation via the parallel flow-zonal flow coupling. This is left to future work.

The self-amplification of test flow shear is energy conserving. Though there is a pressure drop in the axial direction, its direct effect is weak and is amplified by dynamical symmetry breaking. Thus, the axial flow is mainly driven by the background drift wave turbulence. The process of energy transferring between fluctuation and mean axial flow can be illustrated by multiplying the flow fluctuation, mean flow, density fluctuation, mean density, and vorticity equations by $\tilde{v}_z$, $\langle v_z \rangle$, $\tilde{n}_e$, $\langle n \rangle$, ϕ, respectively and integrating them over the space:

$$\frac{\partial}{\partial t} \int \frac{\tilde{v}_z^2}{2} dV = - \int \langle \tilde{v}_r \tilde{v}_z \rangle \frac{\partial \langle v_z \rangle}{\partial r} dV - \int \tilde{v}_z \frac{\partial \tilde{p}_e}{\partial z} dV, \tag{2.49}$$

$$\frac{\partial}{\partial t}\int \frac{\langle v_z\rangle^2}{2}dV = \int \langle \tilde{v}_r\tilde{v}_z\rangle \frac{\partial\langle v_z\rangle}{\partial r}dV, \tag{2.50}$$

$$\frac{\partial}{\partial t}\int \frac{\tilde{n}_e^2}{2}dV = -\int \langle \tilde{n}_e\tilde{v}_r\rangle \frac{\partial\langle n\rangle}{\partial r}dV - \int \tilde{n}_e\frac{\partial\tilde{v}_{e,z}}{\partial z}dV, \tag{2.51}$$

$$\frac{\partial}{\partial t}\int \frac{\langle n\rangle^2}{2}dV = \int \langle \tilde{n}_e\tilde{v}_r\rangle \frac{\partial\langle n\rangle}{\partial r}dV, \tag{2.52}$$

$$\frac{\partial}{\partial t}\int \frac{(\nabla_\perp\phi)^2}{2}dV = -\int \phi\frac{\partial(\tilde{v}_z-\tilde{v}_{e,z})}{\partial z}dV, \tag{2.53}$$

where the flow drive by ion pressure drop is neglected since it is weak. By adding them up, we can obtain the energy conservation in the weakly non-adiabatic limit (i.e. $\tilde{n}_e \sim \phi$)

$$\frac{\partial}{\partial t}\int \frac{\tilde{n}_e^2+(\nabla_\perp\phi)^2+\tilde{v}_z^2+\langle v_z\rangle^2+\langle n\rangle^2}{2} = 0, \tag{2.54}$$

where $\tilde{p}_e \cong T_e\tilde{n}_e$ has been used. By keeping track of the couplings between fluctuations and mean profiles in the above system, we can see that energy is coupled in the following progression: $\langle n\rangle \to \tilde{n}_e \to \nabla_\perp\phi$ (which is $\tilde{\mathbf{v}}_{E\times B}$) $\to \tilde{v}_z \to \langle v_z\rangle$. Specifically, energy is coupled from $\tilde{v}_z$ to $\langle v_z\rangle$ via the axial Reynolds power $P_z^{\mathrm{Res}} \equiv \langle\tilde{v}_r\tilde{v}_z\rangle\partial_r\langle v_z\rangle$. Thus, it is clear that Reynolds work coupling conserves energy.

In linear device, the axial flow is driven by ion pressure drop in the axial direction and is damped by the total viscosity $\chi_\phi^{\mathrm{tot}} = \chi_\phi^{\mathrm{DW}} + \chi_\phi^{\mathrm{PSFI}}\Theta(\langle v_z\rangle' - \langle v_z\rangle'_{\mathrm{crit}}) - |\chi_\phi^{\mathrm{Res}}|$. The flow profile gradient stays below the PSFI threshold due to the nonlinear saturation by $\chi_\phi^{\mathrm{PSFI}}$. The net axial flow has a source driven by the axial ion pressure drop in the central region and a sink set by the momentum out flux at the wall. Boundary conditions for the plasma flows are determined by neutral flow dynamics within the boundary layer via ion-neutral coupling. In this paper, flow profiles (a) with no drive by ion pressure drop or momentum flux at the wall, (b) with ion pressure drop and no-slip wall boundary condition, and (c) with both ion pressure drop and momentum loss at the boundary are calculated and discussed respectively. Flow profiles strongly depend on the boundary condition. Future work on the neutral dynamics within the boundary layer will provide a physical boundary condition for the plasma flow, and will thus lead to a better understanding on the global momentum budget and axial flow structure in linear devices.

For tokamaks, a synergy of conventional models for residual stress and the negative viscosity by dynamical symmetry breaking is proposed. The dynamical symmetry breaking doesn't require complex magnetic field structure, so it is also applicable to intrinsic rotations in tokamaks. The negative viscosity reduces the total flow damping and thus enhances the intrinsic rotation profile gradient. In particular, the dynamical symmetry breaking works in flat q regimes, so is significant for controlling transport through the q profile. Also, using only a simple model of electron drift waves, this new model for residual stress can be applied to intrinsic rotation in burning plasmas with CTEM turbulence. Moreover, the dynamical symmetry breaking mechanism is also relevant to intrinsic rotation of ECH heated plasmas [SKK$^+$13]. This mechanism can enhance the effect of flow drive induced by ECH. For example, the ECH injection can induce a residual stress, Π^{Res} via conventional symmetry breaking mechanisms and the flow gradient is thus enhanced by the negative viscosity increment resulting from dynamical symmetry breaking, i.e. $\langle v_{\|}\rangle' \sim \Pi^{\mathrm{Res}}/(\chi_{\phi} - |\chi_{\phi}^{\mathrm{Res}}|)$.

The dynamical symmetry breaking mechanism can be relevant to other types of turbulence, like ITG. However, as only drift wave turbulence has been considered so far, the details of the ITG case are unknown at this stage. Its study is planned for a future publication. We conjecture that a qualitatively similar feedback mechanism may still work in ITG turbulence. This is because in ITG turbulence, the test flow shear enters the growth rate even without a frequency shift, and $\langle v_{\|}\rangle'$ enters via $k_{\theta}k_{\|}$ asymmetry. Further, for a kinetic theory of ITG instability, the basic non-adiabatic ion response is $\delta f \sim \{iL(\omega - \omega_{*,i})|e|\varphi/T_i\} f_0$, where L is a propagator. Hence, the frequency shift effect can enter here, as well. However, whether this will give a negative viscosity increment is unknown at this moment in time. We plan to address this question in a future publication, the preparation of which is ongoing.

In a similar vein, the mechanism proposed in this paper can be relevant to flow reversals during LOC-SOC transition [RCD$^+$11]. Intrinsic flow direction during the LOC-SOC transition can be set by geometrical symmetry breakers, e.g. $\langle v_E \rangle'$ and $I'(x)$. However, our mechanism enhances the flow profile gradient, via $\langle v_\parallel \rangle' \sim \Pi^{\text{Res}}/(\chi_\phi - |\chi_\phi^{\text{Res}}|)$. In LOC state, $\langle v_\parallel \rangle'$ is enhanced by $-|\chi_\phi^{\text{Res}}|$ as a result of dynamical symmetry breaking. In SOC state, however, it is unclear about the effects on $\langle v_\parallel \rangle'$ by other types of turbulence, and this will be left for a future publication, as commented above.

The dynamical symmetry breaking is fundamentally different from the usual eddy tilting. In the dynamical symmetry breaking model, flow shear directly affects the linear growth rate by selecting some modes which grow faster, resulting in a spectral imbalance. Eddy tilting by $\langle v_\theta \rangle'$ in (r,θ) plane enters the correlator $\langle \tilde{v}_r \tilde{v}_\theta \rangle \sim \langle k_\theta k_r \rangle \sim -\langle k_\theta^2 \rangle \langle v_\theta \rangle' \tau_c$, resulting in an unambiguous Reynolds work, and does not enter directly via stability. But in (r,z) plane, eddy tilting does not work, because $\partial_t k_z = -\partial_z(\omega + k_z \langle v_z \rangle) = 0$. In our case, the $\langle k_\theta k_r \rangle$ correlator couples differently to the growth rate, for different $\langle k_\theta k_r \rangle$. Thus, our mechanism is fundamentally different from eddy tilting.

Chapter 2 is a reprint of the material as it appears in J. C. Li, P. H. Diamond, X. Q. Xu, and G. R. Tynan, “Dynamics of intrinsic axial flows in unsheared, uniform magnetic fields”, *Physics of Plasmas* **23**, 052311 (2016), American Institute of Physics. The dissertation author was the primary investigator and author of this article.

Chapter 3

Negative Viscosity from Negative Compressibility and Axial Flow Shear Stiffness in a Straight Magnetic Field

3.1 Introduction

Strong toroidal rotation and weak magnetic shear are desirable for enhanced confinement in tokamaks. External drives for rotation, e.g. neutral beams, will be insufficient to assure MHD stability [**?**] in future fusion devices, such as ITER. Thus, intrinsic rotation is of interest. Weak or reversed magnetic shear has long been known to enhance microstability and confinement. Studies on enhanced reversed shear [SBB$^+$97], negative central shear [RTB$^+$96], weakly negative shear [YHN$^+$15], etc. reveal this trend. For example, de-stiffened states, with enhanced confinement, were observed in the weak shear regime in JET [MAC$^+$11a]. Therefore, intrinsic rotation at weak magnetic shear is of particular interest. Intrinsic rotation can be generated by background turbulence. Thus, in tokamaks, intrinsic rotation usually tracks the driving gradient of turbulence [RHD$^+$11a]. This also poses the question of how the flow gradient (∇V_ϕ) interacts with, and scales with, the driving gradient of turbulence (i.e. edge ion temperature gradient in the case of Ref.[RHD$^+$11a]).

The controlled shear de-correlation experiment (CSDX) is a cylindrical linear device with uniform axial magnetic fields and turbulence driven intrinsic parallel flows. It offers a well-diagnosed venue for the study of intrinsic flows in the shear-free regime [TBC$^+$14b]. Since most mechanisms for intrinsic parallel flow generation rely on magnetic shear [DKG$^+$13a], a new dynamical symmetry breaking mechanism was proposed to account for axial flow generation in CSDX. This mechanism does not require a specific magnetic field configuration, so it can work in regimes with and without shear. Symmetry breaking is usually required to set a preferred direction for the flow, i.e. a finite $\langle k_\parallel \rangle$. The residual stress is determined by the correlator $\langle k_\theta k_\parallel \rangle \equiv \sum_k k_\theta k_\parallel |\phi_k|^2$. Hence, asymmetry-specifically, handedness-in the turbulent spectrum ($|\phi_k|^2$) is required to obtain a nonzero residual stress. In CSDX, where the turbulence is usually a population of electron drift waves (EDWs), the growth/drive rate is determined by the drift mode frequency shift relative to the electron drift frequency, i.e. $\gamma_k \sim \omega_{*e} - \omega_k$ [LDXT16a]. A test flow shear ($\delta V_\parallel'$) changes the frequency shift, setting modes with $k_\parallel k_\theta \delta V_\parallel' > 0$ to grow faster than those with $k_\parallel k_\theta \delta V_\parallel' < 0$. Therefore, a spectral imbalance in $k_\parallel k_\theta$ space develops, which sets a finite residual stress $\delta\Pi_{r\parallel}^{Res}$. The resulting residual stress drives an intrinsic flow, and so reinforces the test flow shear. This self-amplification of $\delta V_\parallel'$ is a negative viscosity phenomenon. The residual stress induces a negative viscosity increment, i.e. $\delta\Pi_{r\parallel}^{Res} \sim |\chi_\phi^{Res}|\delta V_\parallel'$. The basic scenario resembles that familiar from the theory of zonal flow generation [DIIH05b]. The flow shear modulation ($\delta V_\parallel'$) becomes unstable when the total viscosity $\chi_\phi^{Tot} = \chi_\phi - |\chi_\phi^{Res}|$ turns negative. Therefore, $\delta V_\parallel'$ can be self-reinforced via modulational instability. When the flow profile gradient steepens enough, so that the parallel shear flow instability (PSFI) is turned on, the mean flow gradient ($\nabla V_\parallel$) saturates at the PSFI linear threshold and the total viscosity stays positive, due to the contribution induced by PSFI, i.e. $\chi_\phi^{Tot} = \chi_\phi^{DW} + \chi_\phi^{PSFI} - |\chi_\phi^{Res}|$. In CSDX, the PSFI linear threshold grows as $|V_\parallel'|_{\text{crit}}/|k_\parallel c_s| \sim (k_\parallel L_n)^{-2}$ [LDXT16a, KII15], where

$L_n \equiv -(\partial_r \ln n_0)^{-1}$. Therefore, the flow gradient tracks the turbulence driving gradient (i.e. ∇n_0) as $\nabla V_\parallel / |k_\parallel c_s| \sim |V'_\parallel|_{\text{crit}} / |k_\parallel c_s| \sim (k_\parallel L_n)^{-2}$. This scaling motivates us to wonder if there is a generalized form of the Rice-type scaling [RICd$^+$07a, RHD$^+$11a].

CSDX has straight magnetic fields, and thus is an important limiting case for understanding flow generation at zero shear. While existing models of axial flow generation in CSDX are based on EDW turbulence, fluctuations propagating in the ion drift direction are observed [CAT$^+$16]. Such ion features appear in the central region of the cylindrical plasma in CSDX, where the density profile is flat. In addition, turbulence driven by the ion temperature gradient (ITG) controls momentum transport in tokamaks operated in enhanced confinement states, e.g. states with an internal transport barrier (ITB). Also, intrinsic rotation tracks the edge temperature gradient [RHD$^+$11a]. These trends beg the questions:

1. How does negative compressibility turbulence, e.g. ITG turbulence, affect momentum transport at zero magnetic shear? Particularly, what happens in flat density limit?
2. How does $\nabla V_\parallel$ saturate in ITG turbulence?
3. With tokamaks in mind, how does this new mechanism interact with conventional mechanisms which exploit magnetic shear? What is the interplay of $\nabla V_\parallel$ and ∇T_{i0}?

It has long been known that a finite parallel shear flow (PSF) $\nabla V_\parallel$ can enhance ITG turbulence in sheared magnetic fields [MD88]. However, the detailed question of how the mean flow gradient, $\nabla V_\parallel$, and its perturbation, $\delta V'_\parallel$, affect flow generation and saturation in ITG turbulence in a straight field remains unanswered.

In this paper, we study the effects of ITG turbulence on momentum transport in a straight magnetic field. In the regime well above the ITG stability boundary, a perturbation to the flow profile, $\delta V'_\parallel$, can reduce the turbulent viscosity. $\delta V'_\parallel$ breaks the symmetry by allowing modes with $k_\theta k_\parallel \delta V'_\parallel > 0$ to grow faster than modes with $k_\theta k_\parallel \delta V'_\parallel < 0$. This results in a spectral imbalance in $k_\theta k_\parallel$ space. The residual stress set by this spectral imbalance drives an up-gradient momentum

Table 3.1: Compare $\delta V_{\parallel}'$ induced symmetry breaking in ITG turbulence and electron drift wave turbulence.

	ITG Turbulence	Electron Drift Wave
Direction of correlator	$\langle k_\theta k_\parallel \rangle \delta V_\parallel' > 0$	$\langle k_\theta k_\parallel \rangle \delta V_\parallel' > 0$
Viscosity increment by $\delta\Pi_{r\parallel}^{Res}$	$\chi_\phi^{Res} < 0$	$\chi_\phi^{Res} < 0$
Total viscosity	$\chi_\phi^{Tot} > 0$	χ_ϕ^{Tot} can be negative
Modulational instability	Not exist	Can exist

flux which induces a negative viscosity increment, i.e. $\delta\Pi_{r\parallel}^{Res} \sim |\chi_\phi^{Res}|\delta V_\parallel'$ with $\chi_\phi^{Res} < 0$. Thus, the *total* viscosity is reduced, since $\chi_\phi^{Tot} = \chi_\phi - |\chi_\phi^{Res}|$. The mean flow gradient driven by ITG turbulence is consequently steepened, since $\nabla V_\parallel \sim \Pi_{r\parallel}^{Res}/\chi_\phi^{Tot}$.

However, unlike the case of dynamical symmetry breaking in EDW turbulence, we show that symmetry breaking induced by $\delta V_\parallel'$ in ITG turbulence alone *cannot* amplify the seed flow shear ($\delta V_\parallel'$). Therefore, ITG turbulence *cannot* drive intrinsic flows in straight magnetic fields. In ITG turbulence, the total momentum diffusivity χ_ϕ^{Tot} remains positive, because $|\chi_\phi^{Res}| = \frac{1}{3}\chi_\phi$. The growth rate of a flow shear modulation is $\gamma_q = -\chi_\phi^{Tot} q_r^2$, where q_r is the radial mode number of the modulation. A positive definite χ_ϕ^{Tot} does not induce modulational instability. This differs from the case of EDW turbulence. Table 3.3 shows the comparison between symmetry breaking in ITG and EDW turbulence.

The axial flow in CSDX can be driven by various external sources. The axial ion pressure drop, induced by the location of the heating source on one end of the cylindrical plasma, can drive an axial flow. Biasing the end plate can also accelerate axial ion flows by axial electric fields.

The flow gradient produced by external or intrinsic drive ultimately must saturate due to PSFI-induced relaxation. $\nabla V_\parallel$ can be enhanced by external drives, e.g. the axial ion pressure drop and end plate biasing. When $\nabla V_\parallel$ is stronger than the ion temperature profile gradient (∇T_{i0}), PSFI drive controls the turbulence. Here, the relative strength between ∇T_{i0} and $\nabla V_\parallel$ is measured by the relative length scale $L_T/L_V \equiv \partial_r \ln V_\parallel / \partial_r \ln T_{i0}$. In turbulence controlled by PSFI, both the residual stress and turbulent viscosity depend nonlinearly on $\nabla V_{\parallel}$. As a result, the flow gradient saturates *above* the linear threshold of PSFI and the saturated $\nabla V_{\parallel}$ grows with ∇T_{i0}. This implies a "stiff" $\nabla V_{\parallel}$ profile. An aim of this paper is to calculate the scaling $\nabla V_{\parallel}/k_{\parallel}c_s \sim (k_{\parallel}L_T)^{-\alpha}$ of this stiffness.

The scaling of the $\nabla V_{\parallel}$ profile stiffness reveals the final state of the nonlinear interaction between $\nabla V_{\parallel}$ and ∇T_{i0}. It should be noted that PSFI co-exists with ITG turbulence. Their relative strength depends on L_T/L_V. Because $\nabla V_{\parallel}$ and ∇T_{i0} are coupled nonlinearly, they don't simply add up. However, PSFI can be distinguished from ITG instability (at least in simulation) by comparing their mode phases. The mode phase is defined as

$$\theta_k \equiv \begin{cases} \tan^{-1}(\gamma_k/\omega_k), & \omega_k > 0; \\ \pi + \tan^{-1}(\gamma_k/\omega_k), & \omega_k < 0. \end{cases}$$

Here, γ_k and ω_k are the growth rate and real frequency of the mode. PSFI has zero frequency, which means $\theta_k^{PSFI} = \pi/2$, while the ITG mode phase is usually $\theta_k^{ITG} = 2\pi/3$. The theoretical concept of mode phase is related to the cross phase between flow fluctuations, $\tilde{v}_{\parallel}$ and $\tilde{v}_r$, and thus can be measured in experiments, at least in principle. Also, since mode phase affects Reynolds stress $\langle \tilde{v}_{\parallel}\tilde{v}_r \rangle$, intrinsic flow profiles are sensitive to the mode phase.

Comparison between symmetry breaking in EDW and ITG turbulence drives us to wonder if flow reversal is possible in CSDX by a change in turbulence population from EDW to ITG? More generally, can the idea that mode change leads to flow reversals [RCD$^+$11] be tested by basic experiments? The flow profile in CSDX is determined by the ratio between the axial ion pressure drop ΔP_i and the total turbulent viscosity [LDXT16a], i.e. $V_{\parallel} \sim \int_r^a dr \Delta P_i/\chi_{\phi}^{Tot}$ where a is the plasma radius in CSDX. In EDW, though χ_{ϕ}^{Tot} can turn negative at least transiently, it is finally forced positive by PSFI saturation. In ITG turbulence, χ_{ϕ}^{Tot} is positive definite, since $|\chi_{\phi}^{Res}| = \frac{1}{3}\chi_{\phi}$. Therefore, there would be no argument for flow reversal in the final state, even though fluctuation or reversal may occur as a transient. Also, one can argue that flow reversal, even if it exists in CSDX, does not track the change in turbulence from EDW to ITG.

We neglect the momentum pinch effect in this work. In addition to the diffusive and residual components, the parallel Reynolds stress can have a momentum pinch term that is proportional to the flow magnitude. Since the momentum pinch is usually due to toroidal effect in tokamaks [HDGR07, PAB$^+$11, ACC$^+$12], it is neglected in this work, where we study linear devices that have straight and uniform magnetic fields. In general, the momentum pinch is of the turbulent equipartition variety, and so $|V_{pinch}|/|\chi_\phi| \sim 1/R_0$, where R_0 is the major radius of the tokamak. This is explained as a toroidal effect. It is possible to also have L_n scalings, i.e. $|V_{pinch}|/|\chi_\phi| \sim 1/L_n$, in certain parameter regimes. However, since this analysis does not treat self-consistent evolution of density profiles, we decided to omit a discussion of this rather sensitive, detailed effect.

The rest of this paper is organized as follows: Sec.5.2 introduces the fluid model of the PSF–ITG system in a straight magnetic field. Sec.3.3 discusses the three regimes that we consider in this work. Sec.3.4 summarizes the structure of results. Sec.3.5 presents results on mode phase, symmetry breaking, and flow profile in each regime. Finally, Sec.6.4 summarizes and discusses the results.

3.2 Fluid Model for PSF–ITG System

We consider a system where the ion temperature gradient (∇T_{i0}) is coupled to the flow gradient ($\nabla V_\parallel$), i.e. a coupled PSF–ITG system of potential vorticity, $\tilde{q} = (1 - \nabla_\perp^2)\phi$, parallel flow, $v_\parallel = \tilde{v}_\parallel + V_\parallel$, and ion pressure, $p_i = \tilde{p}_i + P_0$, with zero magnetic shear in cylindrical geometry:

$$\frac{d}{dt}(1-\nabla_\perp^2)\phi + \mathbf{v}_E \cdot \frac{\nabla n_0}{n_0} + \nabla_\parallel \tilde{v}_\parallel = 0, \tag{3.1}$$

$$\frac{d\tilde{v}_\parallel}{dt} + \mathbf{v}_E \cdot \nabla V_\parallel = -\nabla_\parallel \phi - \nabla_\parallel \tilde{p}_i, \tag{3.2}$$

$$\frac{d\tilde{p}_i}{dt} + \frac{1}{\tau}\mathbf{v}_E \cdot \frac{\nabla P_0}{P_0} + \frac{\Gamma}{\tau}\nabla_{\|}\tilde{v}_{\|} + \nabla_{\|}Q_{\|} = 0. \tag{3.3}$$

Here, lengths are normalized by $\rho_s \equiv \sqrt{m_i T_{e0}}/(eB_0)$, time is normalized by the ion cyclotron frequency ω_{ci}^{-1}, velocities are normalized by the ion sound speed $c_s \equiv \sqrt{T_{e0}/m_i}$, and the electrostatic potential is normalized as $\phi \equiv e\tilde{\varphi}/T_{e0}$. The convective derivative is defined as $d/dt \equiv \partial/\partial t + \mathbf{v}_E \cdot \nabla$, where $\mathbf{v}_E = \mathbf{B}_0 \times \nabla\phi/B_0$ is the $E \times B$ velocity. The kinetic effect of Landau damping is retained by including the parallel heat flux, with Hammett-Perkins closure $Q_{\|,k} = -\chi_{\|} n_0 i k_{\|} \tilde{T}_{i,k}$. Here, the (collisionless) parallel heat conductivity is $\chi_{\|} = 2\sqrt{2} v_{Thi}/(\sqrt{\pi}|k_{\|}|)$, and v_{Thi} is the ion thermal speed. The ratio of specific heats is $\Gamma = 3$ in this model. The electron response is adiabatic, corresponding to Boltzmann electrons, i.e. $\tilde{n} = \phi$. Hence, $\tilde{p}_i = \tilde{T}_i + \phi/\tau$, with the temperature ratio defined as $\tau \equiv T_{e0}/T_{i0}$. Since the ion features exist in the center of CSDX where density profile is flat, we take $\nabla n_0 = 0$ throughout. Thus, the mean pressure gradient consists of only temperature gradient, i.e. $\nabla P_0 = \nabla T_{i0}$. The linear dispersion relation for the PSF–ITG system is

$$A\Omega^3 - (C_0 - V')\Omega - D + \frac{i|k_{\|}|\chi_{\|}}{c_s}\left(A\Omega^2 + V' - \frac{1+\tau}{\tau}\right) = 0, \tag{3.4}$$

with $\Omega \equiv \omega/|k_{\|}c_s|$, $V' \equiv k_\theta k_{\|} \rho_s c_s V_{\|}'/k_{\|}^2 c_s^2$, $A \equiv 1 + k_\perp^2 \rho_s^2$, $C_0 \equiv 1 + (1 + k_\perp^2 \rho_s^2)\Gamma/\tau$, $D \equiv \omega_T/\tau|k_{\|}c_s|$. ω_T is defined as $\omega_T \equiv -k_\theta \rho_s c_s \partial_r \ln T_{i0}$. In a linear device, such as CSDX, $\tau > 1$, so $|k_{\|}|\chi_{\|}/c_s \sim 1/\sqrt{\tau} < 1$. Thus, terms involving $i|k_{\|}|\chi_{\|}/c_s$ will be neglected.

∇T_{i0} and $\nabla V_{\|}$ are coupled nonlinearly, because either ∇T_{i0} or $\nabla V_{\|}$ can drive instability, by forcing

$$\Delta \equiv \left(\frac{D}{2A}\right)^2 - \left(\frac{C_0 - V'}{3A}\right)^3 > 0. \tag{3.5}$$

The growing mode has growth rate and frequency:

$$\gamma_k = \frac{\sqrt{3}}{2}|k_{\|}c_s|\left(\sqrt[3]{\frac{D}{2A} + \sqrt{\Delta}} - \sqrt[3]{\frac{D}{2A} - \sqrt{\Delta}}\right), \tag{3.6}$$

$$\omega_k = -\frac{1}{2}|k_\parallel c_s| \left(\sqrt[3]{\frac{D}{2A} + \sqrt{\Delta}} + \sqrt[3]{\frac{D}{2A} - \sqrt{\Delta}} \right). \tag{3.7}$$

In the following sections, we will see that in presence of a shear flow $V'_\parallel$, modes with $k_\theta k_\parallel V'_\parallel > 0$ grow faster than others. Therefore, we take $V' \equiv k_\theta k_\parallel V'_\parallel / k_\parallel^2 c_s^2 > 0$.

The underlying instability drive is negative compressibility. Both ITG instability and PSFI are negative compressibility phenomena. Negative compressibility means an increase in density (compression in volume) leads to decrease in pressure. For the system studied here, the relation between the pressure perturbation and density perturbation is

$$\tilde{p}_i \sim \left(\frac{\Gamma}{\tau} \frac{k_\parallel^2 c_s^2}{\omega_k^2} - \frac{\Gamma}{\tau} \frac{k_\theta k_\parallel \rho_s c_s V'_\parallel}{\omega_k^2} - \frac{\omega_T}{\tau|\omega_k|} \right) \tilde{n}.$$

Here, we have used the adiabatic electron response $\tilde{n} \sim \phi_k$. The compressibility becomes negative when either of ITG instability or PSFI is above threshold. Note, ∇T_{i0} and $\nabla V_\parallel$ can act in synergy to turn the compressibility negative, driving the system unstable.

Though coupled nonlinearly, PSFI and ITG instability can be distinguished by different mode phases. PSFI is a purely growing mode, so $\theta_k = \pi/2$. This is because (for $\nabla T_{i0} \to 0$), the dispersion relation becomes

$$A\Omega^2 - (C_0 - V') = 0, \tag{3.8}$$

which gives a purely growing branch when $V' > V'_{\text{crit}} \equiv C_0$, with growth rate $\gamma_k = |k_\parallel c_s| \sqrt{(V' - C_0)/A}$. In contrast, ITG instability has a negative real frequency whose magnitude is comparable to the growth rate. If ∇T_{i0} (the term D) dominates the dispersion relation Eq.4.10, then the resulting ITG mode has complex frequency $\omega \sim \exp(i2\pi/3)[|\omega_T|k_\parallel^2 c_s^2/(\tau A)]^{1/3}$, with mode phase $\theta_k \cong 2\pi/3$.

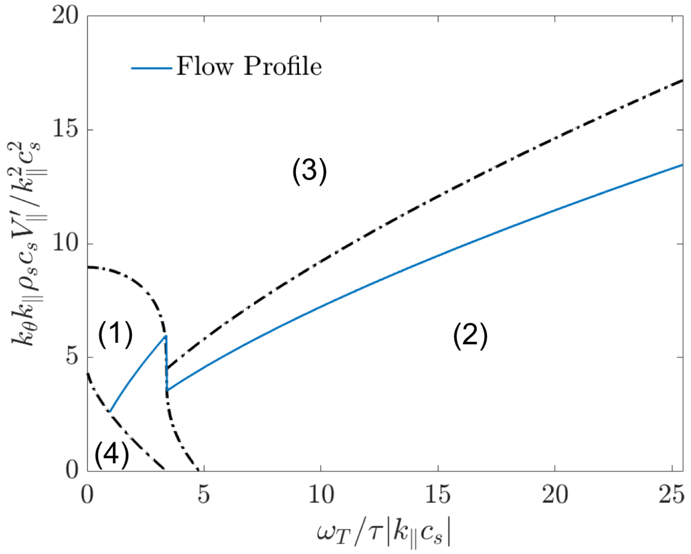

Figure 3.1: Regime defined by instability types and flow profile driven by the PSF–ITG turbulence. The regimes are (1) marginal regime; (2) ITG regime; (3) PSFI regime; and (4) stable regime. Parameters used for this plot are $k_\theta \rho_s = 0.4$ and the ratio of specific heats $\Gamma = 3$.

3.3 Instability Regimes

The nonlinear coupling between $\nabla V_\|$ and ∇T_{i0} significantly increases the level of complexity of calculating the residual stress and the flow profile. Therefore, we classify the PSF–ITG system into three regimes (Fig.3.1), determined by length scales $L_V^{-1} \equiv -\partial_r \ln V_\|$ and $L_T^{-1} \equiv -\partial_r \ln T_{i0}$:

1) The marginal regime is defined by $\Delta \gtrsim 0$, where PSFI and ITG instability co-exist, and both of them are weakly unstable. Thus, $\nabla V_\|$ and ∇T_{i0} are nonlinearly coupled in this regime.

2) The ITG regime is where the system is well above the marginal state and ∇T_{i0} contributes more than $\nabla V_\|$ to the magnitude of Δ, i.e. $(D/2A)^2 > (V'/3A)^3$ which leads to

$$\frac{L_T^{2/3}}{|k_\||^{1/3} L_V} < \frac{c_s}{V_\|} \frac{3}{2^{2/3}} \frac{A^{1/3}}{(k_\theta \rho_s)^{1/3} \tau^{2/3}}. \tag{3.9}$$

We show in Sec.3.5 that, in this regime, though a test flow shear $\delta V_{\|}'$ induces a negative viscosity contribution, the *total viscosity* is *positive definite*. Consequently, there is no intrinsic flow driven by ITG turbulence in a straight field. This is quite different from the case of EDW turbulence.

3) The PSFI regime is also well above the marginal state, but where $\nabla V_{\|}$ contributes more than ∇T_{i0} to instability drive, i.e.

$$\frac{L_T^{2/3}}{|k_{\|}|^{1/3} L_V} > \frac{c_s}{V_{\|}} \frac{3}{2^{2/3}} \frac{A^{1/3}}{(k_\theta \rho_s)^{1/3} \tau^{2/3}}. \tag{3.10}$$

This gives the regime boundary above which PSFI controls the turbulence:

$$|V_{\|}'|_{\text{reg}} = \frac{3}{2^{2/3}} A^{1/3} \left(\frac{|\omega_T|}{\tau |k_{\|} c_s|} \right)^{2/3} \frac{|k_{\|}| c_s}{k_\theta \rho_s}. \tag{3.11}$$

External flow drives can enhance the flow profile gradient. Hence, $\nabla V_{\|}$ can exceed the PSFI regime boundary ($|V_{\|}'|_{\text{reg}}$). PSFI is nonlinear in $\nabla V_{\|}$. Consequently, the turbulent viscosity is nonlinear in $\nabla V_{\|}$, and so $\nabla V_{\|}$ saturates at $|V_{\|}'|_{\text{reg}}$ which is *above the linear threshold of PSFI.* Thus, there is a clear distinction between the threshold $\nabla V_{\|}$ profile and the saturated-or "stiff"-$\nabla V_{\|}$ profile.

3.4 Structure of Results

In this section, we summarize the key aspects of results. We consider a) symmetry breaking by $\delta V_{\|}'$, b) mode phase, and c) flow profile in each of the three regimes. A test flow shear $\delta V_{\|}'$ can break the symmetry and induce a incremental viscosity via the residual stress, i.e. $\delta \Pi_{r\|}^{Res} = -\chi_\phi^{Res} \delta V_{\|}'$. The sign of χ_ϕ^{Res} is determined by the mode phase. Thus, χ_ϕ^{Res} has different signs in PSFI and ITG turbulence. Finally, we need to calculate the flow profile, in order to

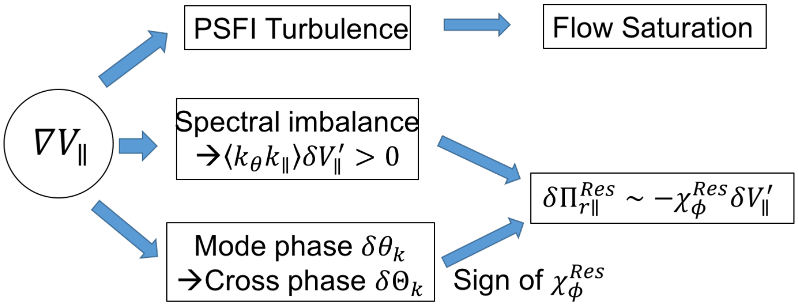

Figure 3.2: Diagram of the three roles played by $\nabla V_\parallel$ in the PSF–ITG system.

explore possibilities about flow saturation in the context of negative compressibility turbulence, i.e. ITG and PSFI turbulence. In the rest of the section, we discuss these three aspects in detail.

3.4.1 Symmetry Breaking by $\delta V_\parallel'$

A perturbation to the flow profile, $\delta V_\parallel'$, breaks the $k_\parallel \to -k_\parallel$ symmetry. $\langle k_\theta k_\parallel\rangle$ is linked to $\delta V_\parallel'$ via the acoustic coupling, $\nabla_\parallel \tilde{v}_\parallel$. In Sec.3.5, we will show that modes with $k_\theta k_\parallel \delta V_\parallel' > 0$ grow faster than those without. This sets a spectral imbalance in $k_\theta k_\parallel$ space. Further, the finite residual stress set by this imbalance is found to be a Fickian momentum flux, i.e. $\delta\Pi_{r\parallel}^{Res} \sim -\chi_\phi^{Res}\nabla V_\parallel$. The viscosity increment induced by residual stress then adds to the total viscosity, so that $\chi_\phi^{Tot} = \chi_\phi + \chi_\phi^{Res}$. Table 3.2 compares symmetry breaking in the three regimes.

3.4.2 Mode Phase

The sign of residual stress is determined by mode phase. Here, mode phase (θ_k) is defined as the phase of the complex mode frequency, i.e. $\omega = \omega_k + i\gamma_k \equiv e^{i\theta_k}\sqrt{\omega_k^2+\gamma_k^2}$. Linearizing the response of $\tilde{v}_{\parallel,k}$, we can obtain the quasilinear Reynolds stress [GDHS07a, GDH$^+$10a]

$$\langle \tilde{v}_\parallel \tilde{v}_r\rangle = -\chi_\phi V_\parallel' + \Pi_{r\parallel}^{Res}, \tag{3.12}$$

with the turbulent viscosity:

$$\chi_\phi \approx \Re \sum_k \frac{i}{\omega} k_\theta^2 \rho_s^2 |\phi_k|^2, \tag{3.13}$$

and residual stress:

$$\Pi_{r\|}^{Res} \approx \Re \sum_k \frac{i}{\omega^2} \frac{\omega_T}{\tau} k_\theta k_\| \rho_s c_s |\phi_k|^2, \tag{3.14}$$

where $\omega_T \equiv -k_\theta \rho_s c_s \partial_r T_{i0}/T_{i0}$. Here, $\omega \equiv \omega_k + i\gamma_k = |\omega| e^{i\theta_k}$ is the complex mode frequency with mode number k, and so $i/\omega \sim e^{i(\pi/2-\theta_k)}$ and $i/\omega^2 \sim e^{i(\pi/2-2\theta_k)}$. Therefore, the *sign* of the residual stress is determined by θ_k, as $\Pi_{r\|}^{Res} \sim \langle k_\theta k_\| \rangle \Re(i/\omega^2) \sim \langle k_\theta k_\| \rangle \cos(\pi/2 - 2\theta_k)$.

Mode phase also determines the sign of χ_ϕ^{Res}, i.e. the viscosity contribution induced by residual stress. In presence of a test flow shear, $\delta V_\|'$, the residual stress induces a momentum flux, $\delta\Pi_{r,\|}^{Res} = -\chi_\phi^{Res} \delta V_\|'$. The sign of χ_ϕ^{Res} is determined by both the mode phase and its change due to $\delta V_\|'$. The residual stress' response to the test flow shear is

$$\delta\Pi_{r,\|}^{Res} \sim -2 \sum_k \cos(\frac{\pi}{2} + \delta\theta_k - 3\theta_k) \frac{|\delta\omega|}{|\omega|^3} \frac{\omega_T}{\tau} k_\theta k_\| |\phi_k|^2, \tag{3.15}$$

where $\delta\theta_k$ is the phase of perturbed complex frequency due to $\delta V_\|'$, i.e. $\delta\omega \equiv |\delta\omega| \exp(i\delta\theta_k)$. Since $|\delta\omega| \sim k_\theta k_\| \delta V_\|'$, the sign of the residual stress-induced viscosity contribution is determined by

$$\chi_\phi^{Res} \sim \cos\left(\frac{\pi}{2} + \delta\theta_k - 3\theta_k\right). \tag{3.16}$$

ITG instability and PSFI have different mode phases, leading to different signs of χ_ϕ^{Res}. As a result, $\delta V_\|'$ has different effects on momentum transport in ITG and PSFI turbulence.

3.4.3 Flow Profile

Though pure ITG turbulence cannot drive intrinsic flows in straight field, ∇T_{i0} affects momentum transport, and thus can regulate the flow gradient. In CSDX, the axial flow can be driven by the axial ion pressure drop. In order to uncover the ITG effect on the flow, we

Table 3.2: Characteristics of the three PSF–ITG instability regimes. Mode phase is defined as the phase of complex mode frequency, i.e. $\omega \equiv \omega_k + i\gamma_k \equiv |\omega| e^{i\theta_k}$. $\delta\theta_k$ is the phase of perturbed complex frequency, $\delta\omega$, due to $\delta V_\parallel'$. χ_ϕ^{Res} is the incremental viscosity induced by $\delta V_\parallel'$. Since PSFI is driven by $\nabla V_\parallel$ nonlinearly, $\delta V_\parallel'$ effect is nonlinear, so we do not consider its linear effects, i.e. $\delta\theta_k$ and χ_ϕ^{Res}.

	Marginal Regime	ITG Regime	PSFI Regime
Primary Turbulence Drive	∇T_{i0} and $\nabla V_\parallel$	∇T_{i0}	$\nabla V_\parallel$
$\delta V_\parallel'$ Induced Spectral Imbalance	$\langle k_\theta k_\parallel \rangle \delta V_\parallel' > 0$	$\langle k_\theta k_\parallel \rangle \delta V_\parallel' > 0$	$\langle k_\theta k_\parallel \rangle \delta V_\parallel' > 0$
Mode Phase θ_k	$\lesssim \pi$	$2\pi/3$	$\gtrsim \pi/2$
Perturbed Mode Phase $\delta\theta_k$	$\pi/2$	$\pi/3$	NA
Sign of χ_ϕ^{Res}	$\chi_\phi^{Res} > 0$	$\chi_\phi^{Res} < 0$	NA

ignore the external sources in the following analysis. Consequently, the flow gradient within the center region of CSDX can be obtained from $\nabla \cdot \Pi = 0$, where Π is the total momentum flux. Considering only the parallel Reynolds stress, the flow profile gradient can be calculated from

$$\partial_r \langle \tilde{v}_r \tilde{v}_\parallel \rangle = \partial_r \left(\Pi_{r\parallel}^{Res} - \chi_\phi \nabla V_\parallel \right) = 0. \tag{3.17}$$

The edge is accounted by boundary conditions for the flow. The flow profile depends heavily on the boundary condition [LDXT16a, AGG$^+$13]. The boundary layer in CSDX is controlled by coupling between ions and neutral particles. Assuming the radial expansion of the boundary layer is negligible compared to the plasma radius, we adopt a no-slip boundary condition for $V_\parallel$. As a result, the flow profile is $V_\parallel(r) = -\int_r^a dr \nabla V_\parallel$, where a is the radius of plasma.

3.5 Results

In this section, we present results on mode phase, $\delta V_\parallel'$ induced symmetry breaking, and flow profile, for each of the three regimes.

3.5.1 Marginal Regime

When the PSF–ITG system is weakly unstable, i.e. $\Delta \gtrsim 0$, PSFI and ITG turbulence coexist. In this regime, $\nabla V_{\parallel}$ and ∇T_{i0} are coupled nonlinearly, and a perturbation to the mean flow profile raises the PSFI level and thus enhances the flow dissipation.

We can obtain the linear thresholds for ITG and PSFI turbulence. The PSF–ITG system can be viewed as an ITG system in presence of $\nabla V_{\parallel}$. From the criterion Eq.3.5, ∇T_{i0} can drive instability with a threshold depending on $\nabla V_{\parallel}$

$$\omega_{T,\mathrm{crit}}^2(\nabla V_{\parallel}) = \frac{4\tau^2 k_{\parallel}^2 c_s^2 (C_0 - V')^3}{27A}. \tag{3.18}$$

In the marginal state, i.e. $\omega_T^2 \gtrsim \omega_{T,\mathrm{crit}}^2$, the growth rate and real frequency are

$$\gamma_k \cong \frac{\sqrt{3}}{3} \frac{|k_{\parallel} c_s|^{2/3}}{(2A\tau)^{1/3}} \frac{\sqrt{\omega_T^2 - \omega_{T,\mathrm{crit}}^2}}{|\omega_T|^{2/3}}, \tag{3.19}$$

$$\omega_k \cong -\frac{|k_{\parallel} c_s|^{2/3} |\omega_T|^{1/3}}{(2A\tau)^{1/3}}. \tag{3.20}$$

Meanwhile, the PSF–ITG system can also be viewed as a PSFI system modified by ∇T_{i0}. From the criterion Eq.3.5, the PSFI threshold can be obtained, and is

$$|V_{\parallel}'|_{\mathrm{crit}} = \frac{|k_{\parallel} c_s|}{k_{\theta} \rho_s} \left[C_0 - 3A^{1/3} \left(\frac{|\omega_T|}{2\tau |k_{\parallel} c_s|} \right)^{2/3} \right]. \tag{3.21}$$

The growth rate, $\gamma_k \sim \sqrt{|V_{\parallel}'| - |V_{\parallel}'|_{\mathrm{crit}}}$ depends *nonlinearly* on $\nabla V_{\parallel}$. ∇T_{i0} enhances PSFI by lowering the PSFI threshold. Therefore, in the marginal regime, PSFI and ITG instability coexist, and one can view this weakly unstable turbulence in two equivalent ways: (1) ITG turbulence modified by $\nabla V_{\parallel}$ and (2) PSFI turbulence modified by ∇T_{i0}.

The residual stress and turbulent viscosity are

$$\Pi_{r\parallel}^{Res} \cong -\frac{2\sqrt{3}}{3}\sum_k \frac{(2A)^{2/3}}{\tau^{1/3}|k_\parallel c_s|^{4/3}} \frac{\sqrt{\omega_T^2-\omega_{T,\mathrm{crit}}^2}}{|\omega_T|^{2/3}} k_\theta k_\parallel \rho_s c_s |\phi_k|^2, \tag{3.22}$$

$$\chi_\phi \cong \frac{\sqrt{3}}{3}\sum_k \frac{(2A\tau)^{1/3}}{|k_\parallel c_s|^{2/3}} \frac{\sqrt{\omega_T^2-\omega_{T,\mathrm{crit}}^2}}{|\omega_T|^{4/3}} k_\theta^2 \rho_s^2 |\phi_k|^2. \tag{3.23}$$

$\nabla V_\parallel$ and ∇T_{i0} are coupled nonlinearly in $\Pi_{r\parallel}^{Res}$, via $\sqrt{\omega_T^2-\omega_{T,\mathrm{crit}}^2}$. Therefore, $\Pi_{r\parallel}^{Res}$ *cannot in general be decomposed into the sum of a* ∇T_{i0} *driven piece and a* $\nabla V_\parallel$ *driven piece*. Here, it is the frequency shift $\sqrt{\omega_T^2-\omega_{T,\mathrm{crit}}^2}$ which determines the instability and thus sets the residual stress and χ_ϕ.

The residual stress requires symmetry breaking. A perturbation to the mean flow gradient, $\delta V_\parallel'$, breaks the $k_\parallel \to -k_\parallel$ symmetry. As shown by Eq.3.18, modes with $k_\theta k_\parallel \delta V_\parallel' > 0$ have lower $\omega_{T,\mathrm{crit}}^2$ than others. Therefore, these modes grow faster because $\gamma_k \sim \sqrt{\omega_T^2-\omega_{T,\mathrm{crit}}^2}$. As a result, a spectral imbalance in $k_\theta k_\parallel$ space is induced. For example, for $V_\parallel' < 0$, modes in the $k_\theta k_\parallel < 0$ domain have higher intensities. Therefore, the correlator is set to be $\langle k_\theta k_\parallel \rangle < 0$. Further, the residual stress is set by the spectral imbalance as

$$\Pi_{r\parallel}^{Res} \cong \frac{2\sqrt{3}}{3} \sum_{\{k|k_\theta k_\parallel<0\}} \frac{(2A)^{2/3}}{\tau^{1/3}|k_\parallel c_s|^{4/3}} \frac{\sqrt{\omega_T^2-\omega_{T,\mathrm{crit}}^2}}{|\omega_T|^{2/3}} |k_\theta k_\parallel| \rho_s c_s I_k(\delta V_\parallel'), \tag{3.24}$$

where $I_k(\delta V_\parallel') \equiv |\phi_k|^2 - |\phi_{-k}|^2$ accounts for the turbulence intensity difference and so the summation is only over the domain where $k_\theta k_\parallel < 0$.

This symmetry breaking mechanism induces a positive increment to the turbulent viscosity. $\delta V_\parallel'$ raises the PSFI level, and so enhances the turbulent viscosity. We consider the response of $\Pi_{r\parallel}^{Res}$ in the presence of a test flow shear $\delta V_\parallel'$. The perturbed complex mode frequency due to

$\delta V_{\parallel}'$ is

$$\delta\omega \cong e^{i\delta\theta_k}\frac{\sqrt{3}}{2C_0}\frac{|k_{\parallel}c_s|^{2/3}}{(2A\tau)^{1/3}}\frac{\omega_{T,\mathrm{crit}}^2}{|\omega_T|^{2/3}\sqrt{\omega_T^2-\omega_{T,\mathrm{crit}}^2}}\frac{k_\theta k_{\parallel}\rho_s c_s \delta V_{\parallel}'}{k_{\parallel}^2 c_s^2}, \tag{3.25}$$

with perturbed mode phase $\delta\theta_k = \pi/2$. $\delta\theta_k$ is the same as PSFI mode phase, indicating that $\delta V_{\parallel}'$ enhances PSFI turbulence. The mode phase in this regime can be obtained from the complex frequency, which is

$$\omega \cong e^{i\theta_k}\frac{|k_{\parallel}c_s|^{2/3}}{(2A\tau)^{1/3}}\frac{\sqrt{4\omega_T^2-\omega_{T,\mathrm{crit}}^2}}{\sqrt{3}|\omega_T|^{2/3}}, \tag{3.26}$$

with mode phase $\theta_k = \pi - \varepsilon$ where $\varepsilon \equiv \arctan\sqrt{(\omega_T^2-\omega_{T,\mathrm{crit}}^2)/3\omega_T^2} \gtrsim 0$. As a result, the residual stress in response to $\delta V_{\parallel}'$ can be written as a diffusive momentum flux $\delta\Pi_{r\parallel}^{Res} = -\chi_\phi^{Res}\delta V_{\parallel}'$ with viscosity $\chi_\phi^{Res} \sim \cos(\pi/2+\delta\theta_k-3\theta_k) = \cos(3\varepsilon) > 0$. This means *the residual stress induces a positive increment to the turbulent viscosity.* Following the same calculation procedure as in Ref.[LDXT16a], we can obtain the residual stress in terms of $\nabla V_{\parallel}$ and $\delta V_{\parallel}'$, which is $\Pi_{r\parallel}^{Res}(\nabla V_{\parallel} + \delta V_{\parallel}') = \Pi_{r\parallel}^{Res}(\nabla V_{\parallel}) - \chi_\phi^{Res}\delta V_{\parallel}'$, with

$$\chi_\phi^{Res} \cong \frac{4^{4/3}}{3^{5/2}}\sum_k \frac{C_0^2}{A^{1/3}}\frac{\tau^{5/3}}{|\omega_T|^{2/3}}\frac{k_\theta^2\rho_s^2|k_{\parallel}c_s|^{2/3}}{\sqrt{\omega_T^2-\omega_{T,\mathrm{crit}}^2}}|\phi_k|^2. \tag{3.27}$$

Therefore, $\delta V_{\parallel}'$ *enhances flow dissipation.*

One can also consider the rise in flow dissipation in terms of parallel Reynolds power density. The parallel Reynolds power density is defined as $P_{\parallel}^R \equiv \langle \tilde{v}_r\tilde{v}_{\parallel}\rangle V_{\parallel}'$. It accounts for the rate of energy coupled from fluctuations to mean parallel flow. When $P_{\parallel}^R > 0$, mean flow gains energy from fluctuations, and vice versa. The perturbed Reynolds power due to $\delta V_{\parallel}'$ is then $\delta P_{\parallel}^R = \left(-\chi_\phi\delta V_{\parallel}' + \delta\Pi_{r\parallel}^{Res}\right)V_{\parallel}' = -\left(\chi_\phi + \chi_\phi^{Res}\right)V_{\parallel}'\delta V_{\parallel}'$. Assuming $\delta V_{\parallel}'$ has the same sign as $V_{\parallel}'$, $\chi_\phi^{Res} > 0$ increases the rate at which energy is coupled from mean flow to fluctuations. Thus, flow dissipation is enhanced.

Though the marginal pure ITG turbulence cannot drive intrinsic flows in a straight field, it can influence the flow profile driven by external sources. The final flow profile set by ITG turbulence can be obtained from Eq.5.18, which is $\nabla V_{\|} = \Pi^{Res}_{r\|}/\chi_\phi$. Because $\nabla V_{\|}$ and ∇T_{i0} are nonlinearly coupled via the frequency shift $\sqrt{\omega_T^2 - \omega_{T,\mathrm{crit}}^2}$, their effects on the residual stress cannot be separated. *However, the nonlinear dependence on $\nabla V_{\|}$ cancels, via the ratio between $\Pi^{Res}_{r\|}$ and χ_ϕ.* In order to see the flow profile's scaling with ∇T_{i0}, the factors induced by symmetry breaking effects are ignored. As a result, the estimated residual stress is

$$|\Pi^{Res}_{r\|}| \approx \frac{2\sqrt{3}}{3}\sum_k \frac{(2A)^{2/3}}{\tau^{1/3}|k_{\|}c_s|^{4/3}} \frac{\sqrt{\omega_T^2 - \omega_{T,\mathrm{crit}}^2}}{|\omega_T|^{2/3}} |k_\theta k_{\|}|\rho_s c_s |\phi_k|^2, \tag{3.28}$$

which is an upper limit for $\Pi^{Res}_{r\|}$ since $|\sum_k k_\theta k_{\|}|\phi_k|^2| \leq \sum_k |k_\theta k_{\|}||\phi_k|^2$. The fluctuation intensity, $|\phi_k|^2$, enters both $\Pi^{Res}_{r\|}$ and χ_ϕ, and so drops out of their ratio. Therefore, the parallel flow gradient emerges as

$$|V_{\|}'| = \frac{|\Pi^{Res}_{r\|}(\nabla V_{\|}, \nabla T_{i0})|}{\chi_\phi(\nabla V_{\|}, \nabla T_{i0})} \sim 2^{4/3}A^{1/3}\left(\frac{|\omega_T|}{\tau|k_{\|}c_s|}\right)^{2/3}\frac{|k_{\|}|c_s}{k_\theta\rho_s}. \tag{3.29}$$

The above scaling of $\nabla V_{\|}$ can be illustrated on a back-of-envelope level. Given by Eq.3.13 and Eq.3.14, the ITG residual stress and turbulent viscosity scale as $\Pi^{Res}_{r\|} \sim \Re(i\omega_T/\tau\omega^2)$ and $\chi_\phi \sim \Re(i/\tau\omega)$, where $\omega \equiv \omega_k + i\gamma_k$ is the complex mode frequency, and $\omega_T \equiv k_\theta\rho_s c_s/L_T$ is the ion drift frequency. For ITG turbulence, $\gamma_k \sim |\omega_k| \sim (|\omega_T|/\tau)^{2/3}$. Therefore, the flow gradient scales as $\nabla V_{\|} \sim \Pi^{Res}_{r\|}/\chi_\phi \sim (|\omega_T|/\tau)^{2/3}|k_{\|}c_s|^{1/3}$.

3.5.2 ITG Regime

Now we consider ITG turbulence well above threshold ($\omega_T^2 \gg \omega_{T,\mathrm{crit}}^2$) with the $\nabla V_{\|}$ effect as a first order correction. In this regime, a test flow shear $\delta V_{\|}'$ induces a negative correction to the viscosity. However, unlike the case of electron drift wave (EDW) turbulence, the total viscosity in ITG turbulence is positive definite. Therefore, *no intrinsic flow can be driven by*

ITG turbulence without symmetry breaking due to the magnetic configuration. The difference in flow dissipations between EDW and ITG turbulence raises the quesiton: is flow reversal possible in CSDX? Even though the answer seems to be negative, it suggests that speculations about flow reversal can be tested in fundamental plasma experiments.

The residual stress can be obtained using the growth rate and frequency, which are

$$\gamma_k \cong \frac{\sqrt{3}}{2} \frac{|\omega_T|^{1/3} |k_\parallel c_s|^{2/3}}{(\tau A)^{1/3}} \left[1 - \left(\frac{\omega_{T,\mathrm{crit}}}{2|\omega_T|} \right)^{2/3} \right], \tag{3.30}$$

$$\omega_k \cong -\frac{1}{2} \frac{|\omega_T|^{1/3} |k_\parallel c_s|^{2/3}}{(\tau A)^{1/3}} \left[1 + \left(\frac{\omega_{T,\mathrm{crit}}}{2|\omega_T|} \right)^{2/3} \right]. \tag{3.31}$$

The leading order complex mode frequency is

$$\omega \cong e^{i2\pi/3} \frac{|\omega_T|^{1/3} |k_\parallel c_s|^{2/3}}{(\tau A)^{1/3}}, \tag{3.32}$$

with mode phase $\theta_k = 2\pi/3$. Therefore, the residual stress and turbulent viscosity in this regime are

$$\Pi_{r\parallel}^{Res} \cong -\frac{\sqrt{3}}{2} \sum_k \frac{|\omega_T|^{1/3} A^{2/3}}{\tau^{1/3} |k_\parallel c_s|^{4/3}} k_\theta k_\parallel \rho_s c_s |\phi_k|^2, \tag{3.33}$$

$$\chi_\phi \cong \frac{\sqrt{3}}{2} \sum_k \frac{(\tau A)^{1/3}}{|\omega_T|^{1/3} |k_\parallel c_s|^{2/3}} k_\theta^2 \rho_s^2 |\phi_k|^2. \tag{3.34}$$

$\delta V_\parallel'$ induces a negative viscosity increment. Similar to the case of marginal regime, the residual stress is set by the spectral imbalance, which, given a flow shear $\delta V_\parallel' < 0$, is

$$\Pi_{r\parallel}^{Res} \cong \frac{\sqrt{3}}{2} \sum_{\{k | k_\theta k_\parallel < 0\}} \frac{|\omega_T|^{1/3} A^{2/3}}{\tau^{1/3} |k_\parallel c_s|^{4/3}} |k_\theta k_\parallel| \rho_s c_s I_k(\delta V_\parallel'). \tag{3.35}$$

The perturbed complex mode frequency due to a test flow shear $\delta V_\parallel'$ is

$$\delta\omega = e^{i\pi/3}\left(\frac{\tau}{|\omega_T|}\right)^{1/3}\frac{k_\theta k_\parallel \rho_s c_s \delta V_\parallel'}{3A^{2/3}|k_\parallel c_s|^{2/3}}, \tag{3.36}$$

with the perturbed mode phase $\delta\theta_k = \pi/3$. Since ITG instability is well established (i.e. $\omega_T^2 \gg \omega_{T,\mathrm{crit}}^2$), the test flow shear not only perturbs the growth rate, but also affects the real frequency. Therefore, the perturbed mode phase carries features of both PSFI and ITG mode phases. Since $\chi_\phi^{Res} \sim \cos(3\theta_k - \delta\theta_k - \pi/2) = \cos(5\pi/6) < 0$, the residual stress induces a negative viscosity increment, which is

$$\chi_\phi^{Res} = -\frac{\sqrt{3}}{6}\sum_k \frac{(\tau A)^{1/3}}{|\omega_T|^{1/3}|k_\parallel c_s|^{2/3}} k_\theta^2 \rho_s^2 |\phi_k|^2. \tag{3.37}$$

This negative viscosity increment reduces the rate of energy coupling from mean flow profile to fluctuations, since the Reynolds power density due to $\delta V_\parallel'$ in this case is $\delta P_\parallel^{Res} = -\left(\chi_\phi - |\chi_\phi^{Res}|\right) V_\parallel' \delta V_\parallel'$. Therefore, $\delta V_\parallel'$ *reduces* flow dissipation, and so can *enhance* the flow gradient, since $\nabla V_\parallel \sim \Pi_{r\parallel}^{Res}/\chi_\phi$.

However, $\delta V_\parallel'$ *cannot self-amplify, though it induces a negative viscosity increment*. The dynamics of $\delta V_\parallel$ is determined by $\partial_t \delta V_\parallel' = \chi_\phi^{Tot}\partial_r^2 \delta V_\parallel'$, with growth rate $\gamma_q = -q_r^2 \chi_\phi^{Tot}$. Here, the *total* viscosity, $\chi_\phi^{Tot} = \chi_\phi - |\chi_\phi^{Res}|$, is *positive definite*, because $|\chi_\phi^{Res}| = \frac{1}{3}\chi_\phi$, which can be obtained by comparing Eq.3.34 and Eq.3.37. *Since $\chi_\phi^{Tot} > 0$, the growth rate γ_q is negative, so the flow shear modulation is damped.* This is also shown by the Reynolds power density. Since $\chi_\phi^{Tot} > 0$, the Reynolds power density is negative, and thus *energy is coupled from mean flow profile to fluctuations*, though at a reduced rate due to $\chi_\phi^{Res} < 0$. Table 3.3 summarizes the comparison between $\delta V_\parallel'$ induced symmetry breaking in ITG turbulence and electron drift wave turbulence.

In order to calculate the flow profile, we need to eliminate the residual stress' nonlinearity in $\nabla V_\parallel$. In the ITG regime, $\nabla V_\parallel$ effects can decouple from ∇T_{i0}. This is because ∇T_{i0} is well above the stability boundary, and dominates over $\nabla V_\parallel$ in magnitude. Moreover, the resid-

Table 3.3: Compare $\delta V_{\|}'$ induced symmetry breaking in ITG turbulence and electron drift wave turbulence. The total viscosity, $\chi_\phi^{Tot} = \chi_\phi + \chi_\phi^{Res}$, determines the modulational growth rate of $\delta V_{\|}'$ which is $\gamma_q = -\chi_\phi^{Tot} q_r^2$ with q_r being the radial mode number of the shear modulation $\delta V_{\|}'$.

	ITG Turbulence	Electron Drift Wave
Direction of correlator	$\langle k_\theta k_{\|}\rangle \delta V_{\|}' > 0$	$\langle k_\theta k_{\|}\rangle \delta V_{\|}' > 0$
Viscosity increment by $\delta\Pi_{r\|}^{Res}$	$\chi_\phi^{Res} < 0$	$\chi_\phi^{Res} < 0$
Total viscosity χ_ϕ^{Tot}	positive	can be negative
Modulations	stable	can be unstable

ual stress induces an negative viscosity increment χ_ϕ^{Res}. Therefore, the residual stress can be linearized as

$$\Pi_{r\|}^{Res}(\nabla T_{i0}, \delta V_{\|}') \approx \Pi_{r\|}^{Res}(\nabla T_{i0}) + |\chi_\phi^{Res}(\nabla T_{i0})| \delta V_{\|}'. \tag{3.38}$$

The up-gradient component results from the symmetry breaking by $\delta V_{\|}'$.

The negative incremental viscosity χ_ϕ^{Res} induced by the residual stress regulates the transport of mean flow. Therefore, in response to a mean flow gradient, the residual stress can induce an up-gradient momentum flux, i.e. $\Pi_{r\|}^{Res}(\nabla T_{i0}, V_{\|}') \approx \Pi_{r\|}^{Res}(\nabla T_{i0}) + |\chi_\phi^{Res}| V_{\|}'$. This leads to Eq.3.39, which calculates the mean flow gradient. Such "negative viscosity" phenomena are well known in geophysical fluid dynamics and magnetized plasmas.

With $\Pi_{r\|}^{Res}(\nabla T_{i0})$, $\chi_\phi(\nabla T_{i0})$ and $\chi_\phi^{Res}(\nabla T_{i0})$ given by Eq. 3.33, 3.34, and 3.37, the flow gradient is

$$|V_{\|}'| = \frac{|\Pi_{r\|}^{Res}(\nabla T_{i0})|}{\chi_\phi(\nabla T_{i0}) - |\chi_\phi^{Res}(\nabla T_{i0})|} \sim \frac{3}{2} A^{1/3} \left(\frac{|\omega_T|}{\tau |k_{\|} c_s|} \right)^{2/3} \frac{|k_{\|}| c_s}{k_\theta \rho_s}. \tag{3.39}$$

Eq.3.39 is an upper bound for the intrinsic $V_{\|}'$ driven by ITG turbulence. Again, $\nabla V_{\|}$ follows the general trend revealed by scalings of Eq.3.13 and Eq.3.14, i.e. $\nabla V_{\|} \sim (|\omega_T|/\tau)^{2/3} |k_{\|} c_s|^{1/3}$.

Can there be flow reversal in CSDX, given the different effects of ITG and EDW turbulence on momentum transport? In tokamaks, reversal refers to the phenomenon where the global toroidal rotation profile spontaneously changes direction. The rotation direction flips when density increases and exceeds n_{sat}, the critical density that triggers the transition from the linear ohmic confinement (LOC) to saturated ohmic confinement (SOC) regime. Also, hysteresis is observed as density is ramped down and the rotation direction flips back. The LOC to SOC transition is thought to be triggered by a change in turbulence population from trapped electron mode (TEM) to ITG. Thus, it is speculated that the Ohmic reversal is due to a change in the sign of $\Pi_{r\|}^{Res}$ triggered when the collisionality $\nu^* > \nu^*_{crit}$, which corresponds to $n > n_{sat}$, tending to drive the turbulence to ITG. Recent simulations show that a flip in the sign of $\Pi_{r\|}^{Res}$ can occur in the weak shear regime [LWD$^+$15].

One wonders if these speculations about flow reversal can be tested in basic plasma experiments. The positive definite χ_ϕ^{Tot} in ITG turbulence, in both weakly and strongly unstable regimes, suggests that flow reversal-by a change in the mode type from electron drift wave (EDW) to ITG-seems unlikely in CSDX. With no-slip boundary condition, the flow profile in CSDX is calculated in Ref.[LDXT16a], which is

$$V_\| = \int_r^a dr \frac{a\Delta P_i}{2\rho_0 L \chi_\phi^{\mathrm{Tot}}}. \tag{3.40}$$

Here, ΔP_i is the ion pressure drop in the axial direction induced by the plasma heating on one end of the cylindrical tube. ρ_0 is plasma density and L is axial length of the tube. When the major mode type flips between EDW and ITG, the direction of pressure drop doesn't change, so the direction of flow depends on the sign of total viscosity, i.e. $V_\| \sim 1/\chi_\phi^{Tot}$. It should be noted that in the realistic ITG regime of CSDX, the ITG residual stress may be weak, compared to external flow drives. Thus, we view the axial ΔP_i as the main flow drive in the ITG regime here. In EDW, χ_ϕ^{Tot} is kept positive by the PSFI contribution, i.e. $\chi_\phi^{Tot} = \chi_\phi^{EDW} + \chi_\phi^{PSFI} - |\chi_\phi^{Res}| > 0$. Note that the nonlinear dependence of χ_ϕ^{Tot} on $\nabla V_\|$ determines the magnitude of saturated flow gradient. In marginal ITG turbulence, $\chi_\phi^{Res} > 0$ so χ_ϕ^{Tot} is positive. Also, when ITG turbulence is well above the linear threshold, even though $\delta V_\|'$ drives $\chi_\phi^{Res} < 0$, the *total* viscosity, $\chi_\phi^{Tot} = \chi_\phi - |\chi_\phi^{Res}|$, remains positive since $|\chi_\phi^{Res}|/\chi_\phi = 1/3$. Therefore, in ITG turbulence, χ_ϕ^{Tot} is positive definite.

As a result, when the mode type flips from EDW to ITG, the sign of χ_ϕ^{Tot} does not change, and so the flow does not reverse.

3.5.3 PSFI Regime

In CSDX, $\nabla V_{||}$ can be driven and enhanced by various external sources. When the flow gradient is above the PSFI regime boundary, PSFI controls the turbulence. Note that the PSFI regime boundary ($|V_{||}'|_{\text{reg}}$) is above the linear PSFI threshold ($|V_{||}'|_{\text{crit}}$). In the PSFI regime, both PSFI and ITG instability are above their linear instability thresholds. Due to the PSFI relaxation, the flow profile gradient saturates at $|V_{||}'|_{\text{reg}}$, i.e. $|V_{||}'|_{\text{crit}} \ll |V_{||}'| \sim |V_{||}'|_{\text{reg}} \sim (\nabla T_{i0})^{2/3}$.

The turbulent viscosity by PSFI turbulence is nonlinear in $\nabla V_{||}$, which leads to the saturation of flow gradient. The growth rate and real frequency in the PSFI regime are

$$\gamma_k \cong \frac{|k_{||}c_s|}{\sqrt{A}}\sqrt{V' - C_0}, \tag{3.41}$$

$$\omega_k \cong -\frac{|\omega_T|}{2\tau(V' - C_0)}. \tag{3.42}$$

The growth rate is nonlinear in $\nabla V_{||}$, while the real frequency is negative as a result of ∇T_{i0} effects. Hence, the turbulent viscosity is

$$\chi_\phi = \sum_k \frac{\sqrt{A}}{|k_{||}c_s|\sqrt{V' - C_0}} k_\theta^2 \rho_s^2 |\phi_k|^2. \tag{3.43}$$

The nonlinear dependence of χ_ϕ on $\nabla V_{||}$ indicates that the flow gradient can saturate. As a result, $|V_{||}'|$ *saturates at the PSFI regime boundary which is above the linear PSFI threshold* (Fig.3.3), i.e.

$$|V_{||}'| \approx |V_{||}'|_{\text{reg}} = \frac{3}{2^{2/3}} A^{1/3} \left(\frac{|\omega_T|}{\tau |k_{||}c_s|} \right)^{2/3} \frac{|k_{||}|c_s}{k_\theta \rho_s}. \tag{3.44}$$

Therefore, the saturated flow gradient is *above* the linear PSFI threshold, and grows with ∇T_{i0}

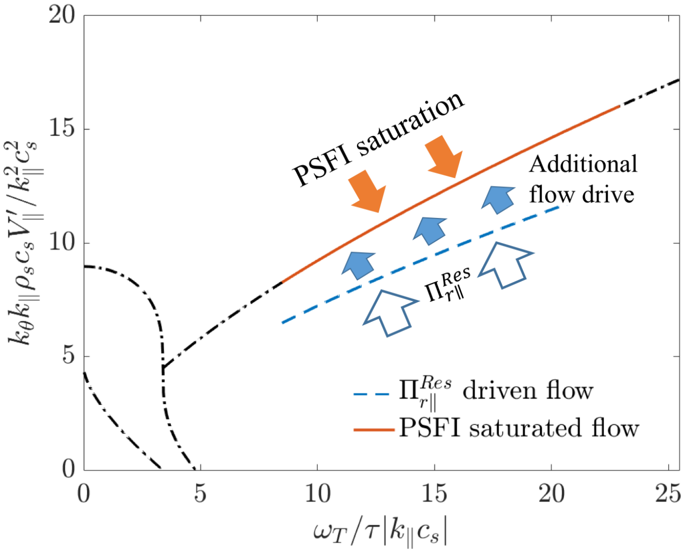

Figure 3.3: The additional flow drive can push the flow across the PSFI threshold, triggering nonlinear PSFI relaxation. The flow gradient is then kept near the PSFI regime boundary as a result of balancing between PSFI saturation and total flow drive.

as shown by Eq.3.44, i.e. $|V'_\||_{\text{crit}}/|k_\| c_s| \ll |V'_\||/|k_\| c_s| \sim |\nabla T_{i0}|^{2/3}/(k_\| T_{i0})^{2/3}$.

3.6 Discussion

In this paper, we have explored the physics of axial flow generation in ITG turbulence, and of axial flow stiffness. The main results in this paper are as follows:

- We have shown that pure ITG turbulence cannot drive intrinsic flows in a straight magnetic field, but can induce a negative viscosity *increment*, which reduces the turbulent flow dissipation.
- PSFI saturates the flow gradient, when $\nabla V_\|$ is driven above the PSFI regime boundary.
- The flow gradient saturates at the PSFI regime boundary, which is above the PSFI linear threshold and tracks the ITG drive, i.e. $\nabla V_\| / |k_\| c_s| \sim (\nabla T_{i0})^{2/3}/(k_\| T_{i0})^{2/3}$.

Below we discuss these results.

Negative compressibility leads to a negative viscosity increment in a straight magnetic field. When the ITG turbulence is well above its stability boundary, a perturbation to the flow gradient $\delta V_{\|}'$ results in a negative viscosity increment, $\chi_\phi^{Res} < 0$. The total viscosity is then reduced, i.e. $\chi_\phi^{Tot} = \chi_\phi - |\chi_\phi^{Res}|$. However, $\delta V_{\|}'$ cannot reinforce itself because χ_ϕ^{Tot} is always positive (since $|\chi_\phi^{Res}| = \frac{1}{3}\chi_\phi$). This means that in order to drive an intrinsic flow, $\Pi_{r\|}^{Res}$ requires other symmetry breaking mechanisms that likely involve magnetic shear. Therefore, there is no intrinsic flow driven by pure ITG turbulence in straight fields. In CSDX, axial flows can be driven various external drives, e.g. end plate biasing and axial ion pressure drop.

In straight magnetic fields, the flow gradient can saturate due to PSFI relaxation. The flow gradient in CSDX can be enhanced by various external sources. When $\nabla V_{\|}$ steepens enough, so that PSFI drive dominates over ITG drive, flow gradient saturates by PSFI relaxation. PSFI is nonlinear in $\nabla V_{\|}$, and so is the viscosity driven by PSFI turbulence. Consequently, $\nabla V_{\|}$ saturates at the PSFI regime boundary (which is above the linear PSFI threshold) and grows as $\nabla V_{\|} \sim (\nabla T_{i0})^{2/3}$. This scaling of flow gradient implies a generalized Rice-type scaling, i.e. $\nabla V_{\|} \sim (\nabla T_{i0})^{\alpha}$, with $\alpha = 2/3$.

We can also solve for the saturated flow gradient from Eq.3.40. The PSFI saturation effect can be accommodated in Eq.3.40 by introducing the PSFI induced turbulent viscosity χ_ϕ^{PSFI} (given by Eq.3.43) when the flow shear is above the PSFI stability boundary. As a result, the total viscosity is

$$\chi_\phi^{Tot} = \begin{cases} \chi_\phi^{ITG} - \chi_\phi^{Res} & \text{if } |V_{\|}'| < |V_{\|}'|_{\text{crit}} \\ \chi_\phi^{ITG} + \chi_\phi^{PSFI} - \chi_\phi^{Res} & \text{if } |V_{\|}'| \geq |V_{\|}'|_{\text{crit}} \end{cases} \tag{3.45}$$

Hence, Eq.3.40 becomes a nonlinear equation for $\nabla V_{\|}$, due to the contribution of χ_ϕ^{PSFI}. Since χ_ϕ^{PSFI} is nonlinear in $\nabla V_{\|}$, it becomes very strong compared to $\chi_\phi^{ITG} - \chi_\phi^{Res}$ when PSFI is sufficiently excited. Therefore, the flow gradient solved from Eq.3.40 saturates at the PSFI regime boundary.

This generalized scaling of $\nabla V_{\|}$ with ∇T_{i0} indicates that the interaction between flow profile and the turbulence drive exhibits simple trends. In ITG turbulence, $\nabla V_{\|}$ and ∇T_{i0} are coupled nonlinearly. But due to the ITG residual stress and PSFI saturation, their final states are constrained by the scaling $\nabla V_{\|} \sim (\nabla T_{i0})^{2/3}$.

Even though $\delta V_{\|}'$ has different effects on electron drift wave (EDW) and ITG turbulence, flow reversal by changing the mode from EDW to ITG seems unlikely. As is known, the axial flow in CSDX is driven by ion pressure drop in the axial direction (ΔP_i), which is $V_{\|} \sim \int_r^a \Delta P_i / \chi_\phi^{Tot}$. In EDW, the negative viscosity increment induced by $\delta V_{\|}'$ can turn the total viscosity negative in some transient state, i.e. $\chi_\phi^{Tot} = \chi_\phi - |\chi_\phi^{Res}| < 0$. Nevertheless, in the final state, the self-amplification of a test flow shear is saturated by PSFI, so the total viscosity remains positive due to the PSFI contribution, i.e. $\chi_\phi^{Tot} = \chi_\phi^{EDW} + \chi_\phi^{PSFI} - |\chi_\phi^{Res}| > 0$. When ITG turbulence is excited, χ_ϕ^{Tot} driven by ITG is positive definite. Thus, for the same flow boundary condition, the sign of χ_ϕ^{Tot} does not change, despite change in mode. Therefore, flow reversal in CSDX will *not* track changes in turbulence.

The following works are proposed for the future. They address remaining issues about flow generation and saturation in CSDX. First, ion-neutral coupling mostly occurs in the boundary layer in CSDX, where plasmas are partially ionized. However, it sets the boundary condition for parallel flows, and thus affects the global flow structure. Since flow profile is very sensitive to the boundary condition, ion-neutral coupling is of great interest. Second, coupling between perpendicular flow and parallel flow. In tokamaks, poloidal flow and toroidal flow are coupled by sheared magnetic fields. Even though CSDX has straight field lines, the parallel flow gradient ($\nabla V_{\|}$) can be coupled to perpendicular flow gradient ($\nabla V_{\perp}$) via the turbulence [WDH12b]. Particularly, a sheared perpendicular flow can saturate the parallel flow gradient in CSDX. Because both $\nabla V_{\perp}$ and $\nabla V_{\|}$ are driven by the background turbulence, their magnitudes are limited by Reynolds power density, which measures the rate at which fluctuations transfer energy to mean flows. The coupling between perpendicular and parallel flows can also be viewed as an extended predator-prey model [ADG16, AD16] in which $\nabla V_\perp$ and $\nabla V_\|$ are two predators (perhaps hierarchical) and the turbulence is the prey. Third, reversal dynamics remains an open question. As is known, flow reversal is unlikely in CSDX by changing the mode from electron drift wave (EDW) to ITG, because PSFI saturation of $\nabla V_\|$ in EDW turbulence keeps the total viscosity positive. However, $\nabla V_\perp$ saturation complicates the problem of flow reversal. The bottom line is that such predictions for flow reversal can be tested in basic plasma experiments.

Chapter 3 is a reprint of the material as it appears in J. C. Li and P. H. Diamond, "Negative viscosity from negative compressibility and axial flow shear stiffness in a straight magnetic field", *Physics of Plasmas* **24**, 032117 (2017), American Institute of Physics. The dissertation author was the primary investigator and author of this article.

Chapter 4

Interaction of Turbulence-Generated Azimuthal and Axial Flows in CSDX

4.1 Introduction

Intrinsic flows of plasmas are beneficial to magnetic confinement and MHD control[RHS$^+$06, MAC$^+$11a]. Intrinsic flows occur both parallel to the magnetic field (e.g., toroidal rotations in tokamaks[RHD$^+$11b] and axial flows in linear devices[HLH$^+$18]) and perpendicular to the magnetic field (e.g., zonal flows[DIIH05b, GD15, AD16]). The generation of such flows may be understood using the heat engine paradigm[KDG10a]. Initially driven by profile gradients (such as ∇T and/or ∇n), the turbulence energy is coupled to both parallel and perpendicular flows. Thus, the key questions are:

(1) What is the branching ratio, i.e., the fraction of fluctuation energy coupled to parallel flows, relative to that coupled to perpendicular flows?

(2) What are the feedback and coupling mechanisms linking intrinsic parallel and perpendicular flows?

As the intrinsic flows are driven by the Reynolds forces, the branching ratio is defined as the ratio of parallel to perpendicular Reynolds powers. The Reynolds power is the product of Reynolds force and flow velocity, i.e., $P_{\parallel}^{R} \equiv -\langle \tilde{v}_r \tilde{v}_{\parallel} \rangle' \langle v_{\parallel} \rangle$ and $P_{\theta}^{R} \equiv -\langle \tilde{v}_r \tilde{v}_{\theta} \rangle' \langle v_{\theta} \rangle$. As given by the Taylor identity[Tay15, DK91], the perpendicular Reynolds force is equivalent to vorticity flux, yielding that $P_{\theta}^{R} = \langle \tilde{v}_r \nabla^2 \tilde{\phi} \rangle \langle v_{\theta} \rangle$. Then, the branching ratio is $P_{\parallel}^{R}/P_{\theta}^{R}$.

The goal is to understand the evolution of fluctuation–flow (i.e., $\langle v_{\theta} \rangle$ and $\langle v_{\parallel} \rangle$) ecology incorporating both parallel and perpendicular flows. This has not been addressed by experiments, or even simulation. However, some existing measurements and models can illuminate the characterization of such an ecology. In a linear device, CSDX (controlled shear decorrelation experiment), the coupling of intrinsic axial (parallel) and and azimuthal (perpendicular) flows is observed to be weak[HLH$^+$18]. In CSDX, the azimuthal flow regulates drift wave turbulence and the axial flow is parasitic. Indeed, in the regime of intrinsic parallel flows, the effect of perpendicular flow is expected to be stronger than that of parallel flow, because $|k_{\parallel}|/k_{\theta} \ll 1$.

The question of what couples the parallel and perpendicular flows, absent magnetic shear, is open. Magnetic shear allows perpendicular flows to break the symmetry in the parallel direction, which results in the generation of intrinsic parallel flows[GDHS07a]. However, this geometrical coupling is not valid at low or zero magnetic shear, such as the flat-q regime in tokamaks and linear devices with uniform magnetic fields. It has long been known that the coupling of potential vorticity and parallel compression (i.e., $\langle \tilde{q} \nabla_{\parallel} \tilde{v}_{\parallel} \rangle$) can convert parallel flows into zonal flows[WDH12b]. But this coupling is weak in the regime of intrinsic parallel flows, due to small $k_{\parallel} L_n$ in CSDX.

In this work, we address the following questions:

(1) What is the branching ratio of turbulence energy between axial and azimuthal flows in CSDX? In particular, we study the effect of incremental changes of perpendicular and parallel flow shears on the branching ratio $P_{\parallel}^{R}/P_{\theta}^{R}$.

(2) How does azimuthal flow shear affect the generation and saturation of intrinsic axial flows,

absent magnetic shear? The axial flow is generated by the modulational instability of test flow shear[LDXT16a]. In presence of a test flow shear, the residual axial Reynolds stress induces a negative viscosity increment χ_z^{Res}. When $|\chi_z^{Res}|$ exceeds the turbulent viscosity driven by drift waves, such that the total viscosity is negative, the test flow shear amplifies itself via the modulational instability. The axial flow shear saturates when the turbulent diffusion becomes strong enough to overcome the residual stress. The saturated flow shear is determined by the balance between residual stress and turbulent viscosity driven by drift waves, i.e., $\langle v_z \rangle' = \Pi_{rz}^{Res}/\chi_z^{DW}$. In this paper, we study how the azimuthal flow shear affects the modulational instability of test flow shear and the saturated axial flow shear.

This work addresses the regime where drift wave is the dominant instability population and wave–flow resonance is weak. This means the axial flow shear discussed here is well below the linear threshold for parallel shear flow instability (PSFI)[LDXT16a, MD88]. Also, perpendicular Kelvin–Helmholtz (KH) instability is negligible because KH drive is much weaker than the ∇n_0 drive, i.e., $|k_\theta \rho_s^2 \langle v_\theta \rangle''| \ll \omega_{*e}$. Here, $\omega_{*e} \equiv k_y \rho_s c_s / L_n$ is the electron drift frequency and $L_n \equiv n_0/|dn_0/dx|$ is the density gradient scale. As a result, we are interested in the regime where $|\langle v_\theta \rangle|/c_s \ll L_{V_\theta}^2/\rho_s L_n$, and L_{V_θ} is the scale length of azimuthal flow shear. Though the wave–flow resonance can be prominent in linear devices, here we ignore the resonance effect for simplicity. In CSDX, where $|k_z|/k_\theta \ll 1$, the main resonance is between drift wave and azimuthal flow, i.e., $\omega_k - k_\theta \langle v_\theta \rangle - k_z \langle v_z \rangle \cong \omega_k - k_\theta \langle v_\theta \rangle \cong \omega_k - k_\theta \langle v_\theta \rangle' \Delta_x$. Δ_x is the distance relative to the reference position. The Doppler shifted drift wave frequency is approximately $\omega_k \sim \omega_{*e}/(1 + k_\perp^2 \rho_s^2)$. Thus, when the value of $|k_\theta \langle v_\theta \rangle' \Delta_x|$ is close to ω_{*e}, the resonance is strong. In this work, we consider the regime where $|k_\theta \langle v_\theta \rangle' \Delta_x| \gg \omega_{*e}$, i.e., $|\langle v_\theta \rangle|/c_s \gg \rho_s L_{V_\theta}/\Delta_x L_n$, and thus resonance is weak. Taken together, we focus on the regime where $\rho_s L_{V_\theta}/\Delta_x L_n \ll |\langle v_\theta \rangle|/c_s \ll L_{V_\theta}^2/\rho_s L_n$.

4.2 Turbulence energy apportionment

We study the apportionment of turbulence energy between azimuthal and axial flows through a modulational study. We incrementally change the azimuthal or axial flow shear, while fixing the other, and study how the branching ratio $P_{\|}^{R}/P_{\theta}^{R}$ changes respectively. Note we ignore the feedback of turbulence-driven flows on the flow profiles. Thus, the flow profiles are determined by fixed external input. In this section, we present the results of this study.

We study the Hasegawa–Wakatani drift wave system coupled with parallel flow fluctuations in slab geometry in the presence of a mean perpendicular (azimuthal) flow $\langle v_y \rangle$ and a mean parallel (axial) flow $\langle v_z \rangle$, both of which vary in the $\hat{x}$ (radial) direction:

$$\frac{d}{dt}\tilde{n} + \tilde{v}_x \frac{\nabla n_0}{n_0} = D_{\|}\partial_z^2(\tilde{n} - \tilde{\phi}) + D_c \nabla^2 \tilde{n}, \tag{4.1}$$

$$\frac{d}{dt}\tilde{\rho} + \tilde{v}_x \langle \rho \rangle' = D_{\|}\partial_z^2(\tilde{n} - \tilde{\phi}) + \chi_c \nabla^2 \tilde{\rho}, \tag{4.2}$$

$$\frac{d}{dt}\tilde{v}_z + \tilde{v}_x \langle v_z \rangle' = -\partial_z \tilde{n}. \tag{4.3}$$

where we define $D_{\|} \equiv v_{The}^2/\nu_{ei}$ and $d/dt \equiv \partial_t + \langle v_y \rangle \partial_y + \langle v_z \rangle \partial_z$. ν_{ei} is electron–ion collision frequency and v_{The} is electron thermal speed. We have normalized electric potential fluctuation as $\tilde{\phi} \equiv e\delta\phi/T_e$ and density fluctuation as $\tilde{n} \equiv \delta n/n_0$, where n_0 is the equilibrium density. The magnetic field is uniform and lies in $\hat{z}$ direction. Both n_0 and $\langle v_y \rangle$ vary only in $\hat{x}$ direction. $\tilde{\rho} \equiv \rho_s^2 \nabla_{\perp}^2 \tilde{\phi}$ is the vorticity fluctuation, where ρ_s is the ion Larmor radius at electron temperature, $\langle \rho \rangle \equiv \langle v_y \rangle' \rho_s / c_s$ is the zonal vorticity where c_s is the ion sound speed. $\tilde{\mathbf{v}}_E \equiv c_s \hat{\mathbf{z}} \times \nabla \tilde{\phi}$ is the $E \times B$ velocity fluctuation. D_c and χ_c are the collisional particle diffusivity and vorticity diffusivity (i.e., viscosity).

Drift wave is the dominant instability population. The vorticity gradient can drive the perpendicular Kelvin–Helmholtz (KH) instability. But the vorticity gradient drive is quantitatively weaker than the ∇n_0 drive, i.e., $|k_y \rho_s^2 \langle v_y \rangle''|/\omega_{*e} \ll 1$ where $\omega_{*e} \equiv k_y \rho_s c_s / L_n$ is the electron drift frequency and $L_n \equiv n_0/|dn_0/dx|$ is the density gradient scale. Also, $|\langle v_z \rangle'|$ is kept well below the PSFI threshold, such that PSFI is stable.

The azimuthal and axial flows are both externally imposed and fixed. We denote them as V_y and V_z to distinguish them from the intrinsic flows. As a result, the dispersion relation is an eigenmode equation for ϕ:

$$\rho_s^2 \frac{d^2\phi}{dx^2} = \left[k_y^2 \rho_s^2 \Omega_k - k_y \rho_s V_y'' + i\alpha \frac{\Omega_k - \omega_{*e}}{\Omega_k + i\alpha} + \frac{k_y k_z V_z'}{\Omega_k} - \frac{k_z^2(\omega_{*e} + i\alpha)}{\Omega_k(\Omega_k + i\alpha)} \right] \phi, \tag{4.4}$$

where $\alpha \equiv k_z^2 v_{The}^2/\nu_{ei}$ and $\Omega_k \equiv \omega_k - k_y V_y - k_z V_z + i\gamma_k$. We can obtain the ϕ profile by using an eigenvalue solver. Here, we set the extent of the radial direction to be $0 \leq x \leq L_x$, where $L_x = 5\rho_s$. We set the parameters in the range relevant to CSDX, which are $\rho_s = 1\text{cm}$, $L_n = 1.5\text{cm}$, $k_y\rho_s = 0.7$, $L_z = 300\text{cm}$, $k_z = -2\pi/L_z$. The adiabatic parameter is $k_z^2 D_\parallel/\omega_{*e} = 3$. The flow profiles are: $V_y = V_{y,max} \sin\left[\pi\left(x/L_x - 0.5\right)\right]$ and $V_z = V_{z,max} \cos\left(\pi x/L_x\right)$. The boundary condition is $\phi(0) = \phi(L_x) = 0$. Then, we can obtain the drift wave frequency ω_k, growth rate γ_k, and ϕ profile.

Using the ϕ profile, we determine the average Reynolds powers, which are:

$$P_y^R = -L_x^{-1} \int_0^{L_x} dx \partial_x \langle \tilde{v}_x \tilde{v}_y \rangle V_y$$

and

$$P_z^R = -L_x^{-1} \int_0^{L_x} dx \langle \tilde{v}_x \tilde{v}_z \rangle' V_z$$

. By Taylor identity[Tay15, DK91], the azimuthal Reynolds force is identical to the vorticity flux, i.e., $-\partial_x \langle \tilde{v}_x \tilde{v}_y \rangle = \langle \tilde{v}_x \tilde{\rho} \rangle$. Hence, the azimuthal Reynolds power becomes $P_y^R = L_x^{-1} \int_0^{L_x} dx \langle \tilde{v}_x \tilde{\rho} \rangle V_y$. The vorticity flux contains a diffusive flux and a residual flux, i.e., $\langle \tilde{v}_x \tilde{\rho} \rangle = -\chi_y V_y'' + \Gamma_\rho^{Res}$. Here, we ignore the resonance between drift wave and the azimuthal and axial flows. Thus, the non-

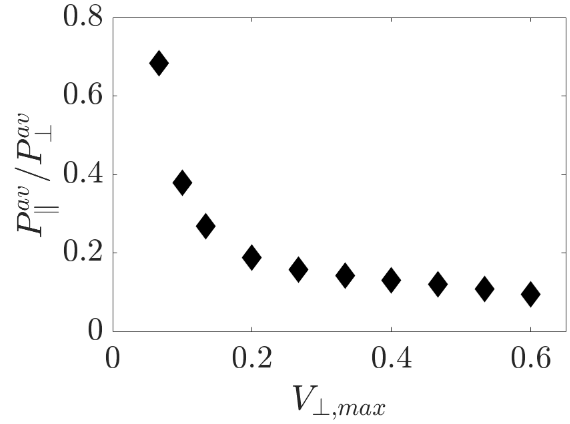

Figure 4.1: Change of branching ratio P_z^R/P_y^R in response to incremental changes of azimuthal flow shear. The axial flow profile is given by $V_y = V_{y,max}\sin\left[\pi\left(x/L_x - 0.5\right)\right]$. Thus, the flow shear changes with the flow magnitude.

resonant turbulent diffusivity of vorticity is

$$\chi_y = \frac{\gamma_k}{|\Omega_k|^2} k_y^2 \rho_s^2 c_s^2 |\phi|^2. \tag{4.5}$$

The residual vorticity flux is

$$\Gamma_\rho^{Res} = k_y c_s^2 |\phi|^2 \left[\frac{\gamma_k \omega_{*e} + \alpha(\omega_{*e} - \Re\Omega_k)}{|\Omega_k + i\alpha|^2} - \frac{\gamma_k \omega_{*e}}{|\Omega_k|^2} + \Re\frac{i}{\Omega_k^2} k_z k_y V_z' - \Re\frac{i k_z^2 (\omega_{*e} + i\alpha)}{\Omega_k^2(\Omega_k + i\alpha)}\right]. \tag{4.6}$$

Similar to the vorticity flux, the axial Reynolds stress contains a diffusive momentum flux and a residual stress, i.e., $\langle \tilde{v}_x \tilde{v}_z \rangle = -\chi_z V_z' + \Pi_{xz}^{Res}$. The non-resonant turbulent diffusivity of axial momentum is

$$\chi_z = \frac{\gamma_k}{|\Omega_k|^2} k_y^2 \rho_s^2 c_s^2 |\phi|^2. \tag{4.7}$$

The residual stress is

$$\Pi_{xz}^{Res} = \Re\frac{i k_y k_z (\omega_{*e} + i\alpha)}{\Omega_k(\Omega_k + i\alpha)} \rho_s c_s^3 |\phi|^2. \tag{4.8}$$

We study the changes of branching ratio of turbulence energy in response to incremental changes of azimuthal and axial flow shears. The branching ratio is the ratio of axial and

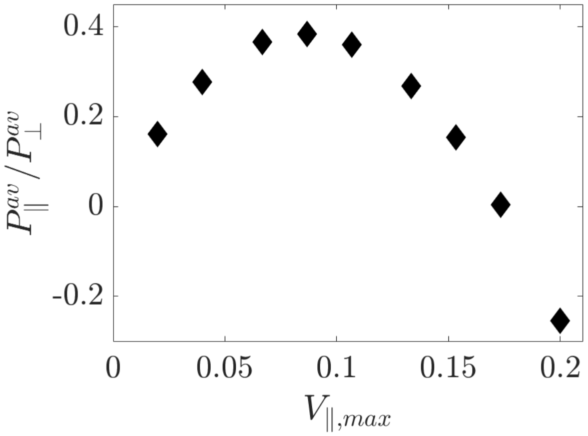

Figure 4.2: Change of branching ratio P_z^R/P_y^R in response to incremental changes of axial flow shear. The axial flow profile is given by $V_z = V_{z,max}\cos(\pi x/L_x)$. Thus, the flow shear changes with the flow magnitude.

azimuthal Reynolds powers P_z^R/P_y^R. It measures the turbulence energy apportionment between axial and azimuthal flows. Fig. 4.1 shows that azimuthal flow shear impedes the turbulent production of axial flow. When increasing the azimuthal flow magnitude and shear, while fixing the axial flow, the ratio P_z^R/P_y^R decreases.

Fig. 4.2 shows that the production of axial flow saturates below the PSFI threshold. When increasing the axial flow magnitude $V_{z,max}$, while fixing the azimuthal flow, the ratio P_z^R/P_y^R first increases. When $V_{z,max}$ continues increasing, the ratio saturates and starts to decrease. Note that the saturation is below the PSFI threshold. Fig. 4.3 shows the growth rate when increasing the axial flow shear. The onset of PSFI requires $V_{z,max}/c_s > 3$. The axial flow production saturates at $V_{z,max}/c_s \sim 0.09$ as given by Fig. 4.2, which is far below the PSFI threshold.

4.3 Azimuthal flow effects on intrinsic axial flow

We study the drift wave system described by Eqs. (4.3), (6.1) and (6.2). Electrons are weakly adiabatic, i.e., $\tilde{n} = (1 - i\delta)\tilde{\phi}$, where the non-adiabatic electron response $\delta < 1$. δ is determined by the frequency shift, i.e. $\delta = (\omega_{*e} - \omega_k - k_y\langle v_y\rangle - k_z\langle v_z\rangle)/k_z^2 D_{\parallel}$. The eigenmode

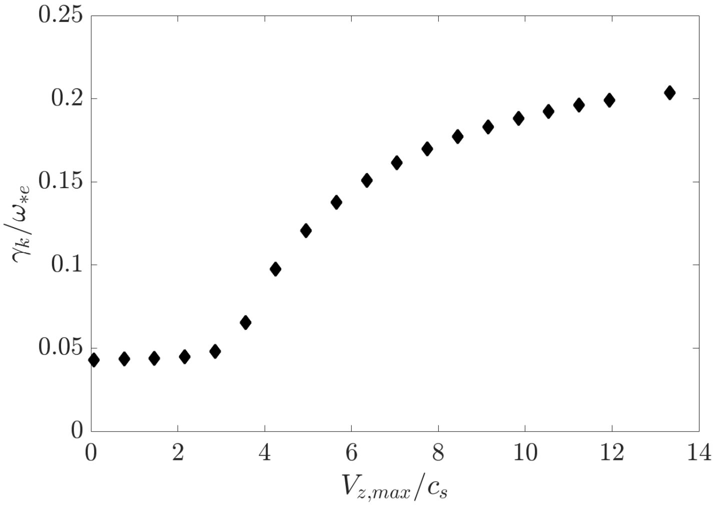

Figure 4.3: Growth rate for various axial flow shears. The axial flow profile is given by $V_z = V_{z,max}\cos(\pi x/L_x)$. Thus, the flow shear changes with the flow magnitude.

equation is

$$\rho_s^2\frac{\partial^2\phi}{\partial x^2} = \left[\left(1+k_y^2\rho_s^2 - i\delta\right) - \frac{\omega_{*e}+k_y\rho_s^2\langle v_y\rangle''}{\Omega_k} + \frac{k_yk_z\langle v_z\rangle'}{\Omega_k^2} - (1-i\delta)\frac{k_z^2c_s^2}{\Omega_k^2}\right]\phi. \tag{4.9}$$

Multiplying both sides of Eq. (4.9) with ϕ^* and integrating over the radial direction, we obtain the linear dispersion relation, which is

$$\left(1+k_\perp^2\rho_s^2 - i\delta\right) - \frac{\omega_{*e}+k_y\rho_s^2\langle v_y\rangle''}{\Omega_k} + \frac{k_yk_z\rho_sc_s\langle v_z\rangle'}{\Omega_k^2} - (1-i\delta)\frac{k_z^2c_s^2}{\Omega_k^2} = 0. \tag{4.10}$$

Here, we define the effective radial wavenumber $k_x^2\rho_s^2 \equiv \rho_s^2\int_0^{L_x}dx|\partial_x\phi|^2/\int_0^{L_x}dx|\phi|^2$. Hence, the perpendicular wavenumber is $k_\perp^2\rho_s^2 \equiv k_x^2\rho_s^2 + k_y^2\rho_s^2$.

Azimuthal flow stabilizes drift wave by weakening the ∇n_0 drive. As observed in the second term in Eq. (4.10), $\langle v_y\rangle''$ weakens the electron drift frequency, when $k_y\rho_s^2\langle v_y\rangle''/\omega_{*e} < 0$. In CSDX, the condition $k_y\rho_s^2\langle v_y\rangle''/\omega_{*e} < 0$ holds true, and thus azimuthal flow shear stabilizes drift waves in CSDX. In the following analysis, we define the weakened drift frequency of electrons as $\overline{\omega_{*e}} \equiv \omega_{*e} + k_y\rho_s^2\langle v_y\rangle''$ and consider the case where $k_y\rho_s^2\langle v_\theta\rangle''/\omega_{*e} < 0$. The Doppler-shifted frequency and linear growth rate are calculated using the dispersion relation, which are

$$\omega_k \cong \frac{\overline{\omega_{*e}}}{1+k_\perp^2\rho_s^2} - \frac{k_y k_z \rho_s c_s \langle v_z\rangle'}{\overline{\omega_{*e}}}, \tag{4.11}$$

$$\gamma_k \cong \frac{1}{k_z^2 D_\parallel} \frac{\overline{\omega_{*e}}^2}{(1+k_\perp^2\rho_s^2)^2} \left(\frac{k_\perp^2\rho_s^2}{1+k_\perp^2\rho_s^2} - \frac{k_y\rho_s^2\langle v_y\rangle''}{\overline{\omega_{*e}}} + \frac{k_y k_z \rho_s c_s \langle v_z\rangle'}{\overline{\omega_{*e}}^2} \right). \tag{4.12}$$

When axial flow shear hits the PSFI threshold

$$|\langle v_z\rangle'|_{\mathrm{crit}} = \frac{1}{|k_y k_z \rho_s c_s|} \left[\frac{\overline{\omega_{*e}}^2 (1+k_\perp^2\rho_s^2)}{4[(1+k_\perp^2\rho_s^2)^2+\delta^2]} + k_z^2 c_s^2 \right], \tag{4.13}$$

the axial flow shear drives the turbulence as a free energy source. Note given $k_y\rho_s^2\langle v_y\rangle''/\omega_{*e} < 0$, the azimuthal flow lowers the PSFI threshold. For weak axial flow shear, i.e. $|\langle v_z\rangle'| \ll |\langle v_z\rangle'|_{\mathrm{crit}}$, the system is dominated by drift wave.

4.3.1 Generation of intrinsic axial flow absent magnetic shear

The intrinsic axial flow in CSDX is driven by drift wave turbulence via the dynamical symmetry breaking mechanism[LDXT16a]. In response to a seed axial flow shear, the residual Reynolds stress induces a negative viscosity increment. When this negative viscosity increment beats the turbulent viscosity driven by drift waves, such that the total viscosity is negative, the seed shear amplifies itself through a modulational instability.

When the axial flow shear steepens, a finite residual stress forms due to the spectral asymmetry of drift wave turbulence. The stationary profile of axial flow shear is then determined by the balance of residual stress and turbulent diffusion of axial momentum by drift waves, i.e. $\langle v_z\rangle' \sim \Pi_{xz}^{Res}/\chi_z^{DW}$.

4.3.2 Azimuthal flow effects on axial residual stress

In this subsection, we show that the azimuthal flow shear stabilizes the modulational growth of the seed axial flow shear. Moreover, azimuthal flow shear reduces the magnitudes of both residual stress and turbulent viscosity. Thus, it does not affect the stationary axial flow shear to leading order.

We calculate the axial Reynolds stress with azimuthal flow effects included, following the same procedures presented in Ref. [LDXT16a]. The axial Reynolds stress can be written as a diffusive momentum flux plus a residual stress, which is

$$\langle \tilde{v}_x \tilde{v}_z \rangle = -\chi_z \frac{\partial \langle v_z \rangle}{\partial x} + \Pi_{xz}^{Res}. \tag{4.14}$$

From Eq. (4.3), we obtain that

$$\tilde{v}_z \sim \frac{|\gamma_k|}{\left(\omega_k - k_y \langle v_y \rangle' \Delta_x\right)^2} k_z c_s^2 \tilde{\phi} \sim \frac{1}{\left(V' - 1\right)^2} \frac{|\gamma_k|}{\omega_k^2} k_z c_s^2 \tilde{\phi}.$$

Here, $V' \equiv k_y \langle v_y \rangle' \Delta_x / \omega_k \sim \langle v_y \rangle \Delta_x L_n / c_s \rho_s L_{V_y}$. Thus, in the non-resonant regime (i.e., $|\langle v_y \rangle| / c_s \gg \Delta_x L_n / \rho_s L_{V_y}$ and so $|V'| \gg 1$), we obtain that

$$\tilde{v}_z \sim \frac{1}{|V'|^2} \frac{|\gamma_k|}{\omega_k^2} k_z c_s^2 \tilde{\phi}. \tag{4.15}$$

As a result, the turbulent viscosity and residual stress are

$$\chi_z^{DW} \cong \sum_k \frac{1}{|V'|^2} \frac{1}{k_z^2 D_\parallel} \left[\frac{k_\perp^2 \rho_s^2}{1 + k_\perp^2 \rho_s^2} + \frac{|k_y \rho_s^2 \langle v_y \rangle''|}{\overline{\omega_{*e}}} \right] k_y^2 \rho_s^2 |\phi_k|^2, \tag{4.16}$$

$$\Pi_{xz}^{Res} \cong \sum_k \frac{1}{|V'|^2} \frac{1}{k_z^2 D_\parallel} (2 + k_\perp^2 \rho_s^2) \left[\frac{k_\perp^2 \rho_s^2}{1 + k_\perp^2 \rho_s^2} + \frac{|k_y \rho_s^2 \langle v_y \rangle''|}{\overline{\omega_{*e}}} + \frac{k_y k_z \rho_s c_s \langle v_z \rangle'}{\overline{\omega_{*e}}^2} \right] k_y k_z \rho_s c_s |\phi_k|^2. \tag{4.17}$$

The residual stress requires symmetry breaking in the k_y–k_z space. Absent magnetic shear, a seed axial flow shear breaks the symmetry and is self-amplified through a modulational instability. As a result, the broken symmetry in the k_y–k_z space emerges along with a finite axial flow shear profile. Hence, with this spectral asymmetry, the residual stress, to leading order, is

$$\Pi_{xz}^{Res} \cong \sum_{k_y k_z \langle v_z \rangle' > 0} \frac{1}{|V'|^2} \frac{2 + k_\perp^2 \rho_s^2}{k_z^2 D_\parallel} \frac{k_\perp^2 \rho_s^2}{1 + k_\perp^2 \rho_s^2} k_y k_z \rho_s c_s I_k, \tag{4.18}$$

where $I_k = |\phi_k|^2 (k_y k_z \langle v_z \rangle' > 0) - |\phi_k|^2 (k_y k_z \langle v_z \rangle' < 0)$ accounts for the spectral imbalance. Therefore, both the residual stress and turbulent viscosity driven by drift waves are reduced by azimuthal flow shear.

Next, we show that the azimuthal flow shear also impedes the self-amplification of seed flow shear, i.e., $\langle v_y \rangle'$ slows down the modulational growth of seed flow shear. In response to a seed axial flow shear $\delta \langle v_z \rangle'$, the residual stress induces a negative diffusion of momentum flux, i.e.,

$$\delta \Pi_{xz}^{Res} \cong |\chi_z^{Res}| \delta \langle v_z \rangle', \tag{4.19}$$

where the negative viscosity increment is

$$\chi_z^{Res} \cong -\frac{1}{|V'|^2} \frac{1}{D_\parallel} \frac{k_y^2 \rho_s^2 c_s^2}{\overline{\omega_{*e}}^2} \sum_k (1 + k_\perp^2 \rho_s^2)(4 + k_\perp^2 \rho_s^2) |\phi_k|^2. \tag{4.20}$$

The growth rate of the flow shear modulation is determined by the difference between $|\chi_z^{Res}|$ and χ_z, i.e.,

$$\begin{aligned} \gamma_q &= q_r^2 (|\chi_z^{Res}| - \chi_z^{DW}) \\ &\cong q_r^2 \sum_k \frac{|\phi_k|^2}{|V'|^2} \frac{k_y^2 \rho_s^2 c_s^2}{k_z^2 D_\parallel} \left(K - \frac{k_\perp^2 \rho_s^2}{1 + k_\perp^2 \rho_s^2} \right) \left(1 + \beta \frac{|k_y \rho_s^2 \langle v_y \rangle''|}{\omega_{*e}} \right), \end{aligned} \tag{4.21}$$

where q_r is the radial modenumber of the shear modulation, $K \equiv (1 + k_\perp^2 \rho_s^2)(4 + k_\perp^2 \rho_s^2) k_z^2 c_s^2 / \omega_{*e}^2$, and $\beta \equiv (2K - 1) \Big/ \left(K - \frac{k_\perp^2 \rho_s^2}{1 + k_\perp^2 \rho_s^2} \right)$. When the negative viscosity induced by the residual stress beats the turbulent viscosity by drift wave, the test flow shear is self-reinforced through a modulational instability. This means $K > k_\perp^2 \rho_s^2/(1+k_\perp^2\rho_s^2)$ is required for modulational growth (i.e., $\gamma_q > 0$) of the test shear. For drift waves, we obtain $k_y\rho_s \sim 1$, and thus $K \sim (2+k_x^2\rho_s^2)(5+k_x^2\rho_s^2) > 10k_z^2 L_n^2$ and $0.5 < k_\perp^2\rho_s^2/(1+k_\perp^2\rho_s^2) < 1$. Modulational instability requires $K > k_\perp^2\rho_s^2/(1+k_\perp^2\rho_s^2) > 0.5$, which is possible for drift waves. As shown by Eq. (4.21), the modulational growth of the seed flow shear decreases when the azimuthal flow shear increases.

4.3.3 Azimuthal flow effects on stationary flow shear profile

The evolution of mean axial flow is described by

$$\frac{\partial\langle v_z\rangle}{\partial t} + \frac{\partial}{\partial x}\langle \tilde{v}_x \tilde{v}_z\rangle = -\frac{\partial P}{\partial z} - \nu_{ni}\left(\langle v_z\rangle - V_n\right). \tag{4.22}$$

The pressure drop in the axial direction is due to the heating on one end of the linear device. In CSDX, this pressure drop is weaker than the Reynolds force ($-\partial_x\langle\tilde{v}_x\tilde{v}_z\rangle$) by an order of magnitude[HLH$^+$18]. Frictions between plasma and neutral flows damp the axial flow in the edge region, where neutral particles concentrate. Hence, neutral damping sets the boundary condition for the axial flow profile. Therefore, in the central region of CSDX, the axial flow is generated and saturated by the axial Reynolds stress. The stationary state flow is determined by $\langle\tilde{v}_x\tilde{v}_z\rangle = 0$. As a result, the stationary axial flow shear, to leading order, is

$$\langle v_z\rangle' = \frac{\Pi_{xz}^{Res}}{\chi_z^{DW}} \sim (2+k_\perp^2\rho_s^2)k_z c_s/k_y\rho_s. \tag{4.23}$$

The azimuthal flow shear reduces both Π_{xz}^{Res} and χ_z^{DW} by the same factor $|V'|^{-2}$. Hence, this reduction effect cancels out to leading order in the stationary axial flow shear, which is determined by the ratio $\Pi_{xz}^{Res}/\chi_z^{DW}$. Therefore, the azimuthal flow shear does not affect the saturated axial flow shear to leading order.

4.4 Discussion

In this work, we have studied the coupling of azimuthal and axial flows in CSDX, absent magnetic shear. In particular, we have studied how incremental changes of flow shears affect the production branching ratio P_z^R/P_y^R. We have also investigated the effects of azimuthal flow shear on intrinsic axial flow generation and saturation, absent magnetic shear. The main results of these studies are:

- Increasing azimuthal flow shear reduces the branching ratio, which is measured by the ratio of axial and azimuthal Reynolds powers, i.e., P_z^R/P_y^R.
- When axial flow shear increases, P_z^R/P_y^R first increases and then decreases. This turnover occurs below PSFI threshold.
- Azimuthal flow shear stabilizes drift waves by weakening the ∇n_0 drive, i.e., reducing the ω_{*e} by the amount $|k_y \rho_s^2 \langle v_y \rangle''|$.
- Azimuthal flow shear slows down the modulational growth of seed axial flow shear, and thus reduces the production of intrinsic axial flow, absent magnetic shear.
- Azimuthal flow shear reduces both axial residual stress (Π_{xz}^{Res}) and turbulent viscosity driven by drift waves (χ_z^{DW}) by the same factor, i.e., both Π_{xz}^{Res} and χ_z^{DW} scale with the azimuthal flow shear as $|V'|^{-2} \sim |\langle v_y \rangle'|^{-2} \Delta_x^{-2} L_n^{-2} \rho_s^2 c_s^2$.
- Azimuthal flow shear does not affect the saturated axial flow shear to leading order, because $\langle v_z \rangle' = \Pi_{xz}^{Res}/\chi_z^{DW}$ and the reduction by $\langle v_y \rangle'$ cancels.

Results in this paper offer testable predictions for simulation studies on interaction of parallel and perpendicular flows. Here, we focus on the regime with straight magnetic fields. Hence, these results are relevant to linear devices and flat-q regions in tokamaks. In tokamaks, the combination of weak magnetic shear (i.e., flat q profile) and strong toroidal rotation are required for the formation of enhanced confinement states[MAC$^+$11a]. Thus, the turbulence energy apportionment between poloidal (i.e., zonal) and toroidal flows absent magnetic shear is of interest.

In the regime of intrinsic parallel flows, the feedback of parallel flow shear on the turbulence–flow system is weaker than that of perpendicular flow shear because $|k_\parallel V_\parallel'/k_\theta V_\theta'| \ll 1$. As a result, the turbulence is regulated primarily by V_θ', and parallel flow is parasitic. Non-parasitic parallel flow regime is achievable with external parallel momentum source. Of course, when the enhanced parallel flow shear hits the PSFI threshold, the resulting PSFI turbulence can drive zonal flow via strong acoustic coupling[WDH12b]. Even below the PSFI threshold, externally driven parallel flow shear can enhance the regulating effect of parallel flow on turbulence. When $|k_\parallel V_{\parallel,tot}'|$ is comparable to $|k_\theta V_\theta'|$, the parallel flow shear will have a strong effect on vorticity flux, mode structure, and fluctuation intensity. In both ways, the external parallel momentum source can enhance the interaction of parallel and perpendicular flows.

Chapter 4 is a reprint of the material as it appears in J. C. Li and P. H. Diamond, "Interaction of Turbulence-Generated Azimuthal and Axial Flows in CSDX", which is being prepared for publication. The dissertation author was the primary investigator and author of this article.

Chapter 5

Phenomenology of Parasitic Axial Flows Generated by Drift Wave Turbulence with Broken Symmetry

5.1 Introduction

Plasma flows along the magnetic field play a vital role in the stabilization of MHD instabilities and the development of transport barriers.[GSJ$^+$02, RICd$^+$07b, dRB$^+$07, DKG$^+$13b, IR14, Ric16] In most existing magnetic confinement fusion devices, the parallel flow, or toroidal plasma rotation, is driven directly by external momentum sources, such as neutral beam injection (NBI). However, in large scale devices like ITER, the NBI driven rotation will not be efficient, due to limited neutral beam penetration into high density plasmas. In order to optimize and improve the confinement regimes in ITER and beyond, it is important to uncover alternative mechanisms that can drive parallel flows.

A phenomenon called intrinsic flow has been identified in magnetically confined plasmas, [SBd$^+$07, dRB$^+$07, RHD$^+$11b, DKG$^+$13b, IR14, Ric16] where the plasma rotates without any input of toroidal momentum. This intrinsic flow can be of the same order of magnitude as that driven by some NBI torques. [RICd$^+$07b, SBd$^+$07, IR14, Ric16] Hence, there is strong interest in knowing whether intrinsic flow in future devices is sufficient to affect confinement and MHD stability. Empirical results show that intrinsic torque in H-mode plasmas scales with the plasma stored energy normalized by the plasma current ("Rice scaling").[RICd$^+$07b] Further measurements from Alcator C-Mod reveal that the intrinsic torque is proportional to the edge temperature gradient.[RHD$^+$11b] The production of intrinsic flow can be understood as a process similar to that of a heat engine. [RHD$^+$11b, KDG10b] In this process, temperature gradient, ∇T, excites turbulence, which not only relaxes ∇T but also drives a non-diffusive, residual stress via asymmetry in turbulence spectra $\langle k_z k_\theta \rangle$. [GDHS07b, DKG$^+$13b] This residual stress then drives the parallel flow, converting the free energy in ∇T into kinetic energy of macroscopic flow.

As proposed in this heat engine model, the parallel residual stress Π_{rz}^{Res} is the key element that connects radial inhomogeneity to the macroscopic intrinsic flow. It is a component of parallel Reynolds stress, and is not proportional to either flow or flow shear. [GDHS07b, DKG$^+$13b] The parallel Reynolds stress can then be written as [DKG$^+$13b]

$$\langle \tilde{v}_r \tilde{v}_z \rangle = -\chi_z \partial_r V_z + V_{\mathrm{p}} V_z + \Pi_{rz}^{\mathrm{Res}}.$$

The diffusive ($-\chi_z \partial_r V_z$) and pinch ($V_{\mathrm{p}} V_z$) terms are strict transport terms which cannot accelerate the plasma from rest. The divergence of this residual stress, $-\nabla \cdot \Pi_{rz}^{\mathrm{Res}}$, acts as a local momentum source that drives the intrinsic flow. The residual stress depends on properties of underlying turbulence, and may flip sign when there is a change in the driving radial gradients of the equilibrium profiles.

Evidence for the role of parallel residual stress in driving intrinsic flow has been accumulating. Probe measurements from the plasma boundary region of TJ-II stellarator confirm the existence of significant turbulent stress which provides a toroidal intrinsic torques.[GHP$^+$06]

A electrode biasing experiment on J-TEXT achieves a nearly zero toroidal rotation profile, and its results show that the intrinsic torque can be reasonably explained by the measured residual stress.[SCZ$^+$16] The residual stress profile has also been measured at edge of TEXTOR tokamak by canceling the toroidal rotation using counter-current NBI torque.[XHS$^+$13] The observations demonstrate that there is a minimum value for the $E_r \times B$ flow to trigger the residual stress, and that this stress scales with edge pressure gradient when the E_r shear threshold is exceeded. Parallel flow driven by turbulent Reynolds stress has also been observed in a linear device, PANTA.[IKK$^+$16, KIK$^+$16] Recently, a gyrokinetic simulation predicts that residual stress profile exhibits a dipolar structure and provides the intrinsic torque which is consistent with measured rotation profile in DIII-D.[WGE$^+$17]

A number of theoretical models based on symmetry breaking in **k**-space have been proposed to explain the development of the residual stress.[DKG$^+$13b] In these models, the residual stress is determined by the correlator, $\langle k_z k_\theta \rangle = \sum_{\mathbf{k}} k_z k_\theta \left|\hat{\phi}_{\mathbf{k}}\right|^2 / \sum_{\mathbf{k}} \left|\hat{\phi}_{\mathbf{k}}\right|^2$, which is effectively set by the spatial structure of the **k**-spectra $\left|\hat{\phi}_{\mathbf{k}}(r)\right|^2$. Theory suggests that the asymmetry in the k_z space can result from the spatial variation of fluctuation intensity profiles, [GDH$^+$10b] or from the sheared $E_r \times B$ flow that shifts modes off the resonant surfaces. [GDHS07b] These mechanisms indicate that the residual stress is related to $E_r \times B$ flow shear and turbulent intensity gradient, i.e., $\Pi_{rz}^{\mathrm{Res}} \sim V_E'$ and $\Pi_{rz}^{\mathrm{Res}} \sim I'$, respectively. These correlations are consistent with direct measurements from the edge of TEXTOR.[XHS$^+$13]

Despite these advances, our understanding of the microscopic mechanism is still rather limited. Until now, there is no direct evidence validating the connection between the requisite symmetry breaking mechanism and the development of residual stress. Moreover, it is also unclear whether the residual stress can efficiently convert the free energy stored in the radial inhomogeneity into kinetic energy of the macroscopic parallel flow.

Due to its turbulence-driven origin, the axial flow must necessarily be coupled to the azimuthal mean flow. The latter is also known as zonal flow and is generated by drift wave turbulence via a modulational instability. [DIIH05a] A theoretical framework[HDT] has been proposed to account for the interaction between these two secondary shear flows. However, how to precisely predict what the branching ratio between axial and azimuthal flows remains unknown. Therefore, further studies on how energy is distributed among the turbulence, azimuthal and axial mean flows are of interest. The dominant branch will have a larger turbulent drive and set the turbulence level through a predator-prey type interaction with turbulent intensity field.

Besides the branching ratio question, the axial and azimuthal flows might also interact with each other directly. For a coupled drift-ion acoustic waves system, a zonal flow can arise from the parallel flow compression due to the effects of acoustic coupling. [WDH12a] Specially, when the parallel flow shear is strong enough to trigger parallel shear flow instability (PSFI), the enhanced fluctuating parallel flow compression can act as a source for zonal flow. This mechanism of zonal flow generation differs from conventional models which depend on the potential vorticity (PV) flux, and has not been tested experimentally. On the other hand, the axial flow shear may also be affected directly by its azimuthal counterpart. In the presence of a finite magnetic shear, the $E_r \times B$ flow shear break parallel symmetry and generate a parallel residual stress Π_{rz}^{Res}, which accelerates the axial flow V_z. The effects of azimuthal flows on axial flow generation at zero magnetic shear also remains unclear.

In this study, we discuss axial and azimuthal flow dynamics in CSDX, with a special emphasis on the possible flow interactions discussed above. We begin with a summary of our expectations based upon current theory-based modeling. We then report an experiments in a linear device, the Controlled Shear Decorrelation eXperiment (CSDX).[BTA$^+$05, TBC$^+$14a] We show that the turbulent drive for the axial flow is less than that for the azimuthal flow by an order of magnitude. The turbulence fluctuation level is therefore regulated predominantly by the azimuthal flow shear. The results also show that the axial mean flow is driven by turbulent Reynolds stress. This stress, and particularly the non-diffusive, residual stress, results from density gradient drive. In agreement with the recently developed dynamical symmetry breaking mechanism,[LDXT16b] the residual stress emerges from drift wave turbulence with broken spectral symmetry. Note that this dynamical symmetry breaking model is also relevant to zero or weak magnetic shear case, e.g., in devices with straight magnetic fields and in flat-q regime tokamaks. The results presented in this paper validate the theoretical expectations for the link between the residual stress and symmetry breaking in the turbulence **k**-spectra, as well as the role of residual stress in converting thermodynamic free energy into kinetic energy of macroscopic axial flow.

The rest of the present paper is organized as follows. Section 5.2 recapitulates the theoretical background and predictions for turbulence-driven axial and azimuthal shear flows in CSDX. Section 5.3 introduces the experimental approach to measurements of mean flows and Reynolds stresses in CSDX. The experimental results and relevant discussions of theory-experiment comparisons are presented in Sections 5.4 to 5.6, respectively. Section 5.7 summaries the results and findings. In **??**, suggestions for future investigations are proposed.

5.2 Theoretical Predictions

In this section, we summarize theoretical predictions concerning the distribution of energy in the ecology of flows and fluctuations in CSDX. In order to investigate the evolution of turbulence and mean profiles in CSDX, we formulated a reduced model that describes the dynamics of the coupled drift-ion acoustic wave plasma. The model is derived from the Hasegawa-Wakatani system with axial flow evolution. [HDT] It self-consistently describes the variations in the mean profiles of density n, axial and azimuthal flows V_z and V_θ, as well as fluctuation energy

$\varepsilon = \langle \tilde{n}^2 + (\nabla\tilde{\phi})^2 + \tilde{v}_z^2 \rangle$. The mean field equations are

$$\frac{\partial n}{\partial t} = -\partial_r \langle \tilde{v}_r \tilde{n} \rangle + D_c \frac{\partial^2 n}{\partial r^2}, \tag{5.1}$$

$$\frac{\partial V_z}{\partial t} = -\partial_r \langle \tilde{v}_r \tilde{v}_z \rangle + \nu_{c,\parallel} \frac{\partial^2 V_z}{\partial r^2} - \nu_{in} V_z, \tag{5.2}$$

$$\frac{\partial V_\theta}{\partial t} = -\partial_r \langle \tilde{v}_r \tilde{v}_\theta \rangle + \nu_{c,\perp} \frac{\partial^2 V_\theta}{\partial r^2} - \nu_{in} V_\theta. \tag{5.3}$$

The quantities are normalized as follows: $t \equiv t'\omega_{ci}$, $v \equiv v'/c_s$, and $r \equiv r'/\rho_s$, where ω_{ci} is ion cyclotron frequency, c_s is the ion sound speed, and ρ_s is the ion Larmor radius at sound speed. The first terms on the RHS of Eqs. (5.1) to (5.3) represent the turbulent fluxes of particles and momentum, the terms that contain D_c, $\nu_{c,\perp}$ and $\nu_{c,\parallel}$ represent ion-ion collisional dissipations. In Eqs. (5.2) and (5.3), the terms proportional to the ion-neutral collision frequency ν_{in} represent momentum transfer between ions and neutrals, and are significant only in the boundary region. In this study, the Reynolds powers, $\mathcal{P}_z^{Re} = -V_z \partial_r \langle \tilde{v}_r \tilde{v}_z \rangle$ and $\mathcal{P}_\theta^{Re} = -V_\theta \partial_r \langle \tilde{v}_r \tilde{v}_\theta \rangle$, are used to represent the rate of work done by the fluctuations to the mean flows.

In addition to the mean field equations, the evolution of fluctuation intensity $\varepsilon = \langle \tilde{n}^2 + (\nabla\tilde{\phi})^2 + \tilde{v}_z^2 \rangle$ is obtained as

$$\frac{\partial \varepsilon}{\partial t} + \partial_r \Gamma_\varepsilon = -\langle \tilde{n}\tilde{v}_r \rangle \partial_r n - \langle \tilde{v}_r \tilde{v}_z \rangle \partial_r V_z - \langle \tilde{v}_r \tilde{v}_\theta \rangle \partial_r V_\theta - \frac{\varepsilon^{3/2}}{l_{mix}} + \mathcal{P}. \tag{5.4}$$

The first three terms on the RHS of the previous equation are mean field–fluctuation coupling terms. They relate variations in ε to the evolution of the mean fields of n, V_θ and V_z. The energy exchange between fluctuations and mean profiles occurs via the particle flux $\langle \tilde{n}\tilde{v}_r \rangle$, and the Reynolds stresses $\langle \tilde{v}_r \tilde{v}_\theta \rangle$ and $\langle \tilde{v}_r \tilde{v}_z \rangle$. In the energy equation, the $\varepsilon^{3/2}/l_{mix}$ term represents energy dissipation by inverse cascade at a rate $\sqrt{\varepsilon}/l_{mix}$. Dissipated energy is ultimately damped by frictional drag. An energy source term $\mathcal{P}$ represents the excitation of drift wave turbulence, which is linear in ε and proportional to γ_{DW}, i.e., $\mathcal{P} = \gamma_{DW}\varepsilon$. This is needed to incorporate turbulence excitation effects. On the LHS, a diffusive energy flux $\Gamma_\varepsilon = -D_\varepsilon \partial_r \varepsilon = -l_{mix}\sqrt{\varepsilon}\partial_r \varepsilon$ represents turbulence spreading. The flux Γ_ε can be traced back to the nonlinear convective terms in the initial Hasegawa-Wakatani system.

Since the density response in CSDX is weakly non-adiabatic, we then calculate turbulent fluxes using quasilinear theory. In the near adiabatic limit, the expression for the particle flux is given by[HDAT17]

$$\Gamma = \langle \tilde{n}\tilde{v}_r \rangle = -\frac{\nu_{ei}\langle \tilde{v}_r^2 \rangle}{k_z^2 v_{The}^2} \frac{k_\perp^2 \rho_s^2}{1 + k_\perp^2 \rho_s^2} \frac{dn}{dr} = -D\frac{dn}{dr}. \tag{5.5}$$

Here D is the particle diffusion coefficient, and is equal to:

$$D = \frac{k_\perp^2 \rho_s^2}{1 + k_\perp^2 \rho_s^2} \frac{\nu_{ei}\langle \tilde{v}_r^2 \rangle}{k_z^2 v_{The}^2} \simeq \frac{\nu_{ei}}{k_z^2 v_{The}^2}\varepsilon.$$

ν_{ei} and v_{The} are the electron-ion collision frequency and the electron thermal velocity, respectively.

In addition to the particle flux, an expression for the azimuthal momentum flux is needed. In the near adiabatic limit, and using quasi linear theory, the azimuthal momentum flux is equal to:

$$\langle \tilde{v}_r \tilde{v}_\theta \rangle = -\chi_\theta \partial_r V_\theta + \Pi_{r\theta}^{\mathrm{Res}}. \tag{5.6}$$

The first term is the diffusive flux, while the second term is the residual component that accelerates the zonal flow from rest. The pinch term that arises from toroidal effects is neglected for the cylindrical geometry of the experiment. The turbulent viscosity and the residual stress are given as [HDT]

$$\begin{aligned} \chi_\theta &= \frac{|\gamma|\langle \tilde{v}_r^2 \rangle}{|\omega|^2} = \tau_c \langle \tilde{v}_r^2 \rangle = l_{mix}\sqrt{\varepsilon}, \\ \Pi_{r\theta}^{\mathrm{Res}} &= -\frac{|\gamma|\omega_* \langle \tilde{v}_r^2 \rangle}{|\omega|^2} = -\frac{\langle \tilde{v}_r^2 \rangle \tau_c c_s}{\rho_s L_n} = -\frac{l_{mix}\sqrt{\varepsilon}\omega_{ci}}{L_n}. \end{aligned} \tag{5.7}$$

In this study, the $E_r \times B$ flow shearing rate is less than turbulence frequency, i.e., $V_E' \ll \omega$, so the term $\Im\frac{1}{\omega-kV_E'x+i\gamma}$ reduces to $\frac{|\gamma|}{|\omega|^2}$. The azimuthal residual stress and χ_θ thus decouple from azimuthal flow shear.

The axial Reynolds stress is given as [HDT]

$$\langle\tilde{v}_r\tilde{v}_z\rangle = -\frac{|\gamma|\langle\tilde{v}_r^2\rangle}{|\omega|^2}\frac{\partial V_z}{\partial r} + \langle k_\theta k_z\rangle\rho_s c_s^3\left[\frac{|\gamma|}{|\omega|^2} + \frac{\nu_{ei}(\omega_{*e}-\omega^r)}{|\omega|k_z^2 v_{The}^2}\right]. \tag{5.8}$$

The non-diffusive component, i.e, the residual stress Π_{rz}^{Res}, drives the intrinsic axial flow, and is proportional to the correlator $\langle k_\theta k_z\rangle$. We thus write the following expressions for the parallel turbulent diffusivity χ_z, and Π_{rz}^{Res}:

$$\begin{aligned}\chi_z &= \frac{|\gamma|\langle\tilde{v}_r^2\rangle}{|\omega|^2} = \tau_c\langle\tilde{v}_r^2\rangle = l_{mix}\sqrt{\varepsilon},\\ \Pi_{rz}^{\text{Res}} &= \langle k_\theta k_z\rangle\rho_s c_s^3\left[\tau_c + \frac{\nu_{ei}\rho_s^2 k_\perp^2}{k_z^2 v_{The}^2}\right] = \langle k_\theta k_z\rangle\rho_s c_s^3\left[\frac{l_{mix}}{\sqrt{\varepsilon}} + \frac{\nu_{ei}\rho_s^2 k_\perp^2}{k_z^2 v_{The}^2}\right].\end{aligned} \tag{5.9}$$

Note that in order to obtain Π_{rz}^{Res}, we used the expressions for both electron drift frequency ω_{*e} and eigenfrequency $\omega^r = \omega_{*e}/(1+k_\perp^2\rho_s^2)$ in the adiabatic limit. Here, the axial residual stress and χ_z also decouple from V_E', since $E_r \times B$ flow shearing rate is much less than drift wave turbulence frequency in CSDX.

Π_{rz}^{Res} contains an expression for $\langle k_\theta k_z\rangle$, which is not easily determined within the scope of this simple, reduced model. To calculate the correlator, we need a spectral model considering the evolution of $\langle k_\theta k_z\varepsilon\rangle$, which can be obtained from wave momentum equations. This is beyond the scope of this work. Thus, what we offer here is an empirical approach that relates free energy source, ∇n, to the axial flow shear $\partial_r V_z$. The correlator $\langle k_\theta k_z\rangle$ is then expressed in terms of a coefficient that can be used in numerical studies, which is determined as follows. Proceeding in analogy with the treatment of turbulence in pipe flow, the evolution of the fluctuation parallel ion flow is written as

$$\frac{d\tilde{v}_z}{dt} = -c_s^2\nabla_z\left[\frac{e\tilde{\phi}}{T} + \frac{\tilde{P}}{P_0}\right] - \tilde{v}_r\frac{\partial V_z}{\partial r},$$

where c_s denotes the sound speed, $\tilde{v}_r$ is the eddy radial velocity, $\tilde{P}$ is the pressure fluctuation, and $\tilde{\phi}$ is the potential fluctuation. In a drift wave system with adiabatic electrons like CSDX, one has $e\tilde{\phi}/T \sim \tilde{n}/n_0$ and $\tilde{P}/P_0 \sim \tilde{n}/n_0$ as temperature fluctuations are small in this experiment. By introducing the radial mixing length l_{mix} by the familiar relation $\tilde{n}/n_0 \sim l_{mix}|\nabla n|/n_0$, the fluctuating parallel flow then can be written as

$$\tilde{v}_z \approx -\sigma_{vT}\frac{c_s^2 l_{mix}^2}{L_z\tilde{v}_r}\frac{|\nabla n|}{n_0} - l_{mix}\frac{\partial V_z}{\partial r}.$$

Here L_z is the characteristic parallel dimension. The constant σ_{vT} is introduced as a dimensionless scaling between $\tilde{v}_z$ and the density gradient ∇n. Multiplying by $\tilde{v}_r$ and ensemble averaging, the parallel Reynolds stress then becomes:

$$\langle \tilde{v}_r\tilde{v}_z\rangle = -\chi_z\frac{\partial V_z}{\partial r} - \sigma_{vT}\frac{c_s^2\langle l_{mix}^2\rangle}{L_z}\frac{|\nabla n|}{n_0}$$

While the first term represents a diagonal diffusive turbulent viscosity with $\chi_z \sim \langle \tilde{v}_r^2\rangle\tau_c \sim l_{mix}\sqrt{\varepsilon}$, the remaining part is the residual stress Π_{rz}^{Res}, proportional to ∇n. The coefficient σ_{vT} is written as

$$\sigma_{vT} = \frac{\langle k_\theta k_z\rangle}{\langle k_\perp^2\rangle^{1/2}/L_\parallel}.$$

This coefficient captures the cross phase relation between $\tilde{v}_r$ and $\tilde{v}_z$, and calibrates the efficiency of the density gradient in driving the residual stress Π_{rz}^{Res}. σ_{vT} is also a measure of asymmetry in the spectral correlator $\langle k_\theta k_z\rangle = \sum_{\mathbf{k}} k_z k_\theta \left|\hat{\phi}_{\mathbf{k}}\right|^2 / \sum_{\mathbf{k}} \left|\hat{\phi}_{\mathbf{k}}\right|^2$, and encodes information concerning the parallel symmetry breaking that creates the residual parallel stress. An empirical value for σ_{vT}, which can be used in the numerical solution of this model, can be obtained by a least-square fit to the experimental results.

Most of the conventional symmetry breaking mechanisms [DKG$^+$13b, GDH$^+$10b] are not applicable to plasmas with weak or zero magnetic shear, since they are usually associated with finite magnetic shears. To resolve this issue, a dynamical symmetry breaking mechanism has been proposed to explain the development of intrinsic axial flow in absence of magnetic shear. [LDXT16b] This mechanism does not require a specific magnetic field configuration, and thus it is valid for both finite shear and zero shear regimes. This mechanism is effectively equivalent to the modulational growth of a seed axial flow shear, as in zonal flow generation. In both cases, the initial breaking of symmetry is due to the seed flow.

The dynamical symmetry breaking model [LDXT16b] was derived from a drift wave system with evolution of axial flow. The axial mean flow introduces a frequency shift to the growth rate of drift wave, i.e.,

$$\gamma_k \cong \frac{\nu_{ei}\omega_{*e}}{k_z^2 v_{\mathrm{The}}^2} \frac{\omega_{*e} - \omega_k}{(1 + k_\perp^2 \rho_\mathrm{s}^2)^2}. \tag{5.10}$$

The adiabaticity of the electron response is measured by the dimensionless factor $\alpha \equiv k_z^2 v_{The}^2 / \nu_{ei}\omega_{*e}$, where $\omega_{*e} \equiv k_\theta \rho_s c_s / L_n$ is the electron drift frequency. As electrons approach the adiabatic limit, i.e., $\alpha \to \infty$, drift wave is stabilized yielding $\gamma_k \to 0$. In CSDX, electrons are weakly non-adiabatic with $\alpha \sim 1$.

A test axial flow shear $\delta V_z'$, i.e., a perturbation to the mean axial flow profile, can break the symmetry of drift wave turbulence through the frequency shift. The frequency of drift wave is affected by the test flow shear, which is

$$\omega_k \cong \frac{\omega_{*e}}{1 + k_\perp^2 \rho_\mathrm{s}^2} - \frac{k_\theta k_z \rho_\mathrm{s} c_\mathrm{s} \delta V_z'}{\omega_{*e}}. \tag{5.11}$$

The test flow shear modifies the drift wave growth rate, i.e.,

$$\gamma_k \cong \frac{\nu_\mathrm{ei}}{k_z^2 v_\mathrm{The}^2} \frac{\omega_{*e}^2}{(1 + k_\perp^2 \rho_\mathrm{s}^2)^2} \left(\frac{k_\perp^2 \rho_\mathrm{s}^2}{1 + k_\perp^2 \rho_\mathrm{s}^2} + \frac{k_\theta k_z \rho_\mathrm{s} c_\mathrm{s} \delta V_z'}{\omega_{*e}^2} \right). \tag{5.12}$$

For a given $\delta V_z'$, the drift wave modes with $k_\theta k_z \rho_\mathrm{s} c_\mathrm{s} \delta V_z' > 0$ have a larger frequency shift than the other modes. Thus, these modes grow faster. As a result, a spectral imbalance in the $k_z - k_\theta$

spectra is induced by the test flow shear. Such asymmetry in turbulence spectra can be detected by a joint probability density function of the turbulent velocities in both axial and azimuthal direction. The measurements of spectral imbalance are reported and linked to finite residual stress in this work.

The residual stress set by this dynamical symmetry breaking mechanism provides a negative definite contribution to the total turbulent diffusivity of axial momentum flux, i.e., $\Pi_{r,z}^{\mathrm{Res}} = -\chi_z^{\mathrm{Res}} \delta V_z'$ where $\chi_z^{\mathrm{Res}} < 0$. The negative momentum diffusivity induced by residual stress is

$$\chi_z^{\mathrm{Res}} = -\frac{\nu_{ei} L_n^2}{v_{\mathrm{The}}^2} \sum_k (1 + k_\perp^2 \rho_s^2)(4 + k_\perp^2 \rho_s^2) |\phi_k|^2. \tag{5.13}$$

Thus, the total Reynolds stress is

$$\Pi_{r,z} = -\left(\chi_z - \left|\chi_z^{\mathrm{Res}}\right|\right) V_z'. \tag{5.14}$$

This process of self-amplification of test flow shear suggests that intrinsic axial flow is generated through a modulational instability. When the magnitude of the negative viscosity exceeds the turbulent viscosity driven by drift wave, the total Reynolds stress induces a negative diffusion of axial momentum, thus amplifying the perturbation. In this case, the test shear (i.e., the modulation of mean flow shear profile) becomes unstable. The growth rate of test flow shear is $\gamma_q = q_r^2 \left(\left|\chi_z^{\mathrm{Res}}\right| - \chi_z\right)$, where q_r is the radial mode number of flow shear modulation.

The onset threshold of axial flow generation is determined by the balance between residual stress and the turbulent diffusion driven by drift waves. Hence, the $\nabla n / n_0$ threshold can be obtained from $\left|\chi_z^{\mathrm{Res}}\right| = \chi_z$. The turbulent viscosity driven by drift wave turbulence is calculated using

$$\chi_z \sim \frac{\langle l_c^2 \rangle}{\tau_c}, \tag{5.15}$$

where l_c is the eddy correlation length and τ_c is the eddy correlation time. The critical density gradient is then

$$\nabla n_{\text{crit}} \sim n_0 \alpha \frac{\omega_{*e}^2}{\langle k_\theta k_z \rangle \rho_s c_s} \frac{L_z}{c_s^2 \tau_c}. \tag{5.16}$$

Plugging in parameters measured on CSDX, we can obtain $\nabla n_{\text{crit}} \sim 1.5 \times 10^{20}\,\text{m}^{-4}$, which agrees with the experimental measurements presented below. Here, $\alpha = k_z^2 v_{\text{The}}^2 / \omega_{*e} \nu_{ei} \sim 1$ is the adiabaticity factor, the perpendicular turbulence scale length is $k_\theta \rho_s \sim 1.5$, and the eddy correlation time is $\tau_c \sim 6 \times 10^{-5}\,\text{s}$.

The density gradient threshold can also be obtained by using the scaling coefficient σ_{vT} of residual stress. The residual stress scales with ∇n as $\Pi_{r,z}^{\text{Res}} \sim \sigma_{vT} \langle l_c^2 \rangle c_s^2 / (L_n L_z)$. Thus, σ_{vT} is determined by the correlator $\langle k_\theta k_z \rangle$, i.e., $\sigma_{vT} = \langle k_\theta k_z \rangle / \langle k_\theta^2 \rangle$. Considering the symmetry breaking set by a test flow shear, we can calculate the correlator and thus the coefficient, as

$$\sigma_{vT} = \frac{1}{\alpha} \frac{\langle k_\theta k_z \rangle \rho_s c_s \delta V_z'}{\omega_{*e}^2}. \tag{5.17}$$

Thus, by using the balance between residual stress and turbulent diffusion, i.e., $\Pi_{r,z}^{\text{Res}} = \chi_z \delta V_z'$, we can also obtain the critical density gradient for onset of axial flow generation, which is the same as Eq. (5.16).

Though the theory explains how axial flows are generated in the linear stage, the nonlinear evolution of the axial flow is not captured. Further, how axial flows saturate remains an open-ended question. The axial flow can saturate due to the balance between residual stress and turbulent diffusion, as $\chi_z V_z' = \Pi_{r,z}^{\text{Res}}$. The theory presented here focuses on the stage where the test flow shear is small, such that the leading order of the residual stress is $\delta \Pi_{r,z}^{\text{Res}} \sim |\chi_z^{\text{Res}}| \delta V_z'$. Thus, the axial flow saturates when $\chi_z = |\chi_z^{\text{Res}}|$. Ultimately, the flow energy is dissipated by viscous heating and drag dissipation.

In summary, for regimes of moderate azimuthal shear (i.e., $|V_\theta'| \ll \omega_k$), theory predicts that:

(1) drift wave fluctuations and azimuthal (i.e., zonal) flows will form a self-regulating system;

(2) axial flows will evolve parasitically by Reynolds stress, on the existing drift wave–zonal flow turbulence. Here, the key point is $\Pi_{r,\theta}^{\mathrm{Res}} \gg \Pi_{r,z}^{\mathrm{Res}}$, as $k_{\perp} \gg k_z$;

(3) symmetry breaking in the k_θ–k_z space is required for axial flow generation.

(4) Sheared intrinsic axial flows will be generated when the density gradient exceeds a predicted critical value.

Now, we turn to tests of these predictions.

5.3 Experimental Setup

In this section, we present the experimental methodology for testing the predictions of model in Section 5.2. The experiments were conducted on the Controlled Shear Decorrelation eXperiment (CSDX), a linear plasma device with an overall length of 2.8 m and a diameter of 0.2 m (Fig. 5.1). The working gas was argon at a gas fill pressure of 2 mTorr. The argon plasma was produced by a 15 cm diameter 13.56 MHz RF helicon wave source via an $m = 1$ helical antenna that surrounds a glass bell-jar, and was terminated by insulating end-plates at both ends. The uniform magnetic field is in the axial direction (denoted as the $-\hat{z}$ direction). In this study 1800W of power was used, and the magnetic field strength was varied from 500 G to 1000 G. A higher magnetic field results in a steepening of the density profile in CSDX.[BTA^{+}05, TBC^{+}14a] Typical plasma parameters are as follows: the peak on-axis electron density of $n_e \sim 1 \times 10^{19}\mathrm{m}^{-3}$, the electron temperature of $T_e \sim 3-5$ eV, and the ion temperature of $T_i \sim 0.3-0.8$ eV. More details on this device can be found in previous publications.[BTA^{+}05, TBC^{+}14a, TGM^{+}16]

A horizontal scanning probe was used to record basic plasma information such as ion saturation currents and floating potentials at port α that is about 1 m downstream from the helicon source. The probe array is a combination of Mach and Langmuir probes and is capable of

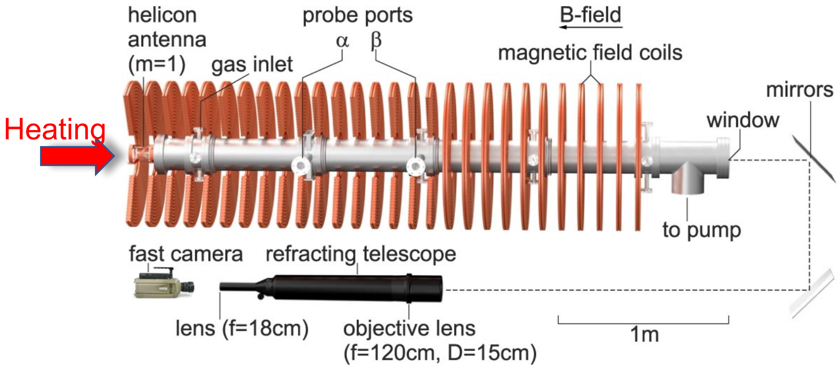

Figure 5.1: Schematic of CSDX with probe and fast imaging diagnostics.

measuring the axial and radial plasma velocities simultaneously (Fig. 5.2). The axial velocity, v_z, was measured by a Mach probe which has two tips aligned along the axial direction and separated by insulators. The axial velocity, according to the fluid model of ion collection by absorbing objects in combined parallel and perpendicular flows, [Hut08, PH09] can be given by $v_z = Mc_s = 0.45 c_s \ln\left(\frac{J_\mathrm{u}}{J_\mathrm{d}}\right)$, where $c_s = \sqrt{T_e/m_i}$ is the sound speed and $J_{\mathrm{u,d}}$ are the ion saturation fluxes collected by two Mach probe tips at the up- and down-stream side. We were careful to use small enough tips to avoid probe shadowing effects that can give spurious axial flow measurements, and verified that the mean flow profile measured by the Mach probe agreed with laser-induced flourescence measurements of the same ion flow. The fluctuating $\mathbf{E} \times \mathbf{B}$ velocities are estimated from the floating potential gradients between two adjacent tips ($\nabla\tilde{\phi}_\mathrm{f}$), i.e., $\tilde{v}_r = -\nabla_\theta\tilde{\phi}_\mathrm{f}/B$ and $\tilde{v}_\theta = \nabla_r\tilde{\phi}_\mathrm{f}/B$. The distance between two adjacent floating potential tips is about 3 mm. The sampling rate of the probe data is $f_s = 500$ kHz which is well above the frequency of the observed dominant fluctuations ($f < 30$ kHz) in our experiments. [TBC$^+$14a] With this probe configuration, the axial Reynolds stress $\langle\tilde{v}_z\tilde{v}_r\rangle$ and the azimuthal Reynolds stress $\langle\tilde{v}_\theta\tilde{v}_r\rangle$ can be measured simultaneously. Similar probe configurations have also been employed in other investigations on the structures of parallel ion flows. [IKK$^+$16, KIK$^+$16]

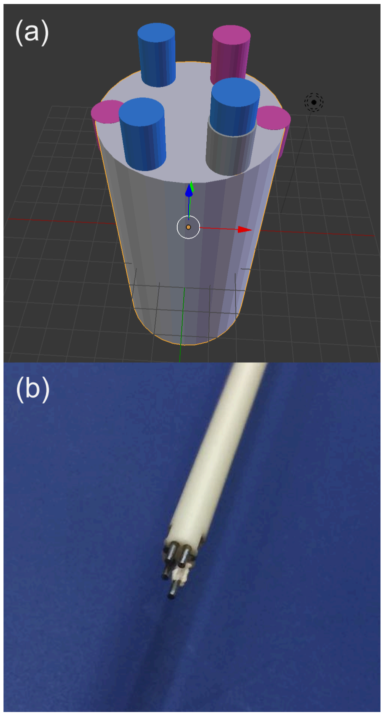

Figure 5.2: (a) Schematic of the 6-tip probe array. Pink tips are negatively biased to measure the ion saturation currents; blue tips measure the floating potentials. (b) Photo of the 6-tip probe array.

5.4 Results: Evolution of Profiles

5.4.1 Enhanced Shear Flows

In this study, we obtained different equilibrium profiles and fluctuation intensities by changing the magnetic field strength B. As shown in Fig. 5.3(a), when the B field is raised, the plasma density and its radial gradient increases. During the B scan, the variation in electron temperature is negligible. The axial velocity reverses at edge, and its radial shear increases with increasing B field (Fig. 5.3(b)). The axial Reynolds stress, $\langle \tilde{v}_z \tilde{v}_r \rangle$ (Fig. 5.3(c)), is estimated using velocity fluctuations in the frequency range of $2 < f < 30$ kHz; previous studies have identified these as collisional drift wave fluctuations.[BTA$^+$05, TBC$^+$14a] $\langle \tilde{v}_z \tilde{v}_r \rangle$ is negligible for $r < 3$ cm at lower B field, but becomes substantially negative at higher B field (Fig. 5.3(c)). The Reynolds force, $\mathcal{F}_z^{Re} = -\partial_r \langle \tilde{v}_z \tilde{v}_r \rangle$ (Fig. 5.3(d)), increases significantly in the core, and becomes more negative at the edge ($3 < r < 6$ cm). This negative turbulent force at the edge appears to be matched with the reversed axial mean flow. The parallel Reynolds force is about 5 times larger than the force on the ions arising from the parallel electric field. This weak electric field arises from the Boltzmann equilibrium associated with the electron pressure drop along the axial direction (Fig. 5.3(e)). Thus, the axial shear flow in CSDX reported here is primarily driven by the turbulent Reynolds force.

In addition to the evolution of the axial flow, the changes in azimuthal flow has also been measured simultaneously during the B scan. As can be seen from Fig. 5.4(a), the mean azimuthal velocity, V_θ, propagates in the electron diamagnetic drift direction (EDD), which is negative in the figure. The magnitude of V_θ increases by a factor of two when B is raised from 500 G to 800 G. The azimuthal Reynolds stress, $\langle \tilde{v}_r \tilde{v}_\theta \rangle$, is also estimated using fluctuations in the frequency range of $2 < f < 30$ kHz. $\langle \tilde{v}_r \tilde{v}_\theta \rangle$ is small and flat at lower B, but its magnitude increases when B is increased (Fig. 5.4(b)). The change in $\langle \tilde{v}_r \tilde{v}_\theta \rangle$ gives rise to substantial turbulent Reynolds force, $\mathcal{F}_\theta^{Re} = -\partial_r \langle \tilde{v}_r \tilde{v}_\theta \rangle$ (Fig. 5.4(c)) at higher B. This turbulent force acts to reinforce the azimuthal

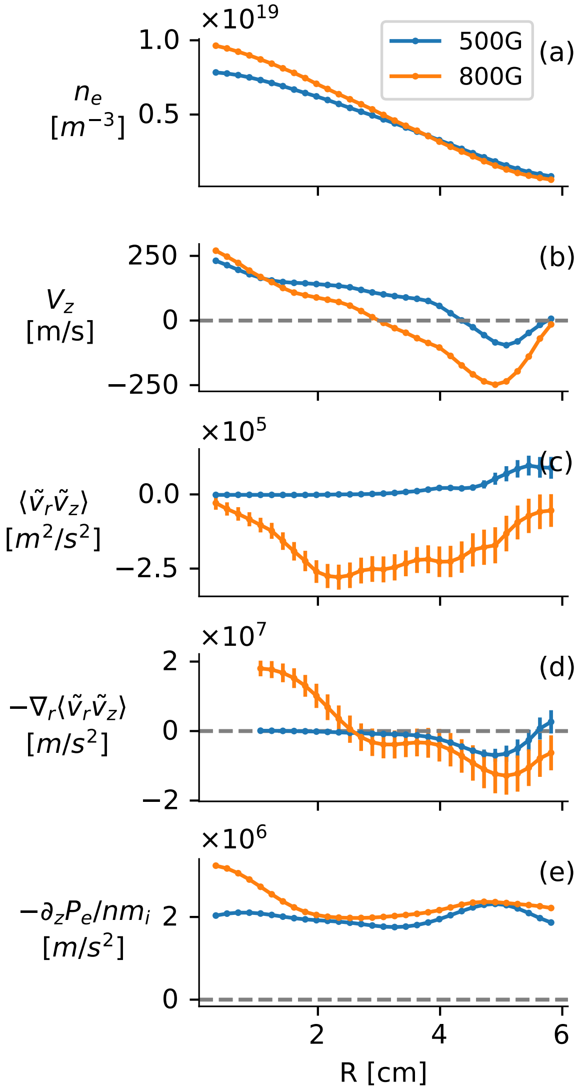

Figure 5.3: Equilibrium profiles of (a) the plasma density, (b) the axial mean flow, (c) the axial Reynolds stress, (d) the axial Reynolds force, and (d) the axial force arises from electron pressure drop.

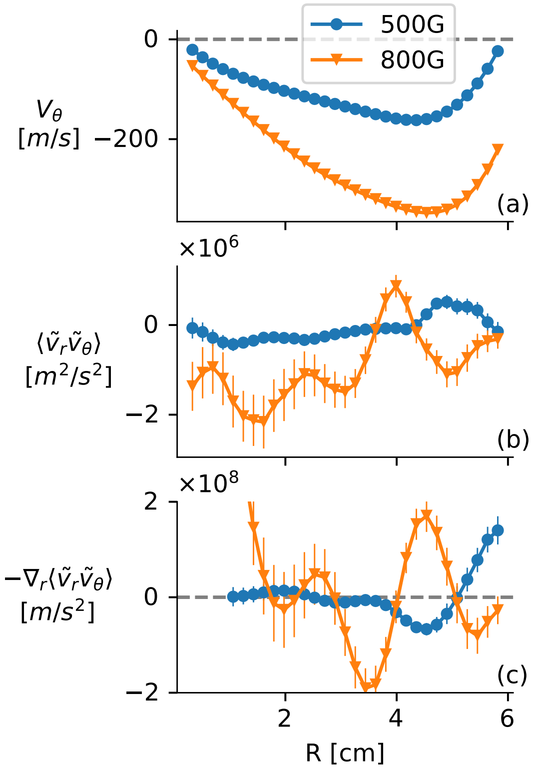

Figure 5.4: Radial profiles of (a) mean azimuthal velocity, (b) azimuthal Reynolds stress $\langle \tilde{v}_r \tilde{v}_\theta \rangle$, and (c) azimuthal Reynolds force $\mathcal{F}_\theta^{Re} = -\partial_r \langle \tilde{v}_r \tilde{v}_\theta \rangle$.

flow shear at the edge ($r \approx 4$ cm). These observations indicate that the azimuthal mean flow, similar to the axial mean flow, increases due to its enhanced turbulent drive. The turbulence-driven azimuthal flow has been reported from previous studies in CSDX.[HYJ$^+$06, YXD$^+$10b, XTD$^+$11b] These recent observations here are consistent with earlier results.

5.4.2 Axial Force Balance Analysis

To confirm the role of Reynolds force in driving the axial flow, we also examined the force balance in axial direction. The azimuthal force balance has been performed in previous studies.[HYJ$^+$06] It confirms that the azimuthal mean flow can be reproduced with azimuthal Reynolds force and collisional damping effects. Here, we carry out similar analysis on the axial flow. The axial ion momentum equation is written as

$$\frac{1}{r}\frac{\partial}{\partial r}\left(r\langle\tilde{v}_z\tilde{v}_r\rangle\right)=-\frac{1}{m_i\langle n\rangle}\frac{\partial P_e}{\partial z}-\nu_{in}V_z+\frac{1}{r}\frac{\partial}{\partial r}\left(\mu_{ii}r\frac{\partial V_z}{\partial r}\right), \tag{5.18}$$

where the ion viscosity $\mu_{ii}=\frac{6}{5}\rho_i^2\nu_{ii}\sim 3-5\,\mathrm{m}^2/\mathrm{s}$ and ion-neutral collision frequency $\nu_{in}=n_{\mathrm{gas}}v_{ti}\sigma_{in}\sim 3-6\times 10^3\,\mathrm{s}^{-1}$ are estimated from previous studies. [HYJ$^+$06] μ_{ii} and ν_{in} are likely to have weak spatial variations, i.e., $\mu_{ii}\propto nT_i^{-1/2}$ and $\nu_{in}\propto T_i^{-1/2}$. Here, we assume the neutral pressure is radially uniform and the neutral temperature is approximated by the ion temperature profile, which has been measured using LIF techniques in previous studies. [TGM$^+$16] A no-slip boundary condition is also imposed, justified by strong ion-neutral damping at edge, i.e., $V_z\rightarrow 0$ at $r=6$ cm. Taking the measured profiles of the Reynolds stress and the axial pressure gradient shown in Fig. 5.3, we can then solve Eq. (5.18) for V_z using a finite difference method. The axial pressure force can also be ignored at higher B field, since it is smaller than turbulence force by a factor of 5. As shown in Fig. 5.5, the calculated results (curves) are in agreement with the mean axial ion flow profiles measured by the Mach probe (circles). This results confirms that the turbulent stress is responsible for the increased V_z' and flow reversal found at higher magnetic field.

5.5 Results: Density Gradient Scalings

5.5.1 Turbulent Drive Scales with Density Gradient

The magnetic field scan yields a clear rise in ∇n, which is much larger than ∇T_e and has been identified in previous work as the primary free energy source driving the fluctuations. [BTA$^+$05, TBC$^+$14a] This change presents us an opportunity to determine the link between ∇n, the turbulent drive, and the macroscopic intrinsic flow. In this study, we did a shot-by-shot B field scan, and used the Reynolds power, $\mathcal{P}_z^{Re}=-\langle V_z\rangle\partial_r\langle\tilde{v}_z\tilde{v}_r\rangle$, to represent the rate

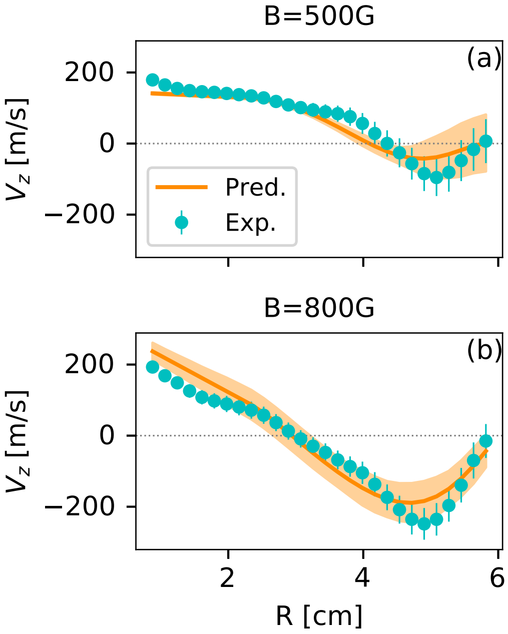

Figure 5.5: Radial profiles of mean axial velocity predicted by force balance with $\mathcal{F}_z^{Re} \gg -\frac{\partial_z P_e}{m_i n}$ (solid line) and measured Mach probe (circles) at 500 G (a) and 800 G (b). Shaded area indicates the uncertainties of predicted V_z profile.

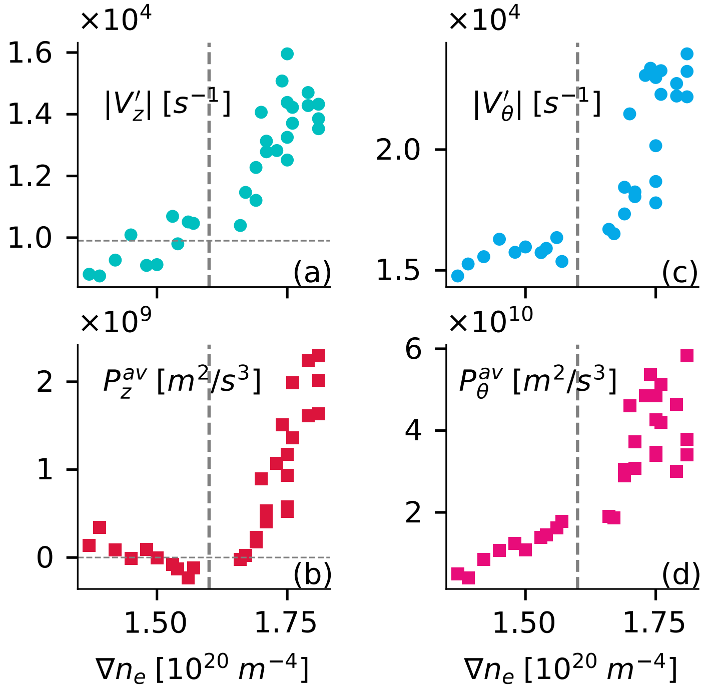

Figure 5.6: The magnitude of axial flow shearing rate $|\partial_r V_z|$ (a), the volume-averaged axial Reynolds power $\mathcal{P}_z^{av}$ (b), azimuthal flow shear $|\partial_r V_\theta|$ (c), and azimuthal Reynolds power $\mathcal{P}_\theta^{Re}$ (d) are plotted against the density gradient ∇n_e.

of work performed by the turbulent fluctuations on the mean axial flow. The axial shear flow and the Reynolds power are plotted as a function of ∇n (Fig. 5.6). The magnitude of axial flow shearing rate, $|V_z'| = |\partial_r V_z|$, increases sharply when the density gradient exceeds a critical value, $\nabla n_e \gtrsim 1.6 \times 10^{20}\,\mathrm{m}^{-4}$ (Fig. 5.6(a)). This critical density gradient is in agreement with the theoretical prediction shown in Eq. (5.16). Concurrently, the Reynolds power also increases substantially when this threshold is exceeded (Fig. 5.6(b)). Here, we used volumed-averaged Reynolds power, $\mathcal{P}_z^{av} = \int -\langle V_z \rangle \partial_r \langle \tilde{v}_z \tilde{v}_r \rangle\, rdr / \int rdr$ where $1 < r < 5$ cm. These observations show that the axial shear flow and its Reynolds power increase consistently as ∇n increases, indicating that the turbulence acts as a converter, transferring the free energy to the intrinsic flow. These results are consistent with the heat engine model. [KDG10b] Here, the free energy due to ∇n is converted into kinetic energy of macroscopic parallel flow.

The azimuthal flow and its turbulent drive are also driven by the density gradient. Similar to the analysis of the axial flow case, we use the azimuthal Reynolds power, $\mathcal{P}_\theta^{Re} = -\langle V_\theta \rangle \partial_r \langle \tilde{v}_r \tilde{v}_\theta \rangle$, to represent the nonlinear kinetic energy transfer into the mean azimuthal flow. We then plot the axial flow shear and azimuthal Reynolds power as a function of the density gradient. As shown in Fig. 5.6(c), there is a clear threshold effect in the density gradient, which is the same as the axial flow case. After the threshold, the azimuthal flow shear, $\left|V_\theta'\right| = |\partial_r V_\theta - V_\theta/r|$, and the azimuthal Reynolds power, $\mathcal{P}_\theta^{Re}$, increase with the density gradient ∇n (Fig. 5.6(d)). The similar trends of V_θ' and $\mathcal{P}_\theta^{Re}$ suggest that the underlying turbulence also converts the free energy from the density gradient into kinetic energy of azimuthal mean flow.

The results above show that both the axial and azimuthal mean flows are turbulence-driven in CSDX. However, the nonlinear kinetic energy transfer to the two secondary shear flows are not equally distributed. The axial Reynolds power is smaller than the azimuthal one by an order of magnitude, i.e., $\mathcal{P}_z^{Re} \ll \mathcal{P}_\theta^{Re}$, since $k_z \ll k_\perp$ for turbulent fluctuations in CSDX. Therefore, we conclude that the azimuthal shear flow sets the turbulent fluctuation level through predator-prey type interaction, while the axial flow evolves in this intensity field. The disparate magnitudes of nonlinear energy transfer also suggest that there is no significant direct energy exchange between axial and azimuthal shear flows. The axial flow is then parasitic to the turbulence-zonal flow system, and is driven by the turbulent Reynolds stress, especially the non-diffusive, residual stress. The weak axial to azimuthal flow coupling allows us then to simplify the 4-field model in Section 5.2 to a 2-field predator-prey model.

5.5.2 Residual Stress Driven by Density Gradient

As discussed in Section 5.2, it is the residual stress that converts the thermodynamic free energy to the kinetic energy of the axial mean flow.[DKG$^+$13b, LDXT16b] The residual stress can be synthesized from the measured Reynolds stress (Fig. 5.3(c)) and the diffusive stress inferred from experimental measurements,[YXD$^+$10b] i.e., $\Pi_{rz}^{\mathrm{Res}} = \langle \tilde{v}_r \tilde{v}_z \rangle + \chi_z \partial_r V_z$ with the diffu-

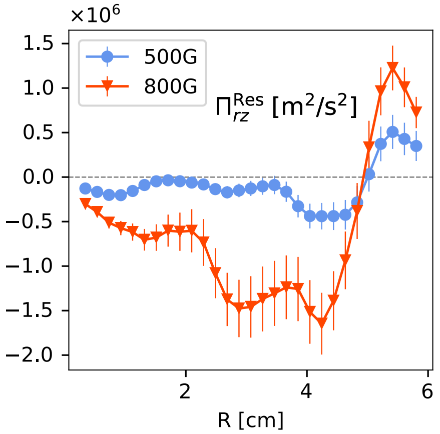

Figure 5.7: Radial profiles of the synthesized residual stress at different magnetic fields.

sivity $\chi_z = \langle \tilde{v}_r^2 \rangle \tau_c$ expressed in terms of the measured eddy radial velocity $\tilde{v}_r$ and eddy correlation time. Here, the pinch term $(V_{\mathrm{p}} V_z)$ is ignored, since it arises from toroidal effects and thus is not significant in a linear device. As shown in Fig. 5.7, the magnitude of the synthesized residual stress increases as the B field, as well as ∇n, is increased.

The magnitude of the residual stress, Π_{rz}^{Res}, is then plotted against the normalized density gradient in Fig. 5.8. At smaller density gradient, the magnitude of residual stress, $\left|\Pi_{rz}^{\mathrm{Res}}\right|$, is small, and is almost independent of the normalized density gradient. At larger ∇n, $\left|\Pi_{rz}^{\mathrm{Res}}\right|$ increases in proportion to the normalized density gradient, with a slope $\sigma_{vT} \approx 0.10$. Here, $\left|\Pi_{rz}^{\mathrm{Res}}\right|$ is volume-averaged in the range of $1 < r < 5$ cm. This finding confirms the hypothesis that the residual stress is driven by the density gradient. Also, a finite $\sigma_{vT} \approx 0.1$ indicates a symmetry breaking mechanism at higher ∇n.

5.5.3 Effect of Azimuthal Flow Shear on Residual stress

The above observations have demonstrated the coexistence of turbulence-driven shear flows in both axial and azimuthal directions. It is also shown that the azimuthal Reynolds power is much larger than its axial counterpart. Therefore, the azimuthal flow primarily determines

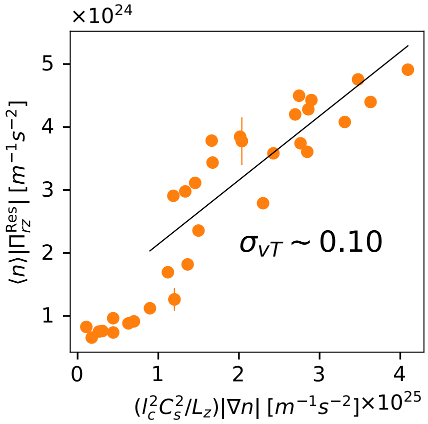

Figure 5.8: Comparison between magnitudes of residual stress and normalized density gradient. The coefficient, σ_{vT}, is estimated to be about 0.10 by a least-square fit using data with higher ∇n.

the turbulence intensity via a predator-prey type interaction, and axial flows are parasitic on this system. As shown in Fig. 5.9, the axial flow shear V_z' and the magnitude of the residual stress $\left|\Pi_{rz}^{\mathrm{Res}}\right|$ are plotted against the azimuthal flow shear. As azimuthal flow shear is entangled with ∇n during the B scan, V_z' (Fig. 5.9(a)) and $\left|\Pi_{rz}^{\mathrm{Res}}\right|$ increases (Fig. 5.9(b)) with V_θ'. Since in present experiments the azimuthal flow shear is less than the frequency of drift wave turbulence, i.e., $V_E' \ll \omega$, the axial residual stress does not depend explicitly on the azimuthal shear flow.

5.6 Results: Residual Stress Restuls from Symmetry Breaking in Turbulence Spectra

The development of residual stress is also proposed to be correlated with symmetry breaking in **k**-space, [DKG$^+$13b] i.e., $\langle k_z k_\theta\rangle = \sum_{\mathbf{k}} k_z k_\theta \left|\hat{\phi}_{\mathbf{k}}\right|^2 / \sum_{\mathbf{k}} \left|\hat{\phi}_{\mathbf{k}}\right|^2 \neq 0$. The symmetry breaking can be assessed by investigating the joint probability density function (PDF) of radial and axial velocity fluctuations, $\mathrm{P}\left(\tilde{v}_r, \tilde{v}_z\right)$. Note that in CSDX we have $\tilde{v}_z \sim \nabla_{\|}\tilde{P} \sim k_z\tilde{\phi}$ and $\tilde{v}_r \sim k_\theta\tilde{\phi}$, due to the adiabatic electron response and negligible temperature fluctuations. By normalizing the

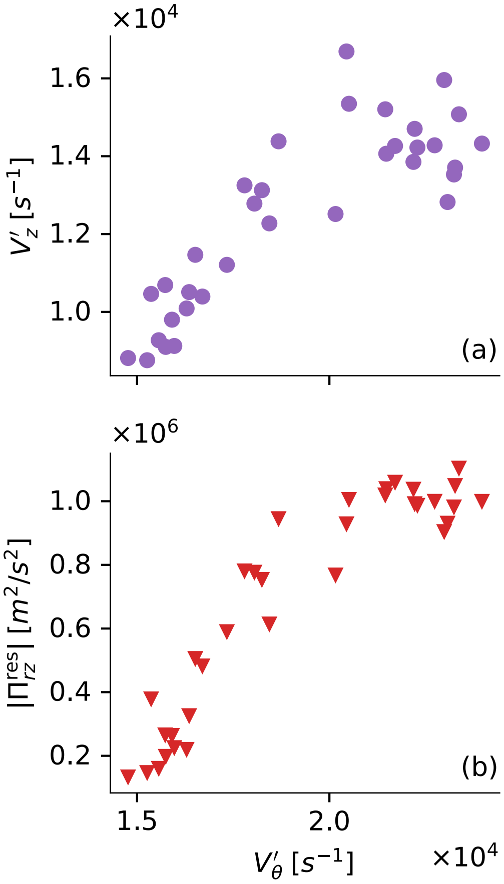

Figure 5.9: Axial flow shear (a) and magnitude of axial residual stress (b) plotted as a function of azimuthal flow shear.

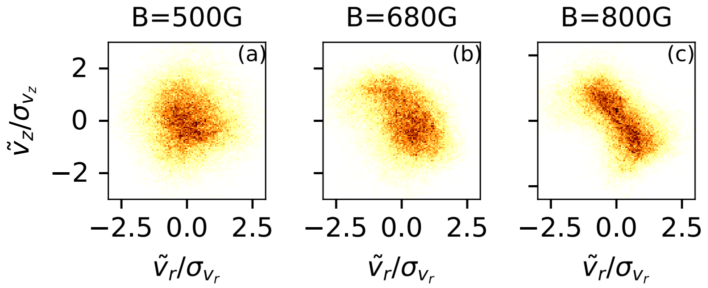

Figure 5.10: Joint PDF of radial and axial velocity fluctuations, $\mathsf{P}\left(\tilde{v}_r, \tilde{v}_z\right)$, at different magnetic fields at $r \approx 3$ cm. Normalization is the standard deviations.

velocity fluctuations using their standard deviations, $\mathsf{P}\left(\tilde{v}_r, \tilde{v}_z\right)$ can represent the correlator $\langle k_z k_\theta \rangle$. As shown in Fig. 5.10, the anisotropy of $\mathsf{P}\left(\tilde{v}_r, \tilde{v}_z\right)$ grows with increasing B field strength and ∇n. The critical density gradient occurs at $B \approx 650$ G, and $\mathsf{P}\left(\tilde{v}_r, \tilde{v}_z\right)$ starts to tilt (Fig. 5.10(b)) at slightly higher B and ∇n. At higher ∇n, $\mathsf{P}\left(\tilde{v}_r, \tilde{v}_z\right)$ is strongly elongated along the diagonal, suggesting large asymmetry in $\langle k_z k_\theta \rangle$.

As proposed by the dynamical symmetry breaking model,[LDXT16b] the mean axial flow shear modifies the drift wave growth rate, by introducing a frequency shift proportional to $k_z k_\theta V_z'$. In our experiments, the seed axial flow shear is negative, $V_z' < 0$, because $V_z(r)$ is initially driven by the axial pressure drop and hence decreases from the core to the edge. As a result, the modes with $\langle k_z k_\theta \rangle < 0$ grow faster than modes with $\langle k_z k_\theta \rangle > 0$, and eventually become dominant. This in turn induces a spectral imbalance, with predominance of the spectral intensity in quadrants II and IV of the $k_\theta - k_z$ plane, as shown in the right panel of Fig. 5.11. The predicted spectral imbalance, $\langle k_\theta k_z \rangle < 0$, is consistent with the tilted contour of $\mathsf{P}\left(\tilde{v}_r, \tilde{v}_z\right)$, as shown in left panel of Fig. 5.11. Since larger residual stress occurs at higher ∇n, we can therefore infer that this symmetry breaking is related to a finite residual stress.

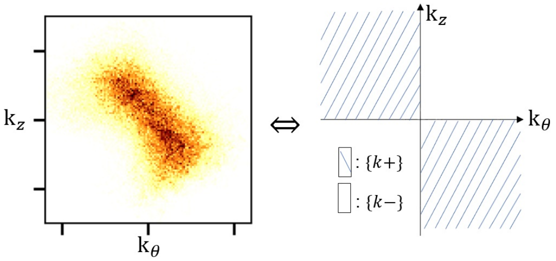

Figure 5.11: Measured joint PDF $\mathrm{P}(\tilde{v}_r, \tilde{v}_\theta)$ (left) and prediction of spectral imbalance in $k_z - k_\theta$ plane by the dynamical symmetry breaking model (right).

5.7 Conclusions

In this work, we study axial and azimuthal flow dynamics in drift wave turbulence in CSDX. We focus on possible interactions between azimuthal and axial flows. The principal results of this study are:

- Turbulent azimuthal Reynolds stresses $\langle \tilde{v}_r \tilde{v}_\theta \rangle$ drive zonal flows which regulate the turbulence.
- Turbulent axial Reynolds stresses $\langle \tilde{v}_r \tilde{v}_z \rangle$ drive axial flows–akin to intrinsic rotation. However, the azimuthal Reynolds power is much larger than the axial Reynolds power, i.e. $\mathcal{P}_\theta^{Re} \gg \mathcal{P}_z^{Re}$, so one may regard the axial flow evolution as parasitic to the drift wave–zonal flow system. This is consistent with the observation that $V_\theta' \ll \omega_k$ (i.e. moderate azimuthal flow shear) and thus there is no transport barrier.
- Spectral symmetry breaking was observed and measured–i.e., $\langle k_\theta k_z \rangle \neq 0$. The observed broken symmetry is consistent with that required for axial flow generation. The symmetry breaking is dynamical, and is not produced by magnetic field geometry.
- Azimuthal and axial flows scale with ∇n, consistent with the scenario of the engine model of the system.
- Experimental results support the predictions of the reduced model discussed in this paper.

We emphasize that conclusions pertinent to azimuthal–axial flow coupling are limited to magnetic field in range from 500 G to 1000 G. In this range, $V'_\theta \ll \omega_k$ and $L_{V_z}^{-1} \ll \left(L_{V_z}^{\mathrm{PSFI}}\right)^{-1}$, which are fundamental to the system dynamics observed and modeled here.

Chapter 5 has been submitted for publication of the material as it may appear in R. Hong, J. C. Li, R. Hajjar, S. Chakraborty Thakur, P. H. Diamond, and G. R. Tynan, "Generation of Parasitic Axial Flow by Drift Wave Turbulence with Broken Symmetry: Theory and Experiment", *Physics of Plasmas* (2018), American Institute of Physics. The dissertation author was the primary investigator and author of this article.

Chapter 6

Another Look at Zonal Flow Physics: Resonance, Shear Flows and Frictionless Saturation

6.1 Introduction

Zonal flows (ZF) are very effective at regulating drift wave (DW) turbulence, as they are the secondary modes of minimal inertia, transport, and damping[DIIH05b, GD15]. Such a mechanism naturally can be thought of as an element in a 'predator–prey' type ecology[DLCT94, KGD15], in which the secondary 'predator' feeds off (i.e., extracts energy from) of the primary 'prey'. In such a system, the damping of the predator (here, the ZF) ultimately regulates the full system. Frictional drag, due to collisions, is usually invoked to damp ZF. However, this picture is unsatisfactory for present day and future regimes of low collisionality. Thus, it becomes essential to understand *frictionless* ZF saturation and its implications for drift wave turbulence. Of course, ZF saturation significantly impacts transport and turbulence scalings. Note that understanding scalings in the frictionless regime is essential for developing reduced models thereof.

As zonal flow shear reduces the turbulent mixing scale, the saturated zonal flow is coupled to the scaling of turbulent diffusivity with $\rho_* \equiv \rho_s/L_n$. This is related to the degree of gyro-Bohm breaking[MPW$^+$01], i.e. the exponent α in $D \sim D_B \rho_*^{\alpha}$, where $D_B \equiv k_B T/16eB$ is Bohm diffusivity and $\alpha < 1$ indicates gyro-Bohm breaking.

Related to zonal flow saturation, we note that strong resonance between drift waves and azimuthal (i.e., zonal) flow is observed in a linear device CSDX (Controlled Shear Decorrelation eXperiment), i.e. $\omega_k - k_\theta \langle v_\theta \rangle \ll \omega_{*e}$, with ω_{*e} being the electron drift frequency. CSDX is a well-diagnosed venue to study the interaction between turbulence and turbulence driven flows in straight magnetic fields[XTD$^+$11a, CAT$^+$16]. Though resonance is manifested most clearly in the linear device, it has more general implications for confinement devices.

Wave-flow resonance enters turbulence regulation by zonal flows both linearly and nonlinearly. Resonance alters our understanding of the shear suppression mechanisms. To this end, the effects of $E \times B$ shear flows on turbulence have been intensively studied. However, simplified shear suppression models are *not* universally applicable. In some limits, weak flow shear can even destabilize turbulence due to the coupling of radial eigenmodes[WDR92]. Moreover, flow shearing alone is not the only parameter that characterizes all effects of flow structure on turbulence[WJGH92]. For example, wave-flow resonance stabilizes turbulence through wave absorption[WDR92, CSD$^+$92]. Yet, resonance is often overlooked by many existing shear suppression models.

Resonance also suggests saturation mechanisms for zonal flows. Many works on zonal flow generation[DIIH05b, GD15, GHD15, GD16] exist, but the question of how zonal flows saturate, absent frictional drag, remains open. Though sometimes mentioned in this context, tertiary instability is *not* effective for most cases of ZF saturation as it is strongly suppressed by magnetic shear. Indeed, in simulation studies, onset of tertiary instability requires an *artificial* increase in the ZF shearing rate[RDK00] so as to overcome the stabilizing effects of magnetic shear. Ion temperature gradients can provide an extra source of free energy to drive the tertiary mode, in addition to flow shear. However, such a contribution to the growth rate of the tertiary mode is of order $O(k^2\rho_i^2)$, and thus does not qualitatively alter tertiary stability[KD02]. Tertiary instability of ZF may occur in flat-q regimes[MAC$^+$11a] with zero magnetic shear. Even there, the key question of just how much turbulent mixing and flow damping result remains to be addressed.

In this work, we discuss the role of wave–flow resonance in zonal flow dynamics. Specifically, we investigate whether the conventional shear suppression rules still hold true when wave–flow resonance is considered. In addition, we study how resonance enters zonal flow regulation. In particular, we seek to answer the following questions:

(1) How do zonal flows saturate in the frictionless regime? What determines the stationary flow scale? To what degree is the often-quoted gyro-Bohm scaling broken?

(2) How do we incorporate the resonance effect in a predator–prey model? How is this new model different from previous ones?

We find that flow shear can destabilize the drift wave turbulence through the resonance. This *contradicts* the conventional wisdom that the flow shear always suppresses turbulence. Resonance between drift wave and plasma flow suppresses the instability by wave absorption. Increasing the flow shear, with fixed flow magnitude, can weaken the resonance. Consequentially, the flow shear increment actually *destabilizes* the drift wave turbulence. This suggests that the flow shear can affect the stability via resonance in a way opposite to what the conventional shear suppression models predict. Thus, wave-flow resonance is an important factor to be considered when studying shear flow effects on stability, and on quasilinear fluxes that transport particles, vorticity, and momentum.

We study drift–ZF turbulence with special focus on the frictionless regime where the flow drag → 0. Note that the DW drive–which can depend on electron collisionality–is not affected by the distinction between frictional and frictionless ion regimes, since frictional damping of

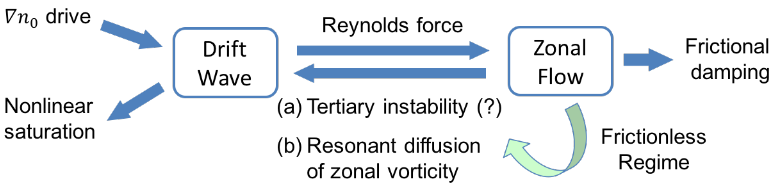

Figure 6.1: Frictionless zonal flow saturation by (a) tertiary instability and (b) resonant vorticity diffusion.

drift *waves* is weak. Many works on ZF generation[DIIH05b, GD15] exist, but the question of how ZF saturates, absent frictional drag, remains open. *We show that turbulent mixing of zonal vorticity by drift waves in the presence of ZF saturates secondary flows for near-marginal turbulence* (with low to zero frictional drag), *and thus is effective at regulating the Dimits up-shift regime.* The Dimits regime[DWBC96, DIIH05b] is that of a frictionless DW–ZF system close to the linear instability threshold, where nearly all the energy of the system is coupled to ZF, so that the residual transport and turbulence are weak, though finite. This induces an up-shift in the onset of the turbulent fluxes when plotted vs ∇T. Turbulent vorticity mixing is fundamentally different from viscous flow damping. Turbulent vorticity mixing conserves total potential enstrophy (PE) between the mean field–i.e., the zonal component–and fluctuations. In contrast, the flow viscosity dissipates both the ZF and (DW flow) fluctuations, and so is an energy sink for all. Fig. 6.1 illustrates the paradigm shift from the hypothetical saturation induced by tertiary instability to the saturation by vorticity mixing.

The ZF saturation mechanism induced by resonant vorticity mixing is incorporated as a nonlinear self-regulating effect in an extended predator-prey model[KGD15, DLCT94]. Stationary turbulence and flow states are calculated and compared in the frictionless, weakly frictional, and strongly frictional regimes. In the frictionless regime, the results are different from the conventionally quoted scalings derived for frictional regimes.

Turbulent vorticity mixing is driven by resonance between drift wave and zonal flow. It is analogous to Landau damping absorption of plasmons during collapse of Langmuir turbulence[GSSS77,

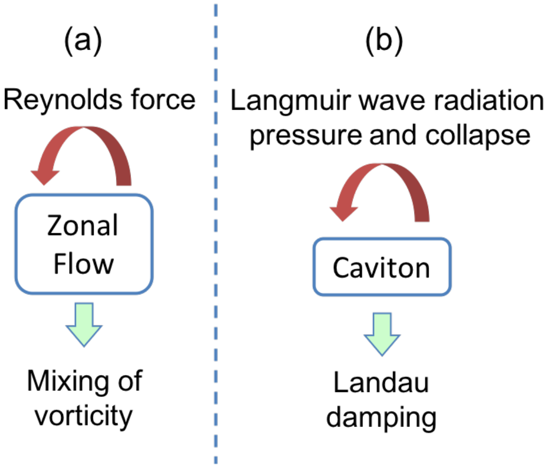

Figure 6.2: Comparison of the generation and frictionless dissipation of (a) zonal flow and (b) caviton.

CGDS17]. In the latter case, plasmon Landau damping arrests collapse, leaving an "empty cavity", without its "filling" of Langmuir wave pressure. Table 6.1 compares these two processes. Both zonal flow formation and Langmuir collapse (i.e., the formation of caviton) result from modulational instability, and they both saturate in the collisionless regime. Moreover, both Landau damping and vorticity mixing conserve energy (or potential enstrophy, in the case of vorticity mixing). The key difference between the two is the detail of the resonance. The resonance considered here is between drift wave phase velocity and flow velocity, while conventional Landau resonance considers the resonance between phase velocity and particle velocity. Landau resonance defines a series of resonant surfaces in (x,v) phase space. When the islands around adjacent surfaces overlap, the trajectory of a particle becomes chaotic, leading to mixing of phase space density (Fig. 6.3). As a result, the particle PDF (probability density function) evolves stochastically, i.e., as by a Fokker–Planck equation in velocity. In contrast, resonant diffusion mixes vorticity in real space. The diffusive scattering of zonal vorticity profile is resonant. Therefore, irreversibility results from stochastic vorticity trajectories due to overlapping islands in real space, i.e., the (x,y) space.

The rest of this paper is organized as follows. Sec. 6.2 presents the wave-flow resonance

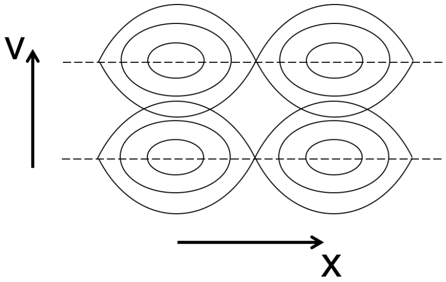

Figure 6.3: Overlapping islands in phase space. The dashed lines represent resonant surfaces.

Table 6.1: Comparison and contrast of Landau damping effects on cavity collapse during Langmuir turbulence collapse and resonance effects on frictionless zonal flow (ZF) saturation.

	Langmuir turbulence collapse	Frictionless ZF saturation
Primary player	Plasmon-Langmuir wave	Drift wave turbulence
Secondary player	Ion-acoustic wave (caviton)	Zonal flow
Free energy source	Langmuir turbulence driver	∇n, ∇T drive
Final state	Nearly empty cavity	Saturated zonal flow and residual turbulence
Resonance	Landau damping	$\omega_k - k_y \langle v_y \rangle$ absorption
Other damping effects	Ion-acoustic radiation	Wave packet trapping

effect on stability, specifically how the flow magnitude and flow shear affect the stability via resonance. Sec. 6.3 discusses how zonal flow saturation in the frictionless regime is regulated by the resonance. Sec. 6.4 summarizes and discusses the main results of this paper.

6.2 Wave-Flow Resonance Effect on Stability

Shear is not the only flow property that controls the stability of turbulence. We reconsider the shear suppression models by incorporating the the effects of resonance. Resonance between drift wave and flow stabilizes the turbulence via wave absorption. The flow shear weakens the resonance, and thus actually enhances the turbulence. Also, we show that the flow magnitude enhances the resonance, and thus, stabilizes the drift wave. The flow magnitude (V_{max}) is defined as the maximum flow velocity in the electron drift direction. Increasing V_{max} reduces the value of $\omega_k - kV_{max}$, and thus enhances the resonance.

We study the Hasegawa–Wakatani drift wave system in slab geometry with a mean perpendicular flow $\langle v_y \rangle$ varying in the $\hat{x}$ direction:

$$\left(\frac{d}{dt} + \tilde{\mathbf{v}}_E \cdot \nabla\right) \tilde{n} + \tilde{v}_x \frac{\nabla n_0}{n_0} = D_\parallel \nabla_\parallel^2 (\tilde{n} - \tilde{\phi}) + D_c \nabla^2 \tilde{n}, \tag{6.1}$$

$$\left(\frac{d}{dt} + \tilde{\mathbf{v}}_E \cdot \nabla\right) \tilde{\rho} + \tilde{v}_x \langle \rho \rangle' = D_\parallel \nabla_\parallel^2 (\tilde{n} - \tilde{\phi}) + \chi_c \nabla^2 \tilde{\rho}, \tag{6.2}$$

where we define $D_\parallel \equiv v_{The}^2/\nu_{ei}$ and $d/dt \equiv \partial_t + \langle v_y \rangle \partial_y$. ν_{ei} is the frequency of electron–ion collision and v_{The} is the electron thermal speed. We have normalized electric potential fluctuation as $\tilde{\phi} \equiv e\delta\phi/T_e$ and density fluctuation as $\tilde{n} \equiv \delta n/n_0$, where n_0 is the equilibrium density. The magnetic field is in the $\hat{z}$ direction, and both n_0 and $\langle v_y \rangle$ vary only in $\hat{x}$ direction. The vorticity fluctuation is $\tilde{\rho} \equiv \rho_s c_s \nabla_\perp^2 \tilde{\phi}$ where ρ_s is the ion Larmor radius at electron temperature and c_s is the ion sound speed, and the zonal vorticity is $\langle \rho \rangle \equiv \langle v_y \rangle'$. $\tilde{\mathbf{v}}_E \equiv c_s \hat{\mathbf{z}} \times \nabla \tilde{\phi}$ is the $E \times B$ velocity fluctuation. D_c and χ_c are the collisional particle diffusivity and vorticity diffusivity (i.e., viscosity). Drift wave is the dominant instability population, because the vorticity gradient drive is quantitatively weaker than the ∇n_0 drive, i.e. $k_y \rho_s^2 \langle v_y \rangle'' / \omega_{*e} \ll 1$ where $\omega_{*e} \equiv k_y \rho_s c_s / L_n$ is the electron drift frequency and $L_n \equiv n_0 / |dn_0/dx|$ is the density gradient scale.

In the following subsections, we show how conventional shear suppression models fail in the presence of strong wave–flow resonance.

6.2.1 Resonance Effects on Stability

Wave-flow resonance stabilizes drift waves through wave absorption. The instability is linked to the mode scale L_m (defined by Eq. (6.5)). The key resonance, here, is between the phase velocity of drift waves and the fluid velocity of plasma, i.e. $\omega_k - k_y \langle v_y \rangle$. Due to the resonance effect, the eigenmode peaks around the position where $|\omega_k - k_y \langle v_y \rangle|$ is a minimum. When the resonance becomes stronger, the scale of the eigenmode decreases. The mode scale is effectively the wavelength in the $\hat{x}$ direction, i.e. $k_x \rho_s \sim L_m^{-1} \rho_s$. Hence, the resonance regulates the turbulent fluxes by varying the mode scale.

We can write the fluctuating quantities in Eq. (6.1)–(6.2) as Fourier components in the $\hat{y}$ and parallel ($\hat{z}$) directions, while retaining the amplitude variation in the $\hat{x}$ direction, i.e.

$$\tilde{\phi}(x,y,z,t) = \sum_{k_y, k_\parallel} \phi(x) e^{i\left(k_y y + k_\parallel z - \Omega_k t\right)},$$

$$\tilde{n}(x,y,z,t) = \sum_{k_y, k_\parallel} n(x) e^{i\left(k_y y + k_\parallel z - \Omega_k t\right)}.$$

The complex frequency Ω_k consists of a real frequency and a growth rate, i.e. $\Omega_k = \omega_k + i\gamma_k$. Electrons are weakly non-adiabatic, i.e. $\tilde{n} = (1 - i\delta)\tilde{\phi}$ with $\delta \ll 1$. The nonadiabatic electron response δ is determined by the frequency shift $\delta = (\omega_{*e} - \omega_k + k_y \langle v_y \rangle)/(k_\parallel^2 D_\parallel) \ll 1$, given that the adiabatic factor is $k_\parallel^2 D_\parallel/\omega_{*e} \gg 1$. The eigenmode equation for $\phi(x)$ is then

$$(\omega_k - k_y\langle v_y\rangle + i\gamma_k)\,\rho_s^2\partial_x^2\phi = \left[\left(1 + k_y^2\rho_s^2 - i\delta\right)(\omega_k - k_y\langle v_y\rangle + i\gamma_k) - \omega_{*e} - k_y\rho_s^2\langle v_y\rangle''\right]\phi, \quad (6.3)$$

where the collisional viscosity χ_c has been neglected. Multiplying both sides of Eq.(6.3) by ϕ^*, and integrating over the $\hat{x}$ direction, we obtain

$$(\omega_k - k_y\langle v_y\rangle + i\gamma_k)\,L_m^{-2}\rho_s^2 + \left[\left(1 + k_y^2\rho_s^2 - i\delta\right)(\omega_k - k_y\langle v_y\rangle + i\gamma_k) - \omega_{*e}\right] = 0 \qquad (6.4)$$

where the mode scale L_m is defined by

$$L_m^{-2}\rho_s^2 \equiv \frac{\rho_s^2\int_0^{L_x} dx|\partial_x\phi|^2}{\int_0^{L_x} dx|\phi|^2}. \qquad (6.5)$$

Here, we have used the boundary condition $\phi(0) = \phi(L_x) = 0$. In addition, the vorticity gradient term is ignored in Eq.(6.4), because it is quantitatively negligible as compared to ω_{*e}.

The Doppler shifted frequency and the growth rate are obtained from Eq. (6.4)

$$\omega_k \cong \frac{\omega_{*e}}{1 + k_y^2\rho_s^2 + L_m^{-2}\rho_s^2}, \qquad (6.6)$$

$$\gamma_k \cong \frac{\omega_{*e}^2}{k_\parallel^2 D_\parallel}\frac{k_y^2\rho_s^2 + L_m^{-2}\rho_s^2}{(1 + k_y^2\rho_s^2 + L_m^{-2}\rho_s^2)^3}. \qquad (6.7)$$

When resonance becomes stronger, i.e. $|\omega_k - k_y\langle v_y\rangle|_{\min}$ decreases, the eigenmode becomes narrower (mode scale L_m/ρ_s decreases), and thus the growth rate decreases. Therefore, stronger resonance stabilizes the drift wave.

6.2.2 Effect of Flow Magnitude on Stability

Increasing the flow magnitude enhances resonance, thus stabilizes the drift wave. We consider the regime where $0 < |\omega_k - k_y \langle v_y \rangle|_{\min} \ll \omega_{*e}$. Here, the resonance is stronger, but there is no singularity in the eigenmode equation. As $\langle v_y \rangle$ increases, resonance is enhanced. Therefore, increasing the flow *magnitude* suppresses instability.

In order to illustrate the effect of flow on the resonance, and thus on stability, we numerically solve the eigenmode equation Eq. (6.3) for wave frequency ω_k, growth rate γ_k, and eigenmode profile $\phi(x)$. The chosen parameters are a proxy for realistic CSDX parameters, which are $L_x = 6$ cm, $\rho_s = 1.2$ cm, $L_n = 2$ cm, $k_y \rho_s = \pi / L_x$. Dirichlet boundary conditions are used, which are $\phi(0) = \phi(L_x) = 0$. The adiabatic factor is $k_\parallel^2 D_\parallel / \omega_{*e} = 3$, so electrons are nearly adiabatic with $\delta \cong 1/3$. We use the hyperbolic tangent function to describe the flow profile, which is

$$\langle v_y \rangle = V_{max} \tanh \frac{x - 0.5 L_x}{L_V}. \tag{6.8}$$

Here, the maximum flow shear is given by V_{max}/L_V. This allows us to vary either the flow magnitude or the flow shear, while keeping the other fixed.

As the flow magnitude increases and the flow shear remains constant, the resonance becomes stronger (Fig. 6.6, left panel). Hence, the mode peak moves closer to the position with the minimum $|\omega_k - k_y \langle v_y \rangle|$, which is at $x = L_x$ (Fig. 6.5). As a result, instability is suppressed (Fig. 6.6, right panel).

6.2.3 Effect of Flow Shear on Stability

Flow shear weakly destabilizes the drift wave by weakening the resonance. As a result, the eigenmode profile is flattened (Fig. 6.7). This increases the mode scale L_m/ρ_s (Fig. 6.8, left panel). Hence, the drift wave is destabilized by the flow shear (Fig. 6.8, right panel).

Note that the increment in growth rate is not due to enhanced KH instability, because KH drive is quantitatively negligible as compared to drift wave drive here.

6.3 Frictionless ZF Saturation by Resonant PV Mixing

In this section, we show that resonant scattering of the zonal vorticity can saturate secondary flows in the frictionless regime. This process is distinct from the tertiary mechanism. This shift in paradigm is illustrated by the diagram in Fig. 6.1. The resonant vorticity diffusion can saturate flows in both marginal and strong turbulence regimes. The stationary flow results from the balance between the residual vorticity flux and the resonant scattering effect. Since both of them scale with the turbulence intensity, the stationary flow is then independent of turbulence strength to leading order. Therefore, this saturation mechanism is effective in the Dimits up-shift regime, where turbulence is marginally unstable. We calculate the stationary zonal flow shear and scale directly from analysis, and determine the degree of gyro-Bohm breaking resulting from strong zonal flow shear.

This saturation mechanism is incorporated into a extended 0D predator–prey model. The flow state and turbulence level are calculated for frictionless, weakly frictional, and strongly frictional regimes, and compared to previous results. Also, we use drift wave turbulence as an example case to calculate the saturated flow state in the frictionless regime. Study for the 0D model lends considerable insight by enabling calculation of flow scales, and flow and turbulence states (i.e., fixed points). However, a 1D model is necessary to study the spatiotemporal evolution in physical systems, such as staircase formation and avalanches[DPDG$^+$10, NCDH96].

6.3.1 Drift Wave–Zonal Flow System in the Resonant PV Mixing Framework

The generation and saturation of zonal flows by drift waves are described by PV (potential vorticity) mixing. The fluctuating PV is defined as $\tilde{q} \equiv \tilde{n} - \tilde{\rho}$, and the zonal PV is

$\langle q \rangle \equiv \langle n \rangle - \langle \rho \rangle$. Hence, the evolution equation for fluctuating PV can be obtained by subtracting Eq. (6.2) from Eq. (6.1), yielding

$$\left(\frac{d}{dt} + \tilde{\mathbf{v}}_E \cdot \nabla\right) \tilde{q} + \tilde{v}_x \frac{\partial}{\partial x} \langle q \rangle = D_{q,c} \nabla^2 \tilde{q}. \tag{6.9}$$

Here, $D_{q,c} \sim (D_c + \chi_c)/2$ is the collisional diffusivity of PV. In multiplying both sides of Eq. (6.9) by $\tilde{q}$, we obtain the potential enstrophy (PE)–i.e., $\Omega \equiv \langle \tilde{q}^2 \rangle /2$–equation[AD16, AD17]:

$$\frac{\partial}{\partial t} \Omega = -\frac{\partial}{\partial x} \frac{\langle \tilde{v}_x \tilde{q}^2 \rangle}{2} - \langle \tilde{v}_x \tilde{q} \rangle \frac{\partial}{\partial x} \langle q \rangle - \varepsilon_c \Omega^{3/2} + \gamma_L \Omega. \tag{6.10}$$

The turbulent PE flux is due to nonlinear spreading, and can be approximated as a diffusive flux, i.e., $\langle \tilde{v}_x \tilde{q}^2 \rangle /2 \sim -D_\Omega \partial_x \Omega$[AD16]. The nonlinear PE dissipation $\varepsilon_c \Omega^{3/2}$ represents the forward cascade (to dissipation) of PE. γ_L is the characteristic linear growth rate of drift waves, which drives the turbulence and thus produces PE. The coupling of PV flux and zonal PV profile gradient conserves PE between mean field and fluctuations.

The equations for mean-field density and zonal vorticity are

$$\frac{\partial}{\partial t} \langle n \rangle = -\frac{\partial}{\partial x} \langle \tilde{v}_x \tilde{n} \rangle + D_c \nabla^2 \langle n \rangle, \tag{6.11}$$

$$\frac{\partial}{\partial t} \langle \rho \rangle = -\frac{\partial}{\partial x} \langle \tilde{v}_x \tilde{\rho} \rangle - \mu_c \langle \rho \rangle - \mu_{NL} \langle \rho \rangle + \chi_c \nabla^2 \langle \rho \rangle. \tag{6.12}$$

μ_c is frictional drag coefficient. The nonlinear flow damping rate μ_{NL} depends on $\langle \rho \rangle$, and is set by tertiary modes, e.g. Kelvin–Helmholtz instability of zonal flows. In reality, the onset of such tertiary modes requires the ZF shear to exceed a threshold[RDK00], in order to overcome the damping of magnetic shear. Onset of tertiary instability can be included in reduced models, if needed. However, here we neglect it, because the relevance of such tertiary modes to ZF saturation in confinement devices is negligible.

To close the system, we need to calculate the turbulence-driven fluxes. The quasilinear PV flux is diffusive, i.e.,

$$\langle \tilde{v}_x \tilde{q} \rangle = -D_{q,turb} \frac{\partial}{\partial x} \langle q \rangle, \tag{6.13}$$

which is obtained from Eq. (6.9), neglecting collisional diffusion. Here, the turbulent diffusivity of PV has a resonant part and a non-resonant part, i.e., $D_{q,turb} = D_q^{\text{res}} + D_q^{\text{non-res}}$.

The resonant diffusivity of PV is set by the resonance between phase velocity of drift wave and the local ZF profile, which yields

$$D_q^{\text{res}} = \sum_k |\tilde{v}_{x,k}|^2 \pi \delta(\omega_k - k_y \langle v_y \rangle), \tag{6.14}$$

where $\tilde{v}_{x,k}$ is the fluctuating velocity in the radial direction and ω_k is the drift wave frequency. The resonant scattering here has a characteristic spectral autocorrelation time scale $\tau_{ck} \sim |\Delta(\omega_k - k_y \langle v_y \rangle)|^{-1} \sim \left\{ |(v_{g,y} - v_{ph,y}) \Delta k_y| + |v_{g,x} \Delta k_x| \right\}^{-1}$, where we have used $\langle v_y \rangle \cong \omega_k / k_y = v_{ph,y}$. The resonance is between drift waves and the instantaneous ZF profile. Thus, this autocorrelation time is shorter than the time scale of ZF evolution, i.e., $\tau_{ck} \ll \tau_{ZF}$, consistent with ZF evolution by turbulent PV mixing. The correlation time τ_{ck} is shorter as compared to the 1D case, where the spectral width is associated with the mismatch between group velocity and phase velocity, i.e., $\tau_{ck} \sim |(v_g - v_{ph}) \Delta k|^{-1}$, only. As a result, the resonant diffusivity is $D_q^{\text{res}} = \sum_k k_y^2 \rho_s^2 c_s^2 |\phi_k|^2 \tau_{ck}$.

The non-resonant diffusivity can be obtained by quasilinear theory, and is

$$D_q^{\text{non-res}} = \sum_{\omega_k \neq k_y \langle v_y \rangle} k_y^2 \rho_s^2 c_s^2 |\phi_k|^2 \frac{|\gamma_k|}{|\omega_k - k_y \langle v_y \rangle|^2}. \tag{6.15}$$

γ_k is the linear growth rate of drift waves. In marginally stable turbulence, γ_k should be replaced by the nonlinear decorrelation rate of turbulence, i.e., $\Delta\omega N_k / N_0$ where $N_k \sim |\phi_k|^2 / \omega_k$ is the wave action density. As a consequence, in marginally stable turbulence, the non-resonant diffusivity is

$$D_q^{\text{non-res}} = \sum_{\omega_k \neq k_y \langle v_y \rangle} k_y^2 \rho_s^2 c_s^2 \frac{|\Delta\omega|}{I_0} \frac{|\phi_k|^2 |\phi_k|^2}{|\omega_k - k_y \langle v_y \rangle|^2}, \tag{6.16}$$

where $I_0 \equiv \sum_k |\phi_k|^2$. This is analogous to wave–particle scattering due to higher order Landau resonance[MD68] in Vlasov plasmas. The Doppler shifted frequency and the growth rate of the drift wave are given by Eq. (6.6) and (6.7). Both of them depend upon the eigenmode scale in radial direction, which is $L_m \equiv \langle k_x^2 \rangle^{-1/2}$. Thus, the non-resonant diffusivity depends on the mode scale, which yields

$$D_q^{\text{non-res}} \sim \sum_{\omega_k \neq k_y \langle v_y \rangle} \frac{k_y^2 \rho_s^2 c_s^2}{k_\parallel^2 D_\parallel} \frac{k_y^2 \rho_s^2 + L_m^{-2} \rho_s^2}{1 + k_y^2 \rho_s^2 + L_m^{-2} \rho_s^2} |\phi_k|^2. \tag{6.17}$$

The mode scale does not affect the turbulent diffusivity significantly. This follows since for drift wave scaling where $k_y \rho_s \sim 1$, the factor involving the mode scale does not vary strongly (with that scale) while it ranges from 0.5 to 1. The non-resonant diffusivity is negligible in comparison to the resonant diffusivity, because $D_q^{\text{non-res}} \sim (k_\parallel^2 D_\parallel)^{-1}$ and $k_\parallel^2 D_\parallel \gg \tau_{ck}^{-1}$ for near–adiabatic electrons. Therefore, the mixing of PV is primarily *resonant*.

The turbulent particle flux driven by drift wave turbulence in the adiabatic regime is diffusive, i.e.,

$$\langle \tilde{v}_x \tilde{n} \rangle = -D_{n,\text{turb}} \frac{\partial}{\partial x} \langle n \rangle, \tag{6.18}$$

where

$$D_{n,\text{turb}} = \sum_k \frac{k_y^2 \rho_s^2 c_s^2}{k_\parallel^2 D_\parallel} \frac{k_y^2 \rho_s^2 + L_m^{-2} \rho_s^2}{1 + k_y^2 \rho_s^2 + L_m^{-2} \rho_s^2} |\phi_k|^2. \tag{6.19}$$

We can then obtain the vorticity flux by subtracting the PV flux from the particle flux, i.e., $\langle \tilde{v}_x \tilde{\rho} \rangle = \langle \tilde{v}_x \tilde{n} \rangle - \langle \tilde{v}_x \tilde{q} \rangle$, which is

$$\langle \tilde{v}_x \tilde{\rho} \rangle = -(D_{n,\text{turb}} - D_q^{\text{res}}) \frac{\partial}{\partial x} \langle n \rangle - D_q^{\text{res}} \frac{\partial}{\partial x} \langle \rho \rangle. \tag{6.20}$$

Here, the last term is the flux induced by resonant diffusion. The non-diffusive component forms a *residual vorticity flux*, i.e., $\Gamma_{\rho}^{Res} = -(D_{n,\text{turb}} - D_q^{\text{res}})\partial_x \langle n \rangle$. Γ_{ρ}^{Res} is driven by drift wave turbulence, so it is proportional to the density gradient. As discussed in Ref. [DIIH05b], Γ_{ρ}^{Res} drives zonal flows against diffusive vorticity mixing. The gradient of Γ_{ρ}^{Res} can accelerate zonal flows from rest. Note that this mean field calculation of the vorticity flux is technically applicable to the stationary state, while modulational instability analysis is limited to the stage of ZF growth.

We then arrive at the DW–ZF system including resonant PV mixing, which is

$$\frac{\partial}{\partial t}\langle n \rangle = \frac{\partial}{\partial x} D_{n,\text{turb}} \frac{\partial}{\partial x}\langle n \rangle + D_c \nabla^2 \langle n \rangle, \tag{6.21}$$

$$\frac{\partial}{\partial t}\langle \rho \rangle = \frac{\partial}{\partial x}\left[(D_{n,\text{turb}} - D_q^{\text{res}})\frac{\partial}{\partial x}\langle n \rangle + D_q^{\text{res}}\frac{\partial}{\partial x}\langle \rho \rangle\right] - \mu_c \langle \rho \rangle - \mu_{NL}\langle \rho \rangle + \chi_c \nabla^2 \langle \rho \rangle, \tag{6.22}$$

$$\frac{\partial}{\partial t}\Omega = D_{\Omega}\frac{\partial^2}{\partial x^2}\Omega + D_q^{\text{res}}\left[\frac{\partial}{\partial x}(\langle n \rangle - \langle \rho \rangle)\right]^2 - \varepsilon_c \Omega^{3/2} + \gamma_L \Omega. \tag{6.23}$$

This system consists of the equations for mean-field density (Eq. (6.21)), zonal vorticity (Eq. (6.22)), and fluctuation PE (Eq. (6.23)). Initially produced by linear drift wave instability, the PE of this system is conserved up to frictional dissipation and nonlinear turbulent saturation, which transfer PE to small scales. The evolution of total PE is given by

$$\frac{\partial}{\partial t}\int dx \left[\Omega + \frac{(\langle n \rangle - \langle \rho \rangle)^2}{2}\right] = \int dx \left[\gamma_L \Omega - \varepsilon_c \Omega^{3/2} - D_{q,c}|\nabla(\langle n \rangle - \langle \rho \rangle)|^2 - \mu_c \langle \rho \rangle^2 - \mu_{NL}\langle \rho \rangle^2\right]. \tag{6.24}$$

The collisional diffusion of zonal PV (the term with $D_{q,c}$ in Eq. (6.24)) is a sink. In contrast, the turbulent PV diffusion conserves PE between mean field and fluctuations.

6.3.2 Frictionless ZF Saturation via Resonant PV Diffusion

As demonstrated by Ref. [Tay15, DK91], vorticity flux is identical to the Reynolds force, and thus drives the zonal flow. The residual vorticity flux excites the zonal flow, and thus the resonant diffusion is the only damping for zonal flows in the frictionless limit–i.e., $\mu_c, \chi_c, \mu_{NL} \to 0$. By multiplying Eq. (6.22) by $\langle \rho \rangle$, we obtain the net production of mean flow enstrophy in the frictionless limit, which is

$$\frac{\partial}{\partial t} \int dx \frac{\langle \rho \rangle^2}{2} = \int dx \left[-(D_{n,\text{turb}} - D_q^{\text{res}}) \frac{\partial \langle n \rangle}{\partial x} \frac{\partial \langle \rho \rangle}{\partial x} - D_q^{\text{res}} \left(\frac{\partial \langle \rho \rangle}{\partial x} \right)^2 \right]. \tag{6.25}$$

Hence, we see resonant diffusion of zonal vorticity saturates zonal flows in the frictionless regime–i.e., its contribution to $\partial_t \int dx \langle \rho \rangle^2$ is negative definite.

The zonal vorticity profile is stationary when the net flow production is zero, i.e., $\partial_t \int dx \langle \rho \rangle^2 = 0$. Therefore, in the frictionless regime, the stationary vorticity profile is determined by the balance between residual vorticity flux and the resonant vorticity diffusion (i.e., so $\langle \tilde{v}_x \tilde{\rho} \rangle = 0$) which implies

$$\langle v_y \rangle'' \sim -\frac{c_s}{\rho_s L_n} \left(1 - \frac{1}{\tau_{ck} k_\parallel^2 D_\parallel} \frac{k_y^2 \rho_s^2 + L_m^{-2} \rho_s^2}{1 + k_y^2 \rho_s^2 + L_m^{-2} \rho_s^2} \right). \tag{6.26}$$

In the relevant limit of near-adiabatic electrons, i.e., $\tau_{ck} k_\parallel^2 D_\parallel \gg 1$, the zonal flow scale is

$$L_{ZF} \sim \left(\frac{\langle v_y \rangle}{c_s} \right)^{1/2} \sqrt{\rho_s L_n}. \tag{6.27}$$

Only a fraction of turbulence energy is coupled to zonal flows. Thus, the flow magnitude is obtained using mixing length estimation for the turbulence energy, and a coupling fraction f:

$$\frac{\langle v_y \rangle^2}{c_s^2} \sim f \frac{l_{mix}^2}{L_n^2}. \tag{6.28}$$

Here, $0 < f < 1$ is the fraction of turbulence energy coupled to the zonal flow. Note that f and the mixing length are as yet unspecified. The flow scale follows as $L_{ZF} \sim f^{1/4} \sqrt{\rho_s l_{mix}}$, which depends only weakly on f. Clearly, the mixing length is much larger than the microscale

(ρ_s) and can be as large as an extended cell ($\sim L_n$), i.e., $\rho_s \ll l_{mix} \leq L_n$. Indeed, $l_{mix} \sim L_n$ is the appropriate "base state" scale, absent zonal flows. Thus, L_{ZF} necessarily lies between the microscale (ρ_s) and the mixing scale (l_{mix}). The questions are to determine the relative weighting of l_{mix} and ρ_s, and to account for shear modification of l_{mix}.

To determine l_{mix}, note that the base state mixing length is reduced by zonal flow shearing. This yields

$$l_{mix}^2 \sim \frac{l_0^2}{1+(\langle v_y\rangle'\tau_c)^2}, \tag{6.29}$$

where l_0 is the mixing length for zero flow shear. In the case of drift wave turbulence, we have $l_0 \sim L_n$ for extended cells absent flow shear.

For weak or modest zonal flow shear, the decorrelation time is the eddy turnover time. The eddy size is set by the mixing length and the eddy turning speed is set by the mean square root of the velocity fluctuations. Then, we obtain $\tau_c \sim \varepsilon^{-1/2} \sim l_{mix}/\langle\tilde{v}^2\rangle^{1/2}$. The mixing length model yields $\langle\tilde{v}^2\rangle/c_s^2 \sim (1-f)l_{mix}^2/L_n^2$. Thus, the mixing length is $l_{mix}^2 \sim (1-f)l_0^2 \Big/ \left(\frac{|\langle v_y\rangle|}{c_s}\frac{L_n}{L_{ZF}}\right)^2$. As a result, the zonal flow scale is $L_{ZF} \sim f^{1/6}(1-f)^{1/6}\rho_s^{2/3}l_0^{1/3}$. The zonal flow shear is then $|\langle v_y\rangle'| \sim f^{1/6}(1-f)^{1/6}\frac{c_s}{L_n}\left(\frac{l_0}{\rho_s}\right)^{1/3}$.

For strong zonal flow shear, i.e., $\langle v_y\rangle' \gg$ eddy turnover rate, the decorrelation time is set by $\tau_c \sim (\langle v_y\rangle'^2 k_r^2 D)^{-1/3}$, i.e., the scale set by the well known interaction of shearing and radial scattering[BDT90]. Due to the strong zonal flow shear, the turbulent diffusivity is resonant, so $D \sim \sum_k |\tilde{v}_r|^2\delta(\omega_k - k_\theta\langle v_y\rangle)$. The resonance time scale is controlled by the shearing rate, which yields $\delta(\omega_k - k_\theta\langle v_y\rangle) \sim |\langle v_y\rangle'|^{-1}$. Hence, the diffusivity becomes $D \sim (1-f)(c_s^2/|\langle v_y\rangle'|)(l_{mix}^2/L_n^2)$. The mixing length is $l_{mix}^2 \sim (1-f)^{2/3}l_0^2 \Big/ \left(\frac{|\langle v_y\rangle|}{c_s}\frac{L_n}{L_{ZF}}\right)^{4/3}$. The zonal flow scale is $L_{ZF} \sim f^{3/16}(1-f)^{1/8}\rho_s^{5/8}l_0^{3/8}$. The zonal flow shear is then $|\langle v_y\rangle'| \sim f^{3/16}(1-f)^{1/8}\frac{c_s}{L_n}\left(\frac{l_0}{\rho_s}\right)^{3/8}$. Here, the flow shear is larger, and the flow scale is larger. This follows because $|\langle v_y\rangle'| \sim |\langle v_y\rangle|/L_{ZF}$ and both $|\langle v_y\rangle|/c_s$ and L_{ZF} increase with the underlying drive scale (l_{mix}). Nevertheless, the flow shear calculated here is close to that calculated for the weak shear case.

Hence, in both cases, the flow shear are similar.

In either case, the factors f and $1-f$ enter with small exponents. Thus, the zonal flow emerges as mesoscopic, but weighted somewhat more strongly toward microscale (ρ_s) than macroscale (l_0). Note that while the mesoscopic zonal flow scale, i.e., $\rho_s < L_{ZF} < L_n$ and $L_{ZF} \sim \sqrt{\rho_s L_n}$ in particular, is frequently assumed, here they are determined by the analysis. The zonal flow shears in both cases are similar and robust. Even for the weak shear case, the calculated zonal flow shear is significant. Hence, the case of strong zonal flow shear–and thus flow resonance–is likely to be most relevant to the frictionless DW–ZF system discussed here. Note that we have calculated the zonal flow scale and shear self-consistently by considering the shearing feedback on mixing length. Externally driven flows may enhance the flow shearing, and thus reduces the mixing scale.

This mesoscopic zonal flow appears as a limiting case with near-adiabatic electrons (i.e., $\tau_{ck} k_\parallel^2 D_\parallel \gg 1$). When $\tau_{ck} k_\parallel^2 D_\parallel$ is comparable to unity, L_{ZF} is linked to the mode scale. In that case, the resonance between drift wave and zonal flow regulates the flow structure by modifying the local mode scale. In the hydrodynamic limit (i.e., $\tau_{ck} k_\parallel^2 D_\parallel \ll 1$), the generation and saturation of zonal flows must be reconsidered. The drift wave model discussed here is not directly applicable to the hydrodynamic case where convective cells, not drift waves, are generated.

The mixing length derived here allows us to calculate the scaling of turbulent diffusivity with $\rho_* \equiv \rho_s / L_n$. Following the mixing length model, the turbulent diffusivity scales as $D \sim l_{mix} v_*$, where $v_* \equiv \rho_s c_s / L_n$ is the electron drift velocity. Thus, we obtain $D \sim D_B l_{mix} / L_n$, where $D_B \sim \rho_s c_s$ is the Bohm diffusivity. When there is no zonal flow, the mixing length is the size of an extended cell, i.e., $l_{mix} \sim L_n$. This recovers the Bohm scaling, i.e., $D \sim D_B$. In the presence of zonal flow shear, the mixing length is larger than ρ_s, and thus gyro-Bohm scaling is a lower bound for turbulent diffusivity, i.e., $D > D_B \rho_*$. Hence, D lies between the gyro-Bohm and Bohm limits, i.e., $D \sim D_B \rho_*^\alpha$ where $0 < \alpha < 1$. The question is to determine α, i.e., the degree of gyro-Bohm breaking. The mixing length in the case of strong zonal flow shear is $l_{mix} \sim \rho_s^{1/4} l_0^{3/4} \sim$

$\rho_s^{1/4} L_n^{3/4}$. This indicates that the scaling of turbulent diffusivity is closer to the Bohm regime, i.e., $D \sim D_B l_{mix}/L_n \sim D_B \rho_*^{1/4} (l_0/L_n)^{3/4} \sim D_B \rho_*^{1/4}$. Therefore, the zonal flow shear leads to a gyro-Bohm correction to the diffusivity which is initially Bohm, absent flow shear. As a result, the diffusivity lies somewhere between Bohm and gyro-Bohm, but weighted more toward Bohm. Note the zonal flow shear here is determined self-consistently by considering shearing feedback on mixing length. Externally driven flow shears are not restricted by this self-consistent feedback mechanism. Thus, the external flow shear could make the diffusivity weighted more toward gyro-Bohm, i.e., $D \sim D_B \rho_*^{1/4+\beta}$ where $\beta > 0$ is induced by external shear. External shear reduces the mixing scale through the shearing feedback. Also, increasing external power input may lead to the formation of transport barriers[MAC$^+$11a]. The barriers can then reduce the mixing scale and thus can make the diffusivity more gyro-Bohm.

6.3.3 Extended Predator–Prey Model

The frictionless saturation induced by resonant PV mixing can be incorporated in the predator–prey model of the DW–ZF system. In this subsection, we show the derivation of this new, 0D model and compare the results with previous models. Note that even though the 0D model studied here is sufficient to demonstrate the flow and turbulence states as well as the flow scale, a model with at least one spatial dimension is necessary to study the spatiotemporal *dynamics* of the system, such as the formation of transport barriers.

Eq. (6.25) shows that in the frictionless regime, the net production of zonal field enstrophy is driven by the vorticity flux. Ignoring the evolution of $\langle n \rangle$, the total mean-field PE is related to the zonal vorticity through $V''^2 \sim \int dx \langle v_y \rangle'^2 / L_{ZF}^2 \equiv \int dx \langle \rho \rangle^2 / L_{ZF}^2$. The total fluctuation PE is $E \equiv \int dx \Omega$. Zonal flow is driven by the residual vorticity flux, but dissipated by the resonant scattering of zonal vorticity. Thus, the *net* mean-field PE is produced by $\langle \tilde{v}_x \tilde{\rho} \rangle V'' = \Gamma_\rho^{Res} V'' - D_q^{\mathrm{res}} V''^2 \sim \alpha_1 E |V''| - \alpha_2 V''^2 E$. Therefore, with frictional damping and nonlinear damping by tertiary instability included, the predator (flow) equation is

$$\frac{L_{ZF}^2}{2}\frac{dV''^2}{dt} = \alpha_1|V''|E - \alpha_2 V''^2 E - \gamma_{NL} V''^2 - \mu_c V''^2. \tag{6.30}$$

The vorticity flux conserves enstrophy between zonal field and fluctuations. Thus, the residual vorticity flux forms a *sink* of the fluctuation PE and the resonant vorticity diffusion forms a *source*. As a consequence, the prey (turbulence) equation can be written as

$$\frac{dE}{dt} = -\alpha_1|V''|E + \alpha_2 V''^2 E - \varepsilon_c E^{3/2} + \gamma_L E. \tag{6.31}$$

Here, baseline (i.e., without flow) nonlinear saturation of turbulence is through the forward cascade of PE. Ultimately, PE is dissipated by collisional diffusion at small scales. The linear growth of energy is due to the (linear) instability of fluctuations.

Eq. (6.30) and (6.31) form a new predator-prey model for the DW-ZF system. This model conserves PE and includes resonant PV mixing. The model is zero dimensional, because the quantities here have been integrated over space. Though the accuracy of this simplified 0D model is limited, we can use it to obtain useful insights. In this new model, the net flow production by turbulence consists of two terms, which are the turbulent production driven by residual stress and the dissipation induced by resonant diffusion.

Eq. (6.30) shows that in the frictionless regime, where the frictional drag $\mu_c \to 0$, the resonant vorticity diffusion saturates the zonal flow production, even without the nonlinear damping induced by tertiary instability. It should be stated that drift wave instability requires finite *electron* collisionality, while the frictional drag and collisional diffusion of particles and vorticity are both determined by *ion* collisionality and/or ion-neutral drag. Hence, flipping between frictional and frictionless regimes does not require a change in the drift wave drive.

The flow and energy states are set by the fixed points of the system, i.e. $dV''^2/dt = dE/dt = 0$. We ignore the nonlinear flow damping by tertiary instability, because it is irrelevant

Table 6.2: Flow states and turbulence states compared among regimes with different frictional damping rates. μ_c is the frictional drag coefficient, E is the turbulence energy (measured by fluctuation enstrophy), γ_L is the linear growth rate of turbulence, and α_1 and α_2 are coefficients in the predator–prey model resulting from residual vorticity flux and vorticity diffusion.

Regime	Frictionless	Weakly Frictional	Strongly Frictional
Frictional Damping Strength	$\mu_c \ll \alpha_2 E$	$\alpha_2 E \ll \mu_c \ll 4\gamma_L \alpha_1^2/\varepsilon_c^2$	$\mu_c \gg 4\gamma_L \alpha_1^2/\varepsilon_c^2$
Flow $\lvert V''\rvert$	$\frac{\alpha_1}{\alpha_2}$	$\frac{\alpha_1 \gamma_L^2}{\mu_c \varepsilon_c^2}$	$\frac{\gamma_L}{\alpha_1}$
Turbulence Energy E	$\frac{\gamma_L^2}{\varepsilon_c^2}$	$\frac{\gamma_L^2}{\varepsilon_c^2}$	$\frac{\gamma_L \mu_c}{\alpha_1^2}$

(usually). Therefore, the flow state can be obtained from Eq. (6.30), and is

$$|V''| = \frac{\alpha_1 E}{\alpha_2 E + \mu_c}. \tag{6.32}$$

We next discuss three regimes—the frictionless regime, the weakly frictional regime, and the strongly frictional regime—and compare results to those of previous models. In particular, we emphasize *what determines the turbulence level* and *what affects the flow* in near-marginal turbulence. The states of zonal vorticity and turbulence energy are summarized in Table 6.2. In the frictionless regime, the turbulence energy level is set only by the linear instability growth rate and the nonlinear dissipation of PE. This differs from the strongly frictional regime, where the turbulence level is set by the frictional drag[DLCT94].

Frictionless regime

In the frictionless regime, the drag is negligible compared to the resonant diffusive scattering of vorticity, i.e. $\mu_c \ll \alpha_2 E$. The flow and turbulence states are given by

$$|V''| = \alpha_1/\alpha_2, \tag{6.33}$$

$$E = (\gamma_L/\varepsilon_c)^2. \tag{6.34}$$

The flow is determined, to leading order, by the balance between residual vorticity flux (α_1) and diffusive mixing of vorticity (α_2). The turbulence energy is basically determined by the balance between linear growth rate and dissipation rate of PE (ε_c).

In the frictionless regime, turbulence energy is (approximately) independent of the flow state. The turbulence energy is determined only by the linear instability drive and the nonlinear dissipation of PE. The dissipation rate tied to forward cascade of potential enstrophy is $\sim \varepsilon_c \Omega^{1/2} \sim \varepsilon_c E^{1/2}$. The turbulence state is then set by the balance between the linear growth rate and the nonlinear dissipation rate, i.e. $\gamma_L \sim \varepsilon_c E^{1/2}$, yielding $E \sim (\gamma_L/\varepsilon_c)^2$. When the linear drive is weak, i.e. $\gamma_L/\varepsilon_c < 1$, the turbulence becomes marginal, with $E \ll 1$. This is different from previous results, where turbulence energy is set by the frictional flow damping. In previous models, below the onset threshold for tertiary instability, the flow is dissipated only by frictional drag. The energy is coupled from turbulence to flow, which is a one-way coupling. Therefore, the fixed point is set by the balance between the frictional flow damping and energy coupling, i.e., $\alpha V E \sim \mu_c V$, where α is the coupling coefficient between flow and turbulence energy. As a result, the saturated turbulence energy $E \sim \mu_c/\alpha$.

In addition, the saturated flow does not depend on the *turbulence level*, to leading order. The balance between residual vorticity flux and the resonant vorticity diffusion sets the flow. In this balance, the turbulence intensity cancels out. This means there can be significant zonal flow, even when the turbulence is weak. Therefore, this new frictionless saturation mechanism, induced by resonant PV mixing, is effective for turbulence near marginality. In previous models, the flow is set by the difference between linear growth of turbulence and frictional flow damping[DIIH05b]. Those models are not relevant to near-marginal turbulence, where $\gamma_L \to 0$.

Weakly frictional regime

When the drag exceeds the rate of turbulent diffusion, i.e. $\mu_c \gg \alpha_2 E$, the flow is linked to the turbulence strength, which is given by

$$|V''| = \alpha_1 E/\mu_c. \tag{6.35}$$

This follows because the flow is driven by turbulence, and collisions are the major source of flow damping. Thus, in the near marginal regime, both the turbulence and the flow becomes very weak, as the turbulence drive approaches zero.

The turbulence energy can be obtained from

$$\frac{\alpha_1^2 E}{\mu_c \gamma_L} + \frac{\varepsilon_c \sqrt{E}}{\gamma_L} - 1 = 0. \tag{6.36}$$

The exact solution is

$$E = \frac{\varepsilon_c^2 \mu_c^2}{2\alpha_1^4} \left[\sqrt{1 + \frac{4\gamma_L \alpha_1^2}{\varepsilon_c^2 \mu_c}} - 1 \right]. \tag{6.37}$$

Hence, in the weakly frictional regime, i.e. $\mu_c \ll 4\gamma_L \alpha_1^2/\varepsilon_c^2$, the turbulence energy is the same as in the frictionless case, while the flow is given by

$$|V''| = \frac{\alpha_1 \gamma_L^2}{\mu_c \varepsilon_c^2}. \tag{6.38}$$

We thus see that the weakly frictional regime is a hybrid of the frictionless and strongly frictional regimes. On one hand, the turbulence level is independent of flow damping, as for the frictionless regime. On the other hand, the flow depends on the turbulence level, meaning that when the turbulence is near marginal, the flow becomes very weak. This is because the turbulence driven flow production must be strong enough to overcome frictional damping, in order to drive a significant flow.

Strongly frictional regime

When the frictional flow damping is strong, i.e. in the strong frictional regime where $\mu_c \gg 4\gamma_L \alpha_1^2/\varepsilon_c^2$, the turbulence energy is set by the flow damping, which is given by

$$E = \gamma_L \mu_c / \alpha_1^2. \tag{6.39}$$

This recovers the scaling trends of previous predator-prey models. The flow is given by

$$|V''| = \gamma_L / \alpha_1. \tag{6.40}$$

Note that in this strongly frictional regime, the flow does not explicitly depend on frictional flow damping, which is the same as for previous results. The turbulence energy here is controlled by both the linear drive and the flow damping. As a consequence, the near-marginal state can be achieved by decreasing the linear forcing of the turbulence. As a result, with strong collisions, the flow is weak for near marginal turbulence.

The new predator–prey model presented here does not depend sensitively on the specific turbulence type. For comparison with the results calculated from the zonal vorticity equation, we now use drift wave instability as an example. The coefficients are

$$\alpha_1 = \frac{k_y^2 \rho_s c_s}{L_n} \left(\tau_{ck} - \frac{1}{k_\parallel^2 D_\parallel} \frac{k_y^2 \rho_s^2 + L_m^{-2} \rho_s^2}{1 + k_y^2 \rho_s^2 + L_m^{-2} \rho_s^2} \right), \tag{6.41}$$

$$\alpha_2 = k_y^2 \rho_s^2 \tau_{ck}. \tag{6.42}$$

As a result, in the frictionless regime, the stationary zonal vorticity emerges as

$$|V''| = \frac{\alpha_1}{\alpha_2} = \frac{c_s}{\rho_s L_n} \left(1 - \frac{1}{\tau_{ck} k_\parallel^2 D_\parallel} \frac{k_y^2 \rho_s^2 + L_m^{-2} \rho_s^2}{1 + k_y^2 \rho_s^2 + L_m^{-2} \rho_s^2} \right), \tag{6.43}$$

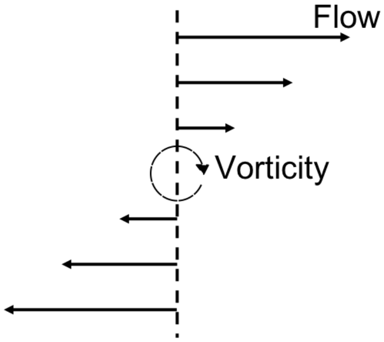

Figure 6.4: For zonal flows, vorticity is equal to flow shear.

which is consistent with Eq. (6.26). Vorticity gradient measures the jump across the flow shear field. Thus, the ZF profile can be deduced from the zonal vorticity by specifying boundary conditions. As shown by Fig. 6.4, for zonal flows, vorticity is equal to shear, which is of greater interest than the flow velocity.

6.4 Discussion

In this paper, we study how wave–flow resonance affects the linear stability of drift wave turbulence, and how it regulates zonal flow saturation in the frictionless regime by resonant vorticity mixing. The main results of this paper are:

- Resonance stabilizes drift waves due to wave absorption. Counter-intuitively, flow shear can destabilize drift wave by weakening the resonance. This contradicts the conventional wisdom of shearing effects.
- Resonance opens a new channel of zonal flow saturation, absent frictional drag, through the irreversible turbulent mixing of vorticity. The scale of the stationary flow that forms is mesoscopic, but weighted somewhat more strongly toward microscale than macroscale. We show directly from analysis that the zonal flow scale is $L_{ZF} \sim f^{3/16}(1-f)^{1/8}\rho_s^{5/8}l_0^{3/8}$ in the relevant adiabatic regime (i.e., $\tau_{ck}k_{\parallel}^2 D_{\parallel} \gg 1$). The flow shear scales as $|\langle v_y \rangle'| \sim$

$f^{3/16}(1-f)^{1/8}\frac{c_s}{L_n}\left(\frac{l_0}{\rho_s}\right)^{3/8}$.

- We calculate the degree of gyro-Bohm breaking and show that the resulting turbulent diffusivity is closer to the Bohm limit, i.e., $D \sim D_B \rho_*^{1/4}(l_0/L_n)^{3/4} \sim D_B \rho_*^{1/4}$. The base state mixing length, absent flow shear, is $l_0 \sim L_n$.

- We incorporate the saturation by mixing of vorticity into the predator–prey model. In contrast to previous results, the saturated flow is independent of the turbulence level, to leading order, in the frictionless regime. Thus, it can be significant for the relevant case of near-marginal turbulence. The turbulence energy is determined by the balance of linear drive and nonlinear dissipation without involving flow damping, and gives $E \sim \gamma_L^2/\varepsilon_c^2$.

In the presence of strong resonance, flow shear can linearly destabilize the drift wave turbulence, which is opposite to what the conventional shear suppression models predict. Resonance suppresses the instability as a result of wave absorption, and the flow shear can weaken the resonance. Therefore, wave-flow resonance is an important factor to be considered when studying the shear flow effect on stability, and on quasilinear fluxes that transport particle, vorticity, and momentum.

The Dimits up-shift regime spans low to zero collisionality and consists of weak turbulence near marginality. ZF saturation induced by resonant PV mixing is effective in both the frictionless regime and for near-marginal turbulence, and thus is compatible with the physics of the Dimits up-shift regime. Resonance regulates ZF saturation in the frictionless regime without the need to invoke tertiary instability. The saturated flow does *not* depend on the turbulence intensity. Hence, there can be significant zonal flows for near-marginal turbulence, absent frictional damping.

The stationary flow profile is determined by the balance between residual vorticity flux and the resonant diffusivity of vorticity. While ZF scale is often *assumed*, the new model discussed here *calculates* the saturated flow scale in the frictionless limit. In the limiting case with near-adiabatic electrons (i.e., $\tau_{ck}k_{\|}^{2}D_{\|} \gg 1$), the ZF scale is mesoscopic, i.e., $L_{ZF} \sim f^{3/16}(1-f)^{1/8}\rho_s^{5/8}l_0^{3/8}$, in accordance with conventional assumptions. The mixing length regulated by the zonal flow shear is then $l_{mix} \sim \rho_s^{1/4}l_0^{3/4} \sim \rho_s^{1/4}L_n^{3/4}$. This implies a Bohm-like scaling of turbulent diffusivity, i.e. $D \sim D_B l_{mix}/L_n \sim D_B\rho_*^{1/4}(l_0/L_n)^{3/4} \sim D_B\rho_*^{1/4}$, where D_B is the Bohm diffusivity and $\rho_* \equiv \rho_s/L_n$. Note that absent zonal flow shear, the scaling is purely Bohm, i.e., $l_{mix} \sim l_0 \sim L_n$ and $D \sim D_B$. As a result of zonal flow shear, the diffusivity scaling exhibits a gyro-Bohm correction, but weighted more toward Bohm. The scaling takes into account zonal flow shears that are self-consistently determined by shearing feedback on mixing length. Thus, externally driven flow shear may be needed to achieve scalings that are more gyro-Bohm. The flow shear driven by external power sources can reduce the mixing scale through shearing feedback. In addition, increasing the external power input can lead to the formation of transport barriers[MAC$^+$11a]. The transport barrier so formed could also reduce the mixing scale and thus could make the diffusivity weighted more toward gyro-Bohm.

We have derived an extended predator–prey model, incorporating the resonant PV mixing process. This new model is effective in the near-marginal turbulence. Thus, it can describe zonal flow saturation in the Dimits up-shift regime. In the frictionless regime, the resonant diffusion of vorticity leads to nonlinear saturation of zonal flow. The turbulence energy is saturated by nonlinear enstrophy dissipation tied to forward cascade of potential enstrophy. As a result, the turbulence energy scales with the linear forcing rate as $E \sim \gamma_L^2$. The saturated flow does *not* depend on the turbulence intensity. Hence, there can be significant flows in near-marginal turbulence. Therefore, frictionless ZF saturation by resonant PV mixing is expected to be effective in weak turbulence regimes. In the frictional regime with significant frictional flow damping, the dependence of turbulence energy level on flow damping is recovered. The flow is driven by turbulence, while saturated by collisions. Hence, in this limit, the flow is very weak in near-marginal turbulence.

The model discussed here addresses the long-standing question of “how close is ‘close’” in near-marginal systems. It is effective in both near-marginal turbulence and in the frictionless regime. Thus, when expanded to *1D*, it can be used to study avalanches and staircase formation[DPDG$^+$10, NCDH96]. In 1D, avalanching induces variability of profiles, and thus of local growth rates. The scaling $E \sim \gamma_L^2$ suggests a variability-dominated state can result when $\gamma_L \to 0$. This follows because γ_L has an exponent > 1, which holds true as long as the self-saturation of fluctuation PE exhibits the dependence $\varepsilon_c \Omega^{1+p}$, where $0 < p < 1$. Thus, the scaling of E with γ_L is stronger than the conventional weak turbulence result. The local linear growth rate is then set by both equilibrium (mean) and variable (i.e., avalanche-induced) profile gradients, i.e., $\gamma_L = \bar{\gamma}_L + \tilde{\gamma}_L$. As a result of resonant PV mixing in the frictionless regime, the turbulence state is determined by $E \sim \gamma_L^2 \sim \bar{\gamma}_L^2 + \tilde{\gamma}_L^2$. $\bar{\gamma}_L$ is determined by the difference between mean profile gradient and critical gradient. In near-marginal turbulence, the mean gradient approaches the critical gradient, so $\bar{\gamma}_L \to 0$. Thus, there the turbulence state is primarily controlled by noise from avalanche variability, i.e., $E \sim \tilde{\gamma}_L^2 \gg \bar{\gamma}_L^2$. Such noise is produced by avalanching, which stochastically modulates the driving gradient. In this case, the predator–prey model must be treated as a set of coupled stochastic differential equations. In 1D, the relevant system is a nonlinear reaction–diffusion model like that of Eq. (6.22) and (6.23), including multiplicative noise. The results in this work thus define the boundary for "marginality". The turbulence energy scales with the dimensionless ratio $(\gamma_L/\varepsilon_c)^2$, where ε_c is the dissipation rate of PE. Therefore, the turbulence can be "marginal" when the equilibrium growth rate $\bar{\gamma}_L < \varepsilon_c$. This gives a basis upon which to define the extent of the "near-marginal regime".

Chapter 6 has been submitted for publication of the material as it may appear in J. C. Li and P. H. Diamond, "Another look at zonal flow physics: resonance, shear flows and frictionless saturation", *Physics of Plasmas* (2018), American Institute of Physics. The dissertation author was the primary investigator and author of this article.

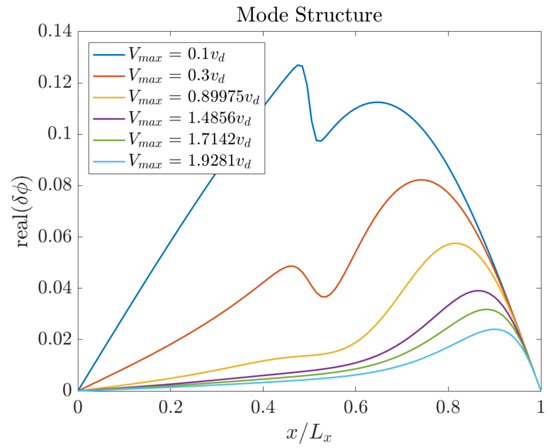

Figure 6.5: Mode structure for various flow magnitudes, with fixed flow shear. The flow is given by function $V_y = V_{max}\tanh\left[(x - 0.5L_x)/L_V\right]$.

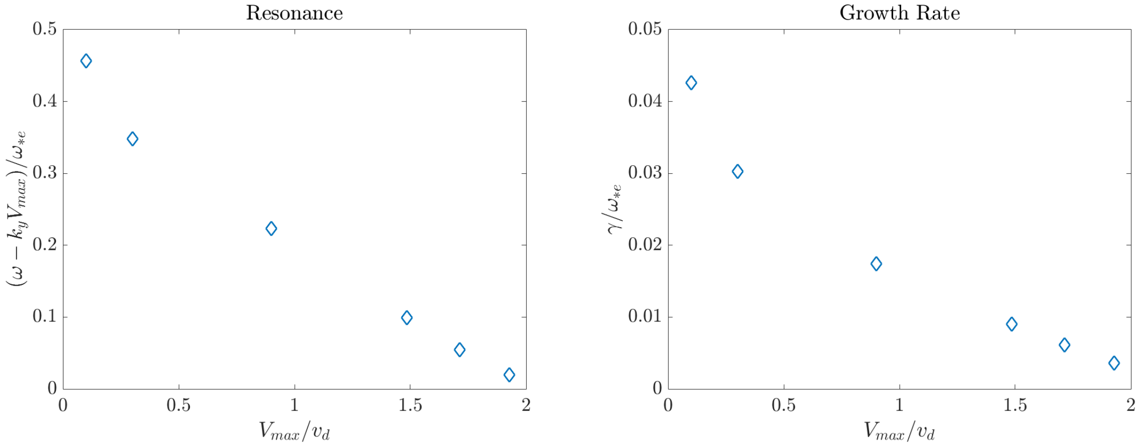

Figure 6.6: Resonance (left) and growth rate (right) vs. flow magnitude, with fixed shear. The flow is given by function $V_y = V_{max}\tanh\left[(x - 0.5L_x)/L_V\right]$.

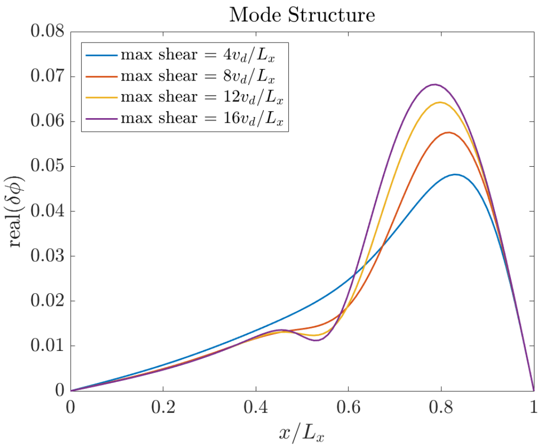

Figure 6.7: Mode structure for various flow shears, with fixed flow amplitude. The flow is given by function $V_y = V_{max}\tanh[(x - 0.5L_x)/L_V]$.

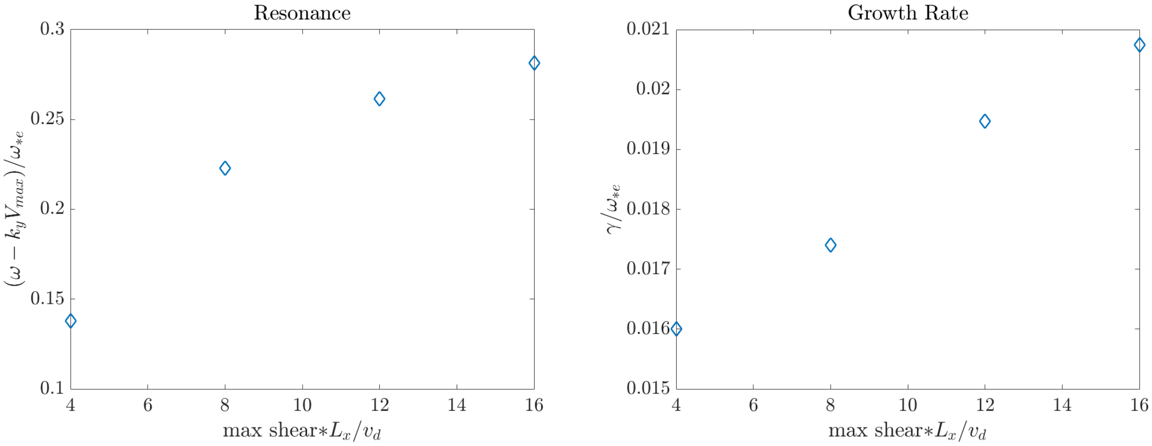

Figure 6.8: Resonance (left) and growth rate (right) vs. flow shear, with fixed magnitude. The flow is given by function $V_y = V_{max}\tanh[(x - 0.5L_x)/L_V]$.

Chapter 7

Summary and Future Directions

In this dissertation, we have studied the fundamental issues of intrinsic axial and azimuthal flows and their interaction with each other in a linear device absent magnetic shear. We sought to answer the following questions:

1. What breaks the $k_{\parallel}$ spectral symmetry of turbulence and thus generates intrinsic parallel flows, absent magnetic shear? (Chapter 2)
2. What saturates the axial flows and determines the profile stiffness of flow shear? (Chapter 3)
3. How to demonstrate, in experiments, the causal link from the density gradient to spectral asymmetry of drift wave turbulence, and the development of mean axial flow? (Chapter 5)
4. How does wave–flow resonance regulate the stability of drift wave turbulence and the saturation of zonal flow in the frictionless regime? (Chapter 6)

In Chapter 2, we develop a new dynamical symmetry breaking mechanism for the generation of intrinsic axial flows in uniform magnetic fields. In a simple drift wave system, a seed axial flow shear can be self-amplifying. The seed flow shear breaks the spectral symmetry by setting the growth rate of some modes higher than that of the others. The resulting spectral imbalance gives rise to a finite residual stress $\Pi_{rz}^{\mathrm{Res}} \sim \langle k_\theta k_z \rangle$. This residual stress induces a negative increment to the turbulent viscosity. When the negative viscosity increment induced by residual stress overcomes the turbulence viscosity set by drift waves, such that the total viscosity becomes negative, the flow shear is amplified by the modulational instability. When the axial flow shear exceeds $\langle v_z \rangle'_{\mathrm{crit}}$ and triggers PSFI, the additional turbulent viscosity by PSFI nonlinearly saturates the $\langle v_z \rangle'$ growth. The flow profile will then be relaxed by $\chi_\phi^{\mathrm{PSFI}}$. Hence, the axial flow shear will stay at or below the PSFI threshold $\langle v_z \rangle'_{\mathrm{crit}}$.

In Chapter 3, we investigate the physics of negative viscosity in ITG turbulence and discuss the axial flow shear stiffness when plotted vs. ∇T_i. The negative viscosity increment induced by residual stress is not limited in the drift wave turbulence. We have shown that pure ITG turbulence cannot drive intrinsic flows in a straight magnetic field, but can induce a negative viscosity increment, which reduces the turbulent flow dissipation.

We also study the stiffness of $\nabla V_\parallel$ profile plotted vs. ∇T_{i0}. PSFI saturates the flow gradient, when $\nabla V_\parallel$ is driven above the PSFI regime boundary. The flow gradient saturates at the PSFI regime boundary, which is above the PSFI linear threshold and tracks the ITG drive, i.e. $\nabla V_\parallel / |k_\parallel c_s| \sim (\nabla T_{i0})^{2/3} / (k_\parallel T_{i0})^{2/3}$ The flow gradient in CSDX can be enhanced by various external sources. When $\nabla V_\parallel$ steepens enough, so that PSFI drive dominates over ITG drive, flow gradient saturates by PSFI relaxation. PSFI is nonlinear in $\nabla V_\parallel$, and so is the viscosity driven by PSFI turbulence. Consequently, $\nabla V_\parallel$ saturates at the boundary between PSFI regime and ITG regime (which is above the linear PSFI threshold) and grows as $\nabla V_\parallel \sim (\nabla T_{i0})^{2/3}$. This scaling of flow gradient implies a generalized Rice-type scaling, i.e. $\nabla V_\parallel \sim (\nabla T_{i0})^\alpha$, with $\alpha = 2/3$.

In Chapter 4, we study the interaction of intrinsic azimuthal and axial flows in CSDX. In particular, we have studied how incremental changes of flow shears affect the production branching ratio P_z^R / P_y^R. We have also investigated the effects of azimuthal flow shear on intrinsic axial flow generation and saturation, absent magnetic shear. We have found increasing azimuthal flow shear reduces the branching ratio, which is measured by the ratio of axial and azimuthal Reynolds powers, i.e., P_z^R/P_y^R. When axial flow shear increases, P_z^R/P_y^R first increases and then decreases. This turnover occurs below PSFI threshold. Azimuthal flow shear stabilizes drift waves by weakening the ∇n_0 drive, i.e., reducing the ω_{*e} by the amount $|k_y\rho_s^2\langle v_y\rangle''|$. Azimuthal flow shear slows down the modulational growth of seed axial flow shear, and thus reduces the production of intrinsic axial flow, absent magnetic shear. Azimuthal flow shear reduces both axial residual stress (Π_{xz}^{Res}) and turbulent viscosity driven by drift waves (χ_z^{DW}) by the same factor, i.e., both Π_{xz}^{Res} and χ_z^{DW} scale with the azimuthal flow shear as $|V'|^{-2} \sim |\langle v_y\rangle'|^{-2}\Delta_x^{-2}L_n^{-2}\rho_s^2c_s^2$. However, azimuthal flow shear does not affect the saturated axial flow shear to leading order, because $\langle v_z\rangle' = \Pi_{xz}^{Res}/\chi_z^{DW}$ and the reduction by $\langle v_y\rangle'$ cancels.

Chapter 5 discusses the phenomenology of axial and azimuthal flow dynamics in drift wave turbulence in CSDX. We haven shown, by measurement, the pathway of free energy source → turbulence → symmetry breaking → residual Reynolds stress → intrinsic axial flow shear. The interaction between axial and azimuthal flows is weak. A plausible physical picture of the system of flows and turbulence discussed in this thesis is summarized in Fig. 7.1. In this study, the axial Reynolds power is smaller than the azimuthal one by an order of magnitude. Thus, the azimuthal flow-turbulence interaction is the primary branch in the turbulence-flow system. The axial mean flow is then parasitic to such system, and is driven by the residual stress. The azimuthal flow shearing rate is much less than the drift wave frequency, so the residual stress decouples from the effect of azimuthal flow (dashed line in Fig. 7.1). This axial residual stress results from a dynamical symmetry breaking mechanism, i.e., driven by drift wave turbulence with broken symmetry in **k**-space. This spectral imbalance in $\langle k_z k_\theta\rangle$ is induced by the seed axial flow shear, which is in turn amplified by the axial residual stress. These observations are consistent with the causal link proposed by the heat engine model, i.e., a pathway from symmetry breaking to the development of residual stress and the onset of axial mean flow.

Although the axial–azimuthal flow coupling appears to be weak in this study, it needs not

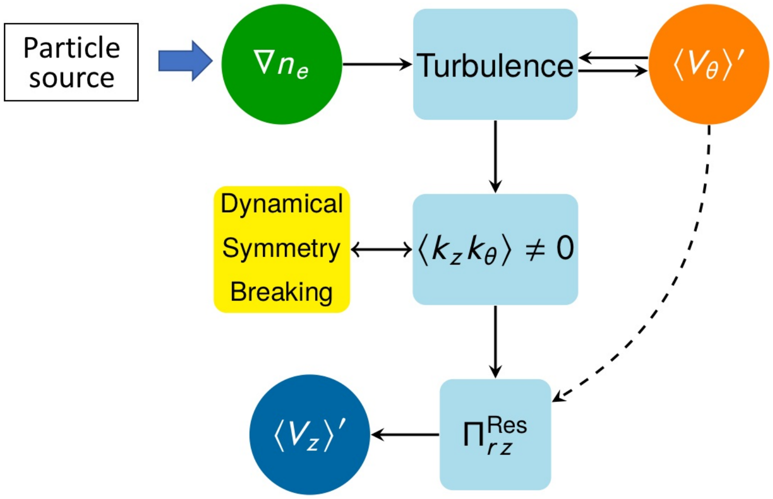

Figure 7.1: The present—a pathway from drift wave turbulence with broken symmetry to the development of residual stress and the onset of axial mean flow in CSDX.

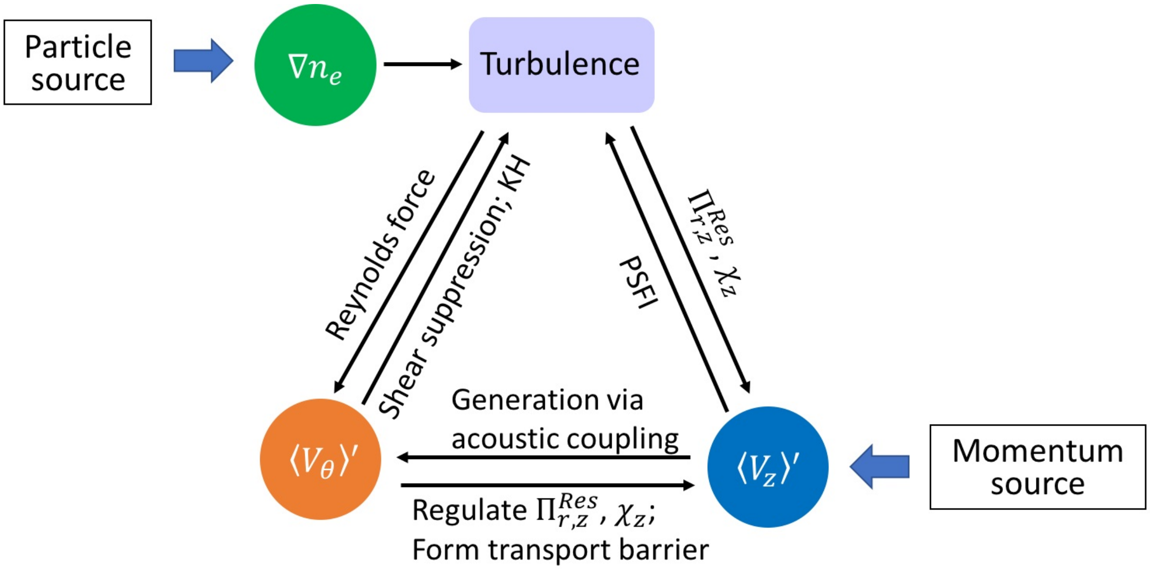

Figure 7.2: The future—a diagram of hypothesized turbulence–flow interaction in CSDX with both axial momentum and particle sources. Here, PSFI is the abbreviation for parallel shear flow instability.

always be so. There are at least two ways to enhance the interaction between axial and azimuthal flows in CSDX. The proposed mechanisms are illustrated in Fig. 7.2. One way is to increase the power of the plasma source, such that ∇n drives stronger drift wave turbulence and thus leads to enhanced zonal flows via the Reynolds force. When the zonal flow shear is comparable to drift wave frequency, it will regulate the axial flow production and dissipation by entering explicitly–and reducing–the axial residual stress and turbulent diffusivity. The enhanced zonal flow shear will then increase the axial flow shear by reducing the cross-field momentum transport, i.e., thus forming a transport barrier.

The other way to enhance the coupling between axial and azimuthal flows is to increase the parallel momentum source. The enhanced axial flow can increase the zonal flow production via the acoustic coupling. [WDH12a] The parallel flow compression can be converted to zonal flow by coupling with potential vorticity (PV) fluctuations. This coupling, i.e., $\langle \tilde{q} \nabla_{\|} \tilde{v}_{\|} \rangle$, breaks PV conservation, and thus forms a source for zonal flow. This conversion occurs when parallel flow compression is significant, especially near the PSFI threshold. With increased axial and azimuthal flow shears, a transport barrier can be formed by increasing the axial momentum source. CSDX will be equipped with an axial gas-puff system that provides an axial momentum source. The axial flow then can also be driven by a strong axial momentum source, and thus V_z would be adjustable within a wide range. In our current experiments, the peak value of the axial Mach number is about 0.2, which is well below the PSFI threshold. The upgraded system will present us an opportunity to investigate the role of PSFI in parallel flow saturation as well as axial-azimuthal flow coupling.

To summarize, we remark that CSDX offers an excellent venue to study the detailed physics of transport barrier formation with turbulent-driven transverse and parallel shear flows at zero magnetic shear. In tokamaks, it has been observed that coexistence of large toroidal rotation and low magnetic shear, i.e., flat-q regime, leads to enhanced confinement states, and profile "de-stiffening".[MAC$^+$11b] This regime is under intensive study in the magnetic fusion energy community, and it is worthwhile to note that basic experiments can produce substantial insights into the relevant physics.

In Chapter 6, we study how wave–flow resonance affects the linear stability of drift wave turbulence, and how it regulates zonal flow saturation in the frictionless regime by resonant vorticity mixing. Resonance stabilizes drift waves due to wave absorption. Flow shear can destabilize drift wave by weakening the resonance. This *contradicts* the conventional wisdom of shearing effects. The resonance opens a new channel of zonal flow saturation, absent frictional drag, through the turbulent mixing of vorticity. The scale of the stationary flow that forms is mesoscopic, but weighed somewhat more strongly toward the microscale than the macroscale. We show directly from analysis that the zonal flow scale is $L_{ZF} \sim f^{3/16}(1-f)^{1/8}\rho_s^{5/8} l_0^{3/8}$ in the relevant adiabatic regime (i.e., $\tau_{ck} k_\parallel^2 D_\parallel \gg 1$). We calculate the degree of gyro-Bohm breaking and show that the resulting turbulent diffusivity is closer to the Bohm limit, i.e., $D \sim D_B \rho_*^{1/4}$. This new saturation mechanism has been incorporated in the predator–prey model. In contrast to previous results, the saturated flow is independent of the turbulence level in the frictionless regime. Thus, it can be significant for the relevant case of near-marginal turbulence. The turbulence energy is determined by the balance of linear drive and nonlinear dissipation without involving flow damping, and with $E \sim \gamma_L^2/\varepsilon_c^2$.

Bibliography

[ACC+12] C Angioni, Y Camenen, F J Casson, E Fable, R M McDermott, A G Peeters, and J E Rice. *Nuclear Fusion*, 52(11):114003, 2012.

[AD16] Arash Ashourvan and P. H. Diamond. How mesoscopic staircases condense to macroscopic barriers in confined plasma turbulence. *Phys. Rev. E*, 94:051202, Nov 2016.

[AD17] Arash Ashourvan and P. H. Diamond. On the emergence of macroscopic transport barriers from staircase structures. *Physics of Plasmas*, 24(1):012305, 2017.

[ADG16] Arash Ashourvan, P H Diamond, and ÖD Gürcan. Transport matrix for particles and momentum in collisional drift waves turbulence in linear plasma devices. *Physics of Plasmas*, 23(2):022309, 2016.

[AGG+13] J Abiteboul, Ph Ghendrih, V Grandgirard, T Cartier-Michaud, G Dif-Pradalier, X Garbet, G Latu, C Passeron, Y Sarazin, A Strugarek, O Thomine, and D Zarzoso. Turbulent momentum transport in core tokamak plasmas and penetration of scrape-off layer flows. *Plasma Physics and Controlled Fusion*, 55(7):074001, 2013.

[BDT90] H. Biglari, P. H. Diamond, and P. W. Terry. Influence of sheared poloidal rotation on edge turbulence. *Physics of Fluids B: Plasma Physics*, 2(1):1–4, 1990.

[BTA+05] M. J. Burin, G. R. Tynan, G. Y. Antar, N. A. Crocker, and C. Holland. On the transition to drift turbulence in a magnetized plasma column. *Physics of Plasmas*, 12(5):052320, 2005.

[CAT+16] L. Cui, A. Ashourvan, S. C. Thakur, R. Hong, P. H. Diamond, and G. R. Tynan. *Physics of Plasmas*, 23:055704, 2016.

[CGDS17] Haihong Che, Melvyn L. Goldstein, Patrick H. Diamond, and Roald Z. Sagdeev. How electron two-stream instability drives cyclic langmuir collapse and continuous coherent emission. *Proceedings of the National Academy of Sciences*, 114(7):1502–1507, 2017.

[Cha48] Jule G Charney. On the scale of atmospheric motions. *Geofysiske Publikasjoner*, 17(2), 1948.

[CSD$^+$92] B. A. Carreras, K. Sidikman, P. H. Diamond, P. W. Terry, and L. Garcia. Theory of shear flow effects on longwavelength drift wave turbulence. *Physics of Fluids B: Plasma Physics*, 4(10):3115–3131, 1992.

[DIIH05a] P H Diamond, S-I Itoh, K Itoh, and T S Hahm. Zonal flows in plasma–a review. *Plasma Physics and Controlled Fusion*, 47(5):R35, 2005.

[DIIH05b] P H Diamond, S I Itoh, K Itoh, and T S Hahm. Zonal flows in plasmaa review. *Plasma Physics and Controlled Fusion*, 47(5):R35, 2005.

[DK91] P. H. Diamond and Y.B. Kim. Theory of mean poloidal flow generation by turbulence. *Physics of Fluids B: Plasma Physics*, 3(7):1626–1633, 1991.

[DKG$^+$13a] P. H. Diamond, Y. Kosuga, Ö. D. Gürcan, C. J. McDevitt, T. S. Hahm, N. Fedorczak, J. E. Rice, W. X. Wang, S. Ku, J. M. Kwon, G. Dif-Pradalier, J. Abiteboul, L. Wang, W. H. Ko, Y. J. Shi, K. Ida, W. Solomon, H. Jhang, S. S. Kim, S. Yi, S. H. Ko, Y. Sarazin, R. Singh, and C. S. Chang. An overview of intrinsic torque and momentum transport bifurcations in toroidal plasmas. *Nuclear Fusion*, 53(10):104019, 2013.

[DKG$^+$13b] P.H. Diamond, Y. Kosuga, Ö.D. Gürcan, C.J. McDevitt, T.S. Hahm, N. Fedorczak, J.E. Rice, W.X. Wang, S. Ku, J.M. Kwon, G. Dif-Pradalier, J. Abiteboul, L. Wang, W.H. Ko, Y.J. Shi, K. Ida, W. Solomon, H. Jhang, S.S. Kim, S. Yi, S.H. Ko, Y. Sarazin, R. Singh, and C.S. Chang. An overview of intrinsic torque and momentum transport bifurcations in toroidal plasmas. *Nuclear Fusion*, 53(10):104019, 2013.

[DLCT94] P. H. Diamond, Y.-M. Liang, B. A. Carreras, and P. W. Terry. Self-regulating shear flow turbulence: A paradigm for the l to h transition. *Phys. Rev. Lett.*, 72:2565–2568, Apr 1994.

[DPDG$^+$10] G. Dif-Pradalier, P. H. Diamond, V. Grandgirard, Y. Sarazin, J. Abiteboul, X. Garbet, Ph. Ghendrih, A. Strugarek, S. Ku, and C. S. Chang. On the validity of the local diffusive paradigm in turbulent plasma transport. *Phys. Rev. E*, 82:025401, Aug 2010.

[dRB$^+$07] J. S. deGrassie, J. E. Rice, K. H. Burrell, R. J. Groebner, and W. M. Solomon. Intrinsic rotation in diii-d. *Physics of Plasmas*, 14(5):056115, 2007.

[dVRG$^+$06] P C de Vries, K M Rantamki, C Giroud, E Asp, G Corrigan, A Eriksson, M de Greef, I Jenkins, H C M Knoops, P Mantica, H Nordman, P Strand, T Tala, J Weiland, K-D Zastrow, and JET EFDA Contributors. Plasma rotation and momentum transport studies at jet. *Plasma Physics and Controlled Fusion*, 48(12):1693, 2006.

[DWBC96] A. M. Dimits, T. J. Williams, J. A. Byers, and B. I. Cohen. Scalings of ion-temperature-gradient-driven anomalous transport in tokamaks. *Phys. Rev. Lett.*, 77:71–74, Jul 1996.

[GBH$^+$01] X. Garbet, C. Bourdelle, G. T. Hoang, P. Maget, S. Benkadda, P. Beyer, C. Figarella, I. Voitsekovitch, O. Agullo, and N. Bian. Global simulations of ion turbulence with magnetic shear reversal. *Physics of Plasmas*, 8:2793, 2001.

[GD15] Ö D Gürcan and P H Diamond. Zonal flows and pattern formation. *Journal of Physics A: Mathematical and Theoretical*, 48(29):293001, 2015.

[GD16] Z. B. Guo and P. H. Diamond. Zonal flow patterns: How toroidal coupling induces phase jumps and shear layers. *Phys. Rev. Lett.*, 117:125002, Sep 2016.

[GDH$^+$10a] Ö. D. Gürcan, P. H. Diamond, P. Hennequin, C. J. McDevitt, X. Garbet, and C. Bourdelle. Residual parallel reynolds stress due to turbulence intensity gradient in tokamak plasmas. *Physics of Plasmas*, 17(11), 2010.

[GDH$^+$10b] Ö. D. Gürcan, P. H. Diamond, P. Hennequin, C. J. McDevitt, X. Garbet, and C. Bourdelle. Residual parallel reynolds stress due to turbulence intensity gradient in tokamak plasmas. *Physics of Plasmas*, 17(11):112309, 2010.

[GDHS07a] Ö. D. Gürcan, P H Diamond, T S Hahm, and R Singh. Intrinsic rotation and electric field shear. *Physics of Plasmas (1994-present)*, 14(4):042306, 2007.

[GDHS07b] Ö. D. Gürcan, P. H. Diamond, T. S. Hahm, and R. Singh. Intrinsic rotation and electric field shear. *Physics of Plasmas*, 14(4):042306, 2007.

[GHD15] Z. B. Guo, T. S. Hahm, and P. H. Diamond. Small scale coherent vortex generation in drift wave-zonal flow turbulence. *Physics of Plasmas*, 22(12):122304, 2015.

[GHP$^+$06] B. Gonalves, C. Hidalgo, M. A. Pedrosa, R. O. Orozco, E. Sánchez, and C. Silva. Role of turbulence on edge momentum redistribution in the tj-ii stellarator. *Phys. Rev. Lett.*, 96:145001, Apr 2006.

[GSG$^+$02] X. Garbet, Y. Sarazin, P. Ghendrih, S. Benkadda, P. Beyer, C. Figarella, and I. Voitsekhovitch. Turbulence simulations of transport barriers with toroidal velocity. *Physics of Plasmas*, 9:3893, 2002.

[GSJ$^+$02] A. M. Garofalo, E. J. Strait, L. C. Johnson, R. J. La Haye, E. A. Lazarus, G. A. Navratil, M. Okabayashi, J. T. Scoville, T. S. Taylor, and A. D. Turnbull. Sustained stabilization of the resistive-wall mode by plasma rotation in the diii-d tokamak. *Phys. Rev. Lett.*, 89:235001, Nov 2002.

[GSSS77] AA Galeev, RZ Sagdeev, VD Shapiro, and VI Shevchenko. Langmuir turbulence and dissipation of high frequency energy. *Zhurnal Eksperimental'noi i Teoreticheskoi Fiziki*, 73:1352–1369, 1977.

[HDAT17] R. J. Hajjar, P. H. Diamond, A. Ashourvan, and G. R. Tynan. Modelling enhanced confinement in drift-wave turbulence. *Physics of Plasmas*, 24(6):062106, 2017.

[HDGR07] T. S. Hahm, P. H. Diamond, Ö. D. Gürcan, and G. Rewoldt. Nonlinear gyrokinetic theory of toroidal momentum pinch. *Physics of Plasmas*, 14(7):072302, 2007.

[HDT] R. Hajjar, P. H. Diamond, and G. R. Tynan. The ecology of flows and drift wave turbulence in csdx: a model. *submitted to Physics of Plasmas*.

[HLH+18] R. Hong, J. C. Li, R. Hajjar, S. Chakraborty Thakur, P. H. Diamond, and G. R. Tynan. Generation of parasitic axial flow by drift wave turbulence with broken symmetry: Theory and experiment. *submitted to Physics of Plasmas*, 2018.

[HLT+16] R. Hong, J. C. Li, S. C. Thakur, P. H. Diamond, and G. R. Tynan. *2016 US Transport Task Force Workshop, Denver, CO*, 2016.

[Hut08] I. H. Hutchinson. Ion collection by oblique surfaces of an object in a transversely flowing strongly magnetized plasma. *Phys. Rev. Lett.*, 101:035004, Jul 2008.

[HW83] Akira Hasegawa and Masahiro Wakatani. Plasma edge turbulence. *Physical Review Letters*, 50(9):682, 1983.

[HYJ+06] C. Holland, J. H. Yu, A. James, D. Nishijima, M. Shimada, N. Taheri, and G. R. Tynan. Observation of turbulent-driven shear flow in a cylindrical laboratory plasma device. *Phys. Rev. Lett.*, 96:195002, May 2006.

[IKK+16] S. Inagaki, T. Kobayashi, Y. Kosuga, S.-I. Itoh, T. Mitsuzono, Y. Nagashima, H. Arakawa, T. Yamada, Y. Miwa, N. Kasuya, M. Sasaki, M. Lesur, A. Fujisawa, and K. Itoh. A concept of cross-ferroic plasma turbulence. *Scientific Reports*, 6:22189, 2016.

[IMM+95] K. Ida, Y. Miura, T. Matsuda, K. Itoh, S. Hidekuma, and S. I. Itoh. Evidence for a toroidal-momentum-transport nondiffusive term from the jft-2m tokamak. *Phys. Rev. Lett.*, 74:1990–1993, Mar 1995.

[IR14] K. Ida and J.E. Rice. Rotation and momentum transport in tokamaks and helical systems. *Nuclear Fusion*, 54(4):045001, 2014.

[KD02] Eun-Jin Kim and P. H. Diamond. Dynamics of zonal flow saturation in strong collisionless drift wave turbulence. *Physics of Plasmas*, 9(11):4530–4539, 2002.

[KDG10a] Y. Kosuga, P. H. Diamond, and Ö. D. Gürcan. On the efficiency of intrinsic rotation generation in tokamaks. *Physics of Plasmas*, 17(10), 2010.

[KDG10b] Y. Kosuga, P. H. Diamond, and Ö. D. Gürcan. On the efficiency of intrinsic rotation generation in tokamaks. *Physics of Plasmas*, 17(10):102313, 2010.

[KGD15] Sumire Kobayashi, Ö. D. Gürcan, and Patrick H. Diamond. Direct identification of predator-prey dynamics in gyrokinetic simulations. *Physics of Plasmas*, 22(9):090702, 2015.

[KII15] Y. Kosuga, S. I. Itoh, and K. Itoh. Density peaking by parallel flow shear driven instability in panta. *Plasma Fusion Research*, 10:3401024, 2015.

[KIK$^+$16] T. Kobayashi, S. Inagaki, Y. Kosuga, M. Sasaki, Y. Nagashima, T. Yamada, H. Arakawa, N. Kasuya, A. Fujisawa, S.-I. Itoh, and K. Itoh. Structure formation in parallel ion flow and density profiles by cross-ferroic turbulent transport in linear magnetized plasma. *Physics of Plasmas*, 23(10):102311, 2016.

[Law57] John D Lawson. Some criteria for a power producing thermonuclear reactor. *Proceedings of the Physical Society. Section B*, 70(1):6, 1957.

[LDXT16a] J. C. Li, P. H. Diamond, X. Q. Xu, and G. R. Tynan. Dynamics of intrinsic axial flows in unsheared, uniform magnetic fields. *Physics of Plasmas*, 23(5):052311, 2016.

[LDXT16b] J. C. Li, P. H. Diamond, X. Q. Xu, and G. R. Tynan. Dynamics of intrinsic axial flows in unsheared, uniform magnetic fields. *Physics of Plasmas*, 23(5):052311, 2016.

[LRH$^+$05] B. LaBombard, J. E. Rice, A. E. Hubbard, J. W. Hughes, M. Greenwald, R. S. Granetz, J. H. Irby, Y. Lin, B. Lipschultz, E. S. Marmar, K. Marr, D. Mossessian, R. Parker, W. Rowan, N. Smick, J. A. Snipes, J. L. Terry, S. M. Wolfe, S. J. Wukitch, and the Alcator C-Mod Team. Transport-driven scrape-off layer flows and the x-point dependence of the lh power threshold in alcator c-mod. *Physics of plasmas*, 12(5), 2005.

[LWD$^+$15] Z. X. Lu, W. X. Wang, P. H. Diamond, G. Tynan, S. Ethier, C. Gao, and J. Rice. Intrinsic torque reversals induced by magnetic shear effects on the turbulence spectrum in tokamak plasmasa). *Physics of Plasmas*, 22(5), 2015.

[MAC$^+$11a] P. Mantica, C. Angioni, C. Challis, G. Colyer, L. Frassinetti, N. Hawkes, T. Johnson, M. Tsalas, P. C. deVries, J. Weiland, B. Baiocchi, M. N. A. Beurskens, A. C. A. Figueiredo, C. Giroud, J. Hobirk, E. Joffrin, E. Lerche, V. Naulin, A. G. Peeters, A. Salmi, C. Sozzi, D. Strintzi, G. Staebler, T. Tala, D. Van Eester, and T. Versloot. *Phys. Rev. Lett.*, 107:135004, 2011.

[MAC$^+$11b] P. Mantica, C. Angioni, C. Challis, G. Colyer, L. Frassinetti, N. Hawkes, T. Johnson, M. Tsalas, P. C. deVries, J. Weiland, B. Baiocchi, M. N. A. Beurskens, A. C. A. Figueiredo, C. Giroud, J. Hobirk, E. Joffrin, E. Lerche, V. Naulin, A. G. Peeters, A. Salmi, C. Sozzi, D. Strintzi, G. Staebler, T. Tala, D. Van Eester, and T. Versloot. A key to improved ion core confinement in the jet tokamak: Ion stiffness mitigation due to combined plasma rotation and low magnetic shear. *Phys. Rev. Lett.*, 107:135004, Sep 2011.

[MAD+11] R M McDermott, C Angioni, R Dux, A Gude, T Ptterich, F Ryter, G Tardini, and the ASDEX Upgrade Team. Effect of electron cyclotron resonance heating (ecrh) on toroidal rotation in asdex upgrade h-mode discharges. *Plasma Physics and Controlled Fusion*, 53(3):035007, 2011.

[MD68] Wallace M. Manheimer and Thomas H. Dupree. Weak turbulence theory of velocity space diffusion and the nonlinear landau damping of waves. *The Physics of Fluids*, 11(12):2709–2723, 1968.

[MD88] N. Mattor and P. H. Diamond. Momentum and thermal transport in neutral-beamheated tokamaks. *Physics of Fluids*, 31(5):1180, 1988.

[MDGH09] C. J. McDevitt, P. H. Diamond, Ö. D. Gürcan, and T. S. Hahm. Toroidal rotation driven by the polarization drift. *Phys. Rev. Lett.*, 103:205003, Nov 2009.

[MPW+01] G.R. McKee, C.C. Petty, R.E. Waltz, C. Fenzi, R.J. Fonck, J.E. Kinsey, T.C. Luce, K.H. Burrell, D.R. Baker, E.J. Doyle, X. Garbet, R.A. Moyer, C.L. Rettig, T.L. Rhodes, D.W. Ross, G.M. Staebler, R. Sydora, and M.R. Wade. Non-dimensional scaling of turbulence characteristics and turbulent diffusivity. *Nuclear Fusion*, 41(9):1235, 2001.

[NCDH96] D. E. Newman, B. A. Carreras, P. H. Diamond, and T. S. Hahm. The dynamics of marginality and selforganized criticality as a paradigm for turbulent transport. *Physics of Plasmas*, 3(5):1858–1866, 1996.

[PAB+11] A. G. Peeters, C. Angioni, A. Bortolon, Y. Camenen, F. J. Casson, B. Duval, L. Fiederspiel, W. A. Hornsby, Y. Idomura, T. Hein, N. Kluy, P. Mantica, F. I. Parra, A. P. Snodin, G. Szepesi, D. Strintzi, T. Tala, G. Tardini, P. de Vries, and J. Weiland. *Nuclear Fusion*, 51(9):094027, 2011.

[PH09] Leonardo Patacchini and Ian H. Hutchinson. Kinetic solution to the mach probe problem in transversely flowing strongly magnetized plasmas. *Phys. Rev. E*, 80:036403, Sep 2009.

[RCD+11] J. E. Rice, I. Cziegler, P. H. Diamond, B. P. Duval, Y. A. Podpaly, M. L. Reinke, P. C. Ennever, M. J. Greenwald, J. W. Hughes, Y. Ma, E. S. Marmar, M. Porkolab, N. Tsujii, and S. M. Wolfe. Rotation reversal bifurcation and energy confinement saturation in tokamak ohmic *l*-mode plasmas. *Phys. Rev. Lett.*, 107:265001, Dec 2011.

[RDK00] B. N. Rogers, W. Dorland, and M. Kotschenreuther. Generation and stability of zonal flows in ion-temperature-gradient mode turbulence. *Phys. Rev. Lett.*, 85:5336–5339, Dec 2000.

[RHD+11a] J. E. Rice, J. W. Hughes, P. H. Diamond, Y. Kosuga, Y. A. Podpaly, M. L. Reinke, M. J. Greenwald, Ö. D. Gürcan, T. S. Hahm, A. E. Hubbard, E. S. Marmar, C. J. McDevitt, and D. G. Whyte. *Phys. Rev. Lett.*, 106:215001, 2011.

[RHD$^+$11b] J. E. Rice, J. W. Hughes, P. H. Diamond, Y. Kosuga, Y. A. Podpaly, M. L. Reinke, M. J. Greenwald, Ö. D. Gürcan, T. S. Hahm, A. E. Hubbard, E. S. Marmar, C. J. McDevitt, and D. G. Whyte. Edge temperature gradient as intrinsic rotation drive in alcator *c*-mod tokamak plasmas. *Phys. Rev. Lett.*, 106:215001, May 2011.

[RHS$^+$06] H. Reimerdes, T. C. Hender, S. A. Sabbagh, J. M. Bialek, M. S. Chu, A. M. Garofalo, M. P. Gryaznevich, D. F. Howell, G. L. Jackson, R. J. La Haye, Y. Q. Liu, J. E. Menard, G. A. Navratil, M. Okabayashi, S. D. Pinches, A. C. Sontag, E. J. Strait, W. Zhu, M. Bigi, M. de Baar, P. de Vries, D. A. Gates, P. Gohil, R. J. Groebner, D. Mueller, R. Raman, J. T. Scoville, W. M. Solomon, the DIII-D Team, JET-EFDA Contributors, and the NSTX Team. Cross-machine comparison of resonant field amplification and resistive wall mode stabilization by plasma rotation. *Physics of Plasmas*, 13(5), 2006.

[Ric16] J E Rice. Experimental observations of driven and intrinsic rotation in tokamak plasmas. *Plasma Physics and Controlled Fusion*, 58(8):083001, 2016.

[RICd$^+$07a] J. E. Rice, A. Ince-Cushman, J. S. deGrassie, L. G. Eriksson, Y. Sakamoto, A. Scarabosio, A. Bortolon, K. H. Burrell, B. P. Duval, C. Fenzi-Bonizec, M. J. Greenwald, R. J. Groebner, G. T. Hoang, Y. Koide, E. S. Marmar, A. Pochelon, and Y. Podpaly. Inter-machine comparison of intrinsic toroidal rotation in tokamaks. *Nuclear Fusion*, 47(11):1618, 2007.

[RICd$^+$07b] J.E. Rice, A. Ince-Cushman, J.S. deGrassie, L.-G. Eriksson, Y. Sakamoto, A. Scarabosio, A. Bortolon, K.H. Burrell, B.P. Duval, C. Fenzi-Bonizec, M.J. Greenwald, R.J. Groebner, G.T. Hoang, Y. Koide, E.S. Marmar, A. Pochelon, and Y. Podpaly. Inter-machine comparison of intrinsic toroidal rotation in tokamaks. *Nuclear Fusion*, 47(11):1618, 2007.

[RLM$^+$04] J. E. Rice, W. D. Lee, E. S. Marmar, P. T. Bonoli, R. S. Granetz, M. J. Greenwald, A. E. Hubbard, I. H. Hutchinson, J. H. Irby, Y. Lin, D. Mossessian, J. A. Snipes, S. M. Wolfe, and S. J. Wukitch. *Nuclear Fusion*, 44(3):379, 2004.

[RPR$^+$13] J. E. Rice, Y. A. Podpaly, M. L. Reinke, R. Mumgaard, S. D. Scott, S. Shiraiwa, G. M. Wallace, B. Chouli, C. Fenzi-Bonizec, M. F. F. Nave, P. H. Diamond, C. Gao, R. S. Granetz, J. W. Hughes, R. R. Parker, P. T. Bonoli, L. Delgado-Aparicio, L.-G. Eriksson, C. Giroud, M. J. Greenwald, A. E. Hubbard, I. H. Hutchinson, J. H. Irby, K. Kirov, J. Mailloux, E. S. Marmar, and S. M. Wolfe. *Phys. Rev. Lett.*, 111:125003, 2013.

[RSK04] Andre L Rogister, Raghvendra Singh, and Predhiman K Kaw. On ion temperature gradient and parallel velocity shear instabilities. *Physics of Plasmas*, 11(5):2106, 2004.

[RTB$^+$96] B W Rice, T S Taylor, K H Burrell, T A Casper, C B Forest, H Ikezi, L L Lao, E A Lazarus, M E Mauel, B W Stallard, and E J Strait. The formation and evolution of negative central magnetic shear current profiles on diii-d. *Plasma Physics and Controlled Fusion*, 38(6):869, 1996.

[SBB+97] E J Synakowski, S H Batha, M A Beer, M G Bell, R E Bell, R V Budny, C E Bush, P C Efthimion, T S Hahm, G W Hammett, B. LeBlanc, F. Levinton, E. Mazzucato, H. Park, A. T. Ramsey, G. Schmidt, G. Rewoldt, S. D. Scott, G. Taylor, and M. C. Zarnstorff. Local transport barrier formation and relaxation in reverse-shear plasmas on the tokamak fusion test reactor. *Physics of Plasmas*, 4(5):1736–1744, 1997.

[SBd+07] W M Solomon, K H Burrell, J S deGrassie, R Budny, R J Groebner, J E Kinsey, G J Kramer, T C Luce, M A Makowski, D Mikkelsen, R Nazikian, C C Petty, P A Politzer, S D Scott, M A Van Zeeland, and M C Zarnstorff. Momentum confinement at low torque. *Plasma Physics and Controlled Fusion*, 49(12B):B313, 2007.

[SCZ+16] Yue Sun, Z.P. Chen, G. Zhuang, L. Wang, H. Liu, and Z.J. Wang. Investigations of turbulent transport and intrinsic torque of toroidal momentum at the edge of j-text tokamak with electrode biasing. *Nuclear Fusion*, 56(4):046006, 2016.

[SDF+90] S. D. Scott, P. H. Diamond, R. J. Fonck, R. J. Goldston, R. B. Howell, K. P. Jaehnig, G. Schilling, E. J. Synakowski, M. C. Zarnstorff, C. E. Bush, E. Fredrickson, K. W. Hill, A. C. Janos, D. K. Mansfield, D. K. Owens, H. Park, G. Pautasso, A. T. Ramsey, J. Schivell, G. D. Tait, W. M. Tang, and G. Taylor. Local measurements of correlated momentum and heat transport in the tftr tokamak. *Phys. Rev. Lett.*, 64:531–534, Jan 1990.

[SKK+13] Y. J. Shi, W. H. Ko, J. M. Kwon, P. H. Diamond, S. G. Lee, S. H. Ko, L. Wang, S. Yi, K. Ida, L. Terzolo, S. W. Yoon, K. D. Lee, J. H. Lee, U. N. Nam, Y. S. Bae, Y. K. Oh, J. G. Kwak, M. Bitter, K. Hill, O. D. Gurcan, and T.S. Hahm. Ech effects on toroidal rotation: Kstar experiments, intrinsic torque modelling and gyrokinetic stability analyses. *Nuclear Fusion*, 53(11):113031, 2013.

[Tay15] G. I. Taylor. Eddy motion in the atmosphere. *Philosophical Transactions of the Royal Society of London. Series A, Containing Papers of a Mathematical or Physical Character*, 215:1–26, 1915.

[TBC+14a] S C Thakur, C Brandt, L Cui, J J Gosselin, A D Light, and G R Tynan. Multi-instability plasma dynamics during the route to fully developed turbulence in a helicon plasma. *Plasma Sources Science and Technology*, 23(4):044006, 2014.

[TBC+14b] SC Thakur, C Brandt, L Cui, JJ Gosselin, AD Light, and GR Tynan. Multi-instability plasma dynamics during the route to fully developed turbulence in a helicon plasma. *Plasma Sources Science and Technology*, 23(4):044006, 2014.

[TGM^{+}16] S. C. Thakur, J. J. Gosselin, J. McKee, E. E. Scime, S. H. Sears, and G. R. Tynan. Development of core ion temperature gradients and edge sheared flows in a helicon plasma device investigated by laser induced fluorescence measurements. *Physics of Plasmas*, 23(8):082112, 2016.

[WDH12a] Lu Wang, P H Diamond, and T S Hahm. How does drift wave turbulence convert parallel compression into perpendicular flows? *Plasma Physics and Controlled Fusion*, 54(9):095015, 2012.

[WDH12b] Lu Wang, P H Diamond, and T S Hahm. How does drift wave turbulence convert parallel compression into perpendicular flows? *Plasma Physics and Controlled Fusion*, 54(9):095015, 2012.

[WDR92] X.H. Wang, P. H. Diamond, and M. N. Rosenbluth. Stability of iontemperature-gradientdriven modes in the presence of sheared poloidal flows. *Physics of Fluids B: Plasma Physics*, 4(8):2402–2413, 1992.

[WGE^{+}17] W. X. Wang, B. A. Grierson, S. Ethier, J. Chen, E. Startsev, and P. H. Diamond. Understanding and predicting profile structure and parametric scaling of intrinsic rotation. *Physics of Plasmas*, 24(9):092501, 2017.

[WJGH92] F. L. Waelbroeck, T. M. Antonsen Jr., P. N. Guzdar, and A. B. Hassam. Theory of driftacoustic instabilities in the presence of sheared flows. *Physics of Fluids B: Plasma Physics*, 4(8):2441–2447, 1992.

[WLG^{+}] B.N. Wan, Y.F. Liang, X.Z. Gong, J.G. Li, N. Xiang, G.S. Xu, Y.W. Sun, L. Wang, J.P. Qian, H.Q. Liu, X.D. Zhang, L.Q. Hu, J.S. Hu, F.K. Liu, C.D. Hu, Y.P. Zhao, L. Zeng, M. Wang, H.D. Xu, G.N. Luo, A.M. Garofalo, A. Ekedahl, L. Zhang, X.J. Zhang, J. Huang, B.J. Ding, Q. Zang, M.H. Li, F. Ding, S.Y. Ding, B. Lyu, Y.W. Yu, T. Zhang, Y. Zhang, G.Q. Li, T.Y. Xia, the EAST team, and Collaborators. Overview of east experiments on the development of high-performance steady-state scenario. *Nuclear Fusion*, 57(10):102019.

[XHS^{+}13] Y. Xu, C. Hidalgo, I. Shesterikov, M. Berte, P. Dumortier, M. Van Schoor, M. Vergote, A. Krmer-Flecken, R. Koslowski, and the TEXTOR Team. Role of symmetry-breaking induced by e r b shear flows on developing residual stresses and intrinsic rotation in the textor tokamak. *Nuclear Fusion*, 53(7):072001, 2013.

[XTD^{+}11a] M. Xu, G. R. Tynan, P. H. Diamond, C. Holland, J. H. Yu, and Z. Yan. Generation of a sheared plasma rotation by emission, propagation, and absorption of drift wave packets. *Phys. Rev. Lett.*, 107:055003, Jul 2011.

[XTD^{+}11b] M. Xu, G. R. Tynan, P. H. Diamond, C. Holland, J. H. Yu, and Z. Yan. Generation of a sheared plasma rotation by emission, propagation, and absorption of drift wave packets. *Phys. Rev. Lett.*, 107:055003, Jul 2011.

[YHN^{+}15] M. Yoshida, M. Honda, E. Narita, N. Hayashi, H. Urano, M. Nakata, N. Miyato, H. Takenaga, S. Ide, and Y. Kamada. Effects of toroidal rotation shear and magnetic shear on thermal and particle transport in plasmas with electron cyclotron heating on jt-60u. *Nuclear Fusion*, 55(7):073014, 2015.

[YXD^{+}10a] Z. Yan, M. Xu, P. H. Diamond, C. Holland, S. H. Müller, G. R. Tynan, and J. H. Yu. Intrinsic rotation from a residual stress at the boundary of a cylindrical laboratory plasma. *Phys. Rev. Lett.*, 104:065002, Feb 2010.

[YXD^{+}10b] Z. Yan, M. Xu, P. H. Diamond, C. Holland, S. H. Müller, G. R. Tynan, and J. H. Yu. Intrinsic rotation from a residual stress at the boundary of a cylindrical laboratory plasma. *Phys. Rev. Lett.*, 104:065002, Feb 2010.